

**ROLE OF VASCULAR REMODELING IN THE ACCUMULATION,  
CLEARANCE, AND BIODISTRIBUTION OF BIOMOLECULAR  
FACTORS IN MELANOMA**

A Dissertation  
Presented to  
The Academic Faculty

By

Nathan Andrew Rohner

In Partial Fulfillment  
Of the Requirements for the Degree  
Doctor of Philosophy in Bioengineering

Georgia Institute of Technology

August 2017

**COPYRIGHT © 2017 BY NATHAN A. ROHNER**

**ROLE OF VASCULAR REMODELING IN THE ACCUMULATION,  
CLEARANCE, AND BIODISTRIBUTION OF BIOMOLECULAR  
FACTORS IN MELANOMA**

Approved by:

Dr. Susan N. Thomas, Advisor  
School of Mechanical Engineering  
*Georgia Institute of Technology*

Dr. Fredrik O. Vannberg  
School of Biological Sciences  
*Georgia Institute of Technology*

Dr. Edward A. Botchwey  
Department of Biomedical Engineering  
*Georgia Institute of Technology*

Dr. Edmund K. Waller  
Department of Hematology and  
Medical Oncology  
*Emory University School of Medicine*

Dr. Krishnendu Roy  
Department of Biomedical Engineering  
*Georgia Institute of Technology*

Date Approved: May 5, 2017

*To my family and friends – parents John and Margarite, sister Sarah, brother-in-law  
Brandon, and fiancée Samantha – for their encouragement and support.*

## **ACKNOWLEDGEMENTS**

I would like to express my thanks to the members of the Thomas Lab who were all reliable sources of support and comradery during my time at Georgia Tech. All of this work would not have been possible without the patience, direction, and encouragement from my advisor, Susan Thomas, and the support of Alex Schudel and Erin Edwards. I am also grateful for my many friends in the Bioengineering program and at the Georgia Tech Catholic Center. I am thankful for the support from other faculty, notably Andrés García, and the staff and core lab managers of the Parker H. Petit IBB whom have helped me through this journey. Thanks to my family and faith for helping me to pursue my dreams.

# TABLE OF CONTENTS

<b>ACKNOWLEDGEMENTS</b>	<b>iv</b>
<b>LIST OF TABLES</b>	<b>viii</b>
<b>LIST OF FIGURES</b>	<b>ix</b>
<b>LIST OF SYMBOLS AND ABBREVIATIONS</b>	<b>xi</b>
<b>SUMMARY</b>	<b>xiv</b>
<b>CHAPTER 1. INTRODUCTION</b>	<b>1</b>
1.1 Motivation	1
1.2 Specific Aims	4
1.3 Significance	8
<b>CHAPTER 2. BACKGROUND AND LITERATURE REVIEW</b>	<b>9</b>
2.1 Tumor Progression and Advanced Disease Outcomes	9
2.2 Tumor-secreted Soluble Factors	10
2.2.1 Soluble Factor Signaling within the Tumor Microenvironment	10
2.2.2 Alterations in Soluble Factor Quality and Quantity with Disease Progression	11
2.3 Implications of TSF in the Systemic Effects of Cancer	12
2.3.1 Evidence of Tumor Soluble Factor Bioavailability in Circulation	12
2.3.2 Tumor-derived Soluble Factors Implicated in Metastasis, Immunosuppression, and Cancer-associated Thrombosis	13
2.3.3 Systemic Tissues Adversely Impacted by Melanoma Progression	14
2.4 Tissue Physical Properties Regulating Soluble Factor Transport Profiles	15
2.4.1 Blood and Lymphatic Clearance of Biomolecules from the Interstitium	15
2.4.2 Impact of Interstitial Fluid Pressure on Molecular Transport	15
2.4.3 Extracellular Matrix Effects on Soluble Factor Transport	16
2.5 Tumor-induced Microenvironmental Remodeling in Cancer	16
2.5.1 Role of VEGF-A and -C Signaling Axes in Vascular Remodeling	16
2.6 Molecular Transport in Lymph Nodes	17
2.6.1 Transport and Organization within the Lymph Node	17
2.6.2 Lymph Node Substructure and Remodeling with Disease	18
2.7 Biomaterial Design for dLN Targeted Immunotherapies and Vaccines	21
2.7.1 Physicochemical Carrier Properties Influence Clearance and Dissemination	21
2.7.2 Locoregional Immunotherapy and Alternative Applications	22
<b>CHAPTER 3. MELANOMA PROGRESSION REDUCES MOLECULAR CLEARANCE FROM TUMORS AND BIODISTRIBUTION TO DRAINING LYMPH NODES WHILE INCREASING SYSTEMIC TISSUE ACCUMULATION</b>	<b>23</b>
3.1 Introduction	23
3.2 Materials and Methods	25

3.2.1	B16F10 Mouse Melanoma Cell Culture	25
3.2.2	TSF Analysis in Tumor Cell Conditioned Media	26
3.2.3	Near-infrared Fluorescent Tracers and Conjugation	26
3.2.4	B16F10 Mouse Melanoma Animal Model	27
3.2.5	Micro-computed Tomographic Imaging and Quantification of Vasculature	27
3.2.6	Tracer Biodistribution Analysis	28
3.2.7	Statistical Analysis	29
<b>3.3</b>	<b>Results</b>	<b>29</b>
3.3.1	Tumor Secreted Soluble Factors and Fluorescent Tracer Representatives	29
3.3.2	Size-dependent Rates and Extents of Clearance from the Naïve Skin	31
3.3.3	Size-dependent Tracer Biodistribution after Clearance from Naïve Skin	33
3.3.4	Remodeling of the Tumor Vascular Plexus with Tumor Growth	35
3.3.5	Malignancy Increases Locoregional Tracer Exposure	36
3.3.6	Tumor Progression Reduces dLN Accumulation and Increases Systemic Exposure to Tumor-derived Factors	37
<b>3.4</b>	<b>Discussion</b>	<b>43</b>
<b>3.5</b>	<b>Conclusions</b>	<b>47</b>
<b>CHAPTER 4. Flexible macromolecule versus rigid particle retention in the injected skin and accumulation in draining lymph nodes are differentially influenced by hydrodynamic size</b>		<b>49</b>
<b>4.1</b>	<b>Introduction</b>	<b>49</b>
<b>4.2</b>	<b>Materials and Methods</b>	<b>51</b>
4.2.1	Fluorescent Tracers	51
4.2.2	Biodistribution Experiments and Analysis	52
4.2.3	Statistical Analysis	53
<b>4.3</b>	<b>Results</b>	<b>53</b>
4.3.1	Skin Retention versus Exposure in Systemic Tissues Increases with Increasing Tracer Size	54
4.3.2	Accumulation within dLN is Greatest for Macromolecules and Increases with Size over 72 hr for Particles, albeit at Lower Levels of dLN-Specific Enrichment Relative to Macromolecules	56
4.3.3	Macromolecular but not Particulate Tracer Exposure within the Skin and dLN is Size-dependent	58
<b>4.4</b>	<b>Discussion</b>	<b>59</b>
<b>4.5</b>	<b>Conclusion</b>	<b>63</b>
<b>CHAPTER 5. VEGF-A and -C-induced Disease Progression Effects on Size-Regulated Profiles of Tumor-derived Molecular Association with Immune Cells within Locoregional Lymph Nodes Versus Systemic Tissues</b>		<b>64</b>
<b>5.1</b>	<b>Introduction</b>	<b>64</b>
<b>5.2</b>	<b>Materials and Methods</b>	<b>66</b>
5.2.1	Animal Tumor Models and Inhibitor Treatment	66
5.2.2	ELISA Measurements of Tissue VEGF-A and VEGF-C	67
5.2.3	Micro-computed Tomography Imaging for Vascular Measurements	67
5.2.4	Fluorescent Tracers	68
5.2.5	Tracer Injections	68

5.2.6	Tracer Biodistribution Analyses	69
5.2.7	Tumor and Lymph Node Immunohistochemistry and Imaging	69
5.2.8	Tracer Flow Cytometry Analyses	70
5.2.9	Tracer Diffusion Analyses	71
5.2.10	Statistical Analysis	71
<b>5.3</b>	<b>Results</b>	<b>72</b>
5.3.1	Endogenous and Induced or Suppressed Angiogenic and Lymphangiogenic Signaling During Melanoma Progression	72
5.3.2	Clearance from Tumors is Increased with VEGF-C Overexpression and VEGFR-2 Inhibition	74
5.3.3	VEGFR-2 Inhibition Partially Recovers 500 and 10 nm Tracer dLN Accumulation, while VEGF-C Overexpression Results in Reduced Systemic Tissue Exposure to 500 and 30 nm Tracers	77
5.3.4	Hydrodynamic Size- and Tumor (Lymph)angiogenic Signaling-dependent Profiles of Tracer Association with Discrete Immune Cell Subpopulations within dLN	78
5.3.5	dLN Distributions of Tracers and Resident Cell Subpopulations are Influenced by Hydrodynamic Size-dependent Tumor Vascular Remodeling, Respectively	80
5.3.6	Overall Tissue Cellular Association with Tumor Progression Increased for 500 nm, Especially in Spleen Cells, but Decreased for 10 nm Tracers	82
5.3.7	Altered 30 and 10 nm Tracer Exposure for Tumor-dLN Dendritic, Barrier, and Migratory Cellular Populations, but not B and T Cells, while 500 nm Exhibits Size-dependent Restriction of Diffusion by Cross-linked Collagen	85
<b>5.4</b>	<b>Discussion</b>	<b>88</b>
<b>5.5</b>	<b>Conclusions</b>	<b>90</b>
<b>CHAPTER 6.</b>	<b>CONCLUDING REMARKS AND FUTURE DIRECTIONS</b>	<b>92</b>
<b>6.1</b>	<b>Contributions to the Field</b>	<b>92</b>
6.1.1	Multi-tool Integration to Determine In Situ Soluble Factor Clearance, Accumulation, and Biodistribution at Picomolar Levels	92
6.1.2	Validating Conservation of Size-dependent Lymph Node Drug Targeting in Melanomas over the Course of Disease Progression	93
6.1.3	Demonstrating Enhanced Systemic Tissue Accumulation of Tumor-derived Factors with Advanced Malignancy	94
6.1.4	Informing the Rational Design of Drug Targeting and Delivery Strategies to Achieve Locoregional Immunomodulation in Skin and dLN	95
6.1.5	Providing Insight of Molecular Mechanisms of Tumor Vascular Remodeling Influencing Soluble Factor Transport and Cellular Association	97
<b>6.2</b>	<b>Future Directions</b>	<b>98</b>
6.2.1	Developing Therapeutic Strategies to Curtail the Aberrant Transport Profiles and Negative Disease Outcomes of Cancer Soluble Factors	98
6.2.2	Clinical Applications of Targeted Locoregional Immunotherapies	99
6.2.3	Evaluation of Soluble Factor Transport in Other Inflammatory Diseases	100
<b>REFERENCES</b>		<b>102</b>

## LIST OF TABLES

Table 3.1	TSF Tracer Panel Zeta Potentials and Fluorescent Excitation/Emissions	30
Table 3.2	TSF Tracer Detection Limits (pM) within Tissue Homogenates	32

## LIST OF FIGURES

Figure 2.1	Survival Statistics for Melanoma of the Skin	9
Figure 2.2	Categories of Endogenous TSF and Their Potential Signaling Outcomes	11
Figure 2.3	Lymph Node Transport and Organization	18
Figure 2.4	Microstructures of Skin dLNs	20
Figure 2.5	Locoregional Therapeutic Administration Scheme	22
Figure 3.1	Analysis of B16F10 Conditioned Media and Fluorescent Tracers	30
Figure 3.2	Preparative and Analytical Size-exclusion Chromatography	31
Figure 3.3	Size-dependent Molecular Clearance and Biodistribution of Tracers into Local Versus Systemic Tissues	33
Figure 3.4	B16F10 Melanoma Vascular Remodeling	36
Figure 3.5	Tracer Exposure is Modestly Increased in the Tumor Interstitium	37
Figure 3.6	Fluorescent Tracers Exhibit Increased Accumulation in Systemic Tissues with Tumor Progression	39
Figure 3.7	Tumor Progression Reduces Tracer Accumulation within TDLN	41
Figure 3.8	Melanoma Disease Progression has no effect on the Proportion on 30 nm Tracer Exposure in TDLN while Increasing Exposure of Other Tracers in Systemic Tissues	43
Figure 4.1	Measured Hydrodynamic Sizes of Tracers	54
Figure 4.2	Characterization of Individual versus Mixtures of Tracers	55
Figure 4.3	Tracer Retention in Skin Injection Site Increases with Macromolecular but not Particle Hydrodynamic Size	56
Figure 4.4	Tracer Accumulation within dLN is Greatest for Macromolecules and Increases most Appreciably over time with Increasing Particle Size	57
Figure 4.5	Tracer Exposure within dLN and Skin is Size and Form Dependent	59

Figure 5.1	Characterization of Tumor Models	73
Figure 5.2	VEGF-C Overexpression in Culture and Skin Section IHC	74
Figure 5.3	VC and R2 Partially Recover 500 and 10 nm LN Drainage, while VC Prevents Enhanced 500 and 30 nm Tracer Systemic Dissemination	76
Figure 5.4	Enhanced Cellular Tracer Exposure within VC and R2 dLN	79
Figure 5.5	Tracer Localization, Cellular Frequencies, and Organizational Remodeling within dLN	81
Figure 5.6	Systemic Tracer Cellular Exposure	83
Figure 5.7	Size-dependent Tracer Distribution Profiles among Paracortex, Barrier, and Migratory Cells and Tracer Diffusion through Collagen	87

## LIST OF SYMBOLS AND ABBREVIATIONS

$\mu$ CT	Micro-computed tomography
$\mu$ g	Microgram
$\mu$ l	Microliter
$\mu$ m	Micrometer
AF610	Alexa Fluor 610
AF700	Alexa Fluor 700
ANOVA	Analysis of variance
AU	Arbitrary unit
AUC	Area under the curve
cDC	Conventional dendritic cell
$C_{\max}$	Concentration maximum
Conc.	Concentration
Da	Dalton
DAPI	4',6-diamidino-2-phenylindole
Dex	Dextran
dLN	Draining lymph node(s)
DNA	Deoxyribonucleic acid
D-PBS	Dulbecco's phosphate buffered saline
ECM	Extracellular matrix
ELISA	Enzyme-linked immunosorbent assay
EPR	Enhanced permeability and retention
FITC	Fluorescein isothiocyanate
HEV	High endothelial venule

i.d.	Intradermal
i.t.	Intratumoral
i.v.	Intravenous
IHC	Immunohistochemistry
IL	Interleukin
Inj.	Injection
LN	Lymph node(s)
LSD	Least significant difference
MCM	Medullary cord macrophage
MFI	Mean fluorescence intensity
MIA	Melanoma inhibitory activity
MSM	Medullary sinus macrophage
mV	Millivolt
MW	Molecular weight
NHS	N-hydroxysuccinimide
nm	Nanometer
pDC	Plasmacytoid dendritic cell
PD-L1	Programmed death-ligand 1
pg	Picogram
pM	Picomolar
PS	Polystyrene
SEC	Size exclusion chromatography
SF	Soluble factors
SSM	Subcapsular sinus macrophage
TDLN	Tumor-draining lymph node(s)

TRITC	Tetramethylrhodamine isothiocyanate
TSF	Tumor-secreted soluble factors
VEGF	Vascular endothelial growth factor
VEGFR	Vascular endothelial growth factor receptor
WT	Wild-type

## SUMMARY

Local inflammation within the tumor microenvironment is implicated in the systemic effects of disease progression, such as immune suppression and metastasis. Soluble factors (SF) produced within the tumor, including cytokines, exosomes, proteases, and microvesicles, mediate pathological signaling and have emerged as putative therapeutic targets. However, SF bioavailability in distributed tissues and the impact of disease progression on their dissemination profiles and exposure to various immune cell subsets is poorly defined. This stymies progress towards therapeutic amelioration of SF signaling activities to improve disease outcomes and is the critical knowledge gap this thesis seeks to fill. The central hypothesis is that tumor vascular remodeling redirects the organism-wide exposure of SF secreted locally within the tumor microenvironment, which may negatively contribute to disease burden by altering the bioavailability of molecules important to systemic disease progression. In this thesis, the effects of local tissue remodeling in melanoma leading to pathological SF accumulation profiles within distributed tissues are elucidated in order to provide insight into the potential for localized disease to exert systemic effects and inform opportunities to develop better preventive and curative treatment options for advanced melanomas.

# CHAPTER 1. INTRODUCTION

## 1.1 Motivation

Melanoma remains a significant clinical problem with an estimated 10,000 deaths in the US population in 2016 alone (American Cancer Society). While the 5 year survival rate for localized melanoma of the skin is around 98%, it drops to 18% when distant metastasis is involved (National Cancer Institute). Therapeutic interventions that effectively treat advanced melanomas to improve patient outcomes are thus in crucial need of development.

Local immune suppression is known to occur within the pre-metastatic niche prior to dissemination [1, 2]. How this immune suppression arises, however, remains unclear. The formation of a pre-metastatic niche via cues which promote tumor immune suppression, tumor cell survival and outgrowth, as well as pre-conditioning of local stromal and bone marrow-derived progenitor cells before metastatic cell dissemination is a crucial phase in cancer metastasis [3-5]. Factors secreted within the tumor microenvironment are known to play multifaceted roles in facilitating disease progression, including immune suppression and dissemination [3]. The pro-metastatic secretome is also capable of inducing enhanced vascular permeability and remodeling in disseminated tissues [6], activation of tissue-resident fibroblasts and macrophages resulting in changes in extracellular matrix (ECM) composition and physical properties [7, 8], and recruitment of immune cells which contribute to a pro-tumorigenic, inflammatory microenvironment [5, 9, 10] indicating a robust involvement of multiple extratumoral signaling pathways in cancer progression. However, the bioavailability of tumor-secreted soluble factors (TSF), including various proteins, proteases, exosomes,

and microvesicles, and the impact of tumor progression on their capacities to signal in disseminated tissues, such as pre-metastatic niches, are poorly defined. This stymies progress towards therapeutic amelioration of TSF signaling activities to improve disease outcome and is the critical knowledge gap this dissertation seeks to fill.

Mechanisms of TSF clearance from the tumor microenvironment and dissemination profiles to regional versus systemic tissues likely play major roles in the regulation of TSF signaling locality and resulting functions in cancer progression. The importance of both extent of TSF dissemination and lymphatic versus blood clearance routes are evident in the differences between lymph node versus systemic tissue filtering capacities, relative dilutional effects, and selectivity of exposure to tissue-resident cellular subsets [11]. However, vascular remodeling due to hyper-angiogenic signaling in primary tumors results in haphazard tissue remodeling and a tortuous, dilated, and leaky tumor blood vascular network [12, 13] that is accompanied by lymphatic hyperplasia [14]. These characteristics are well recognized to manifest in the enhanced permeability and retention (EPR) effect in which systemically circulating particulates at the nano- and microscales accumulate to a greater extent within malignant relative to healthy tissues [15], yet the impact of this vascular remodeling on the clearance and biodistribution of TSF remains to be determined.

In addition to remodeling within the tumor microenvironment, tumor-induced remodeling of the structural and cellular organization within tumor-draining tissues has the potential to modulate TSF exposure in these sites of disease progression. Tumor draining lymph nodes (dLN) are secondary lymphoid tissues important in the adaptive immune response and exhibit specialized substructural distributions of cells with distinct

immunological functions for antigen presentation and lymphocyte activation. Several studies have characterized the partitioning of species by molecular weight within healthy and virus infected dLN [16, 17]. However, the effects of tumor dLN remodeling on cellular frequencies and distributions as well as extracellular matrix reorganization in response to tumor drainage [18-20] influencing TSF exposure profiles is unknown. Additionally, while the presence of tumor-derived biomolecules within patients' sera has been observed useful for biomarker tests, this also indicates the bioavailability of TSF to mediate systemic signaling in disseminated tissues and potential immune-privileged sites involved in cancer progression [11]. Tumor-derived pro-angiogenic factor signaling in pre-metastatic systemic tissues [21] may further enhance TSF accumulation and exposure profiles [3]. Together, these examples highlight the need to elucidate the effects of tumor-initiated extratumoral remodeling processes that may dynamically influence cellular exposure to TSF.

Ultimately, the *long term goal* of this work is to characterize the effects of tumor growth and remodeling on TSF tissue and cellular exposure profiles to determine the extent and localization of tumor-derived factors in malignant disease progression that may be targeted and identify opportunities for developing effective treatment strategies. The *overall objective* of this proposal is to provide fundamental insight regarding how vascular remodeling in the malignant skin affects the rate, extent, and size-dependence of molecular transport and association with local dLN-resident subpopulations versus systemic tissue immune cells. The *central hypothesis* is that vascular remodeling within diseased tissues redirects the organism-wide transport of locally secreted TSF and may negatively contribute to disease burden by altering the bioavailability of molecules

important to cancer progression. This central hypothesis will be tested in rigorous preclinical melanoma animal models in the following specific aims.

## **1.2 Specific Aims**

***Specific Aim 1A: Evaluate the Effects of Tumor Progression on Soluble Factor Accumulation, Clearance, and Biodistribution in Melanoma.*** The *working hypothesis* of this aim is that cancer disease progression alters the bioavailability of TSF within the primary tumor, dLN, and systemic tissues. To better understand the effect of disease progression on the biodistribution of TSF, a fluorescently-conjugated tracer panel was size-matched to relevant TSF 5-500 nm in hydrodynamic diameter and infused into the naïve dermis or directly into the dermal lesions of melanoma bearing mice. The extent of intratumoral clearance as well as biodistribution into local versus systemic tissues was determined by tissue-, tracer size-, and time-resolved analyses. Perfusion of a vascular contrast agent followed by micro-computed tomography ( $\mu$ CT) analysis of vascular volume, surface area, and mean vessel diameter provided quantitative insight into the effect of disease progression on tumor vascular remodeling. Tracer dissemination profiles were compared with  $\mu$ CT results to evaluate the extent and time course for which dermal vascular remodeling influences molecular clearance and biodistribution. Results illustrated that despite tumor progression-induced reductions in TSF drainage to sentinel lymph nodes, size-based principles of lymphatic drug delivery are conserved, and that tumors exhibit enhanced molecular clearance into circulation, resulting in systemic tissue accumulation of TSF. The outcomes of this aim inform the rational design of sentinel lymph node-targeted drug delivery strategies as well as future studies implicating that

angioplastic therapy might be used to mitigate the pathological effects of altered TSF exposure profiles in cancer progression. These results are presented in Chapter 3.

***Specific Aim 1B: Determine the Combined Effects of Size and Form on Dermal Retention and dLN Accumulation.*** The *working hypothesis* of this aim was to inform how drug carriers comprised of engineered biomaterials can be leveraged to improve treatment efficacy by enhancing the selective accumulation or retention of payload in the skin and its dLN. This was accomplished by analyzing the influence of rigid particle versus flexible macromolecule hydrodynamic size on profiles of retention in the site of dermal injection as well as the corresponding extent of accumulation in dLN and systemic off-target tissues. Using a panel of fluorescently labeled tracers comprised of inert polymers that are resistant to hydrolysis and proteolytic degradation and spanning a size range of widely used drug carrier systems, I determined that macromolecule but not rigid particle retention within the skin was size-dependent, whereas the relative dermal enrichment compared to systemic tissues increased with size for both tracer types. Additionally, these results suggest that intra- versus extracellular availability of delivered payload within dLN may be influenced by both the size and form of engineered drug carriers. The outcomes of this aim inform how biomaterial-based drug carriers can be designed to enhance the selective exposure of formulated drug in target tissues to improve the therapeutic efficacy as well as minimize off-target effects of locoregional immunotherapy. The results are presented in Chapter 4.

***Specific Aim 2A: Elucidate the Effects of VEGF-A and -C Endogenous and Induced Signaling on Altered Tumor-derived Molecular Biodistribution Profiles.*** The *working hypothesis* for this aim is that tumor angiogenic and/or lymphangiogenic signaling mechanisms underlie the altered clearance and biodistribution of TSF observed with disease progression characterized in Aim 1A. Therefore, the effects of endogenous and induced or suppressed angiogenic and lymphangiogenic signaling during melanoma progression on TSF molecular biodistribution from tumors was determined by intratumorally infusing a tracer panel in melanoma bearing mice divided into cohorts treated with an angiogenic signaling inhibitor or with tumors overexpressing the lymphangiogenic soluble ligand, vascular endothelial growth factor (VEGF)-C. Separately, perfusion of vascular contrast agent followed by  $\mu$ CT analysis and immunohistochemistry (IHC) staining for blood and lymphatic vessels were used to determine the extent of vascular normalization due to applied inhibition and overexpression conditions. The results of this aim reveal that clearance from tumors is increased with VEGF-C overexpression and VEGFR-2 inhibition. VEGFR-2 inhibition partially recovers 500 and 10 nm tracer dLN accumulation, while VEGF-C overexpression results in reduced systemic tissue exposure to 500 and 30 nm tracers. The outcomes of this aim inform how TSF transport profiles may be modulated with angioplastic therapies that can be used to mitigate the detrimental effects of endogenous molecules from the tumor microenvironment or improve tumor-administered therapy bioavailability in locoregional tissues. These results are presented in Chapter 5.

***Specific Aim 2B: Delineate the Influence of Melanoma on Size-dependent Molecular Distribution to Immune Cells within dLN versus Systemic Tissues.*** The *working hypothesis* for this aim is that increased tumor vascular permeability as well as diminished lymphatic function will alter the capacity of TSF active in the regulation of immune signaling to distribute amongst subpopulations of systemic tissue-resident immune cells versus dLN-resident cells that exhibit distinct substructural distributions as well as immunological functions. Herein, the effects of tumor vascular remodeling, including those resulting from tumor VEGF-C overexpression (OE) and VEGF receptor-2 inhibition, on exposure of sentinel lymph node-resident as well as systemic tissue-resident phagocytic and immune cell subpopulations to factors derived from the tumor microenvironment were determined. The *in vivo* biodistribution and uptake by immune cell subtypes of a panel of fluorescently labeled macromolecular and particulate tracers size-matched to physiological biomolecules ranging from 10-500 nm in hydrodynamic diameter after intradermal or intratumoral infusion in C57Bl6 mice was resolved in a temporal- and tissue-resolved fashion by flow cytometry. The changes in dLN paracortex-resident and barrier cell frequencies and distributions were also determined by IHC of frozen dLN sections. The results of this aim indicate a reduced percentage of 30 and 10 nm tracers associated with LN-resident barrier cell macrophages and dendritic cells, but similar uptake levels by B and T cell populations in tumor dLN versus naïve tissues. The outcomes of this aim inform that tissue-level changes in transport to and molecular abundance within the dLN do not translate to equally proportional changes in cellular uptake by all dLN cell subtypes in tumor dLN. The results are presented in Chapter 5.

### **1.3 Significance**

This work provides valuable insight into the following: 1) the role of vascular remodeling altering TSF clearance and biodistribution profiles, 2) the conservation of size-dependent drug delivery principles for dLN targeted therapy in advanced melanoma, 3) the differences between particulate and macromolecular size-dependent transport profiles for locoregional immunotherapy, and 4) the relative distribution of TSF among dLN-resident subpopulations versus systemic tissue immune cells. This study investigated how tumor progression and interventions in angiogenic and lymphangiogenic signaling alters molecular transport by using relevant mouse models of melanoma and highly quantitative tissue- and cellular-level analysis techniques. These results inform of potential local and systemic TSF transport activities that may be targeted as well as how angiogenic or lymphangiogenic therapies may affect aberrant molecular biodistribution profiles. Furthermore, the role of vascular changes in pathological molecular transport and signaling could become an important aspect for evaluation in other chronic inflammatory diseases or in wound healing applications. The incorporation of a range of sizes of particulate and macromolecular forms in these studies allows the results to apply not only to endogenous tumor-secreted biomolecules, but also to bioengineered drug carriers and informs design criteria based upon desired transport profiles and selective exposure to immune cell subsets in the dLN that will prove useful in vaccine and locoregional immunotherapy applications.

## CHAPTER 2. BACKGROUND AND LITERATURE REVIEW

### 2.1 Tumor Progression and Advanced Disease Outcomes

The transition of cancer from a locally confined to a widespread disease with disseminated effects, such as metastasis and anti-tumor immune suppression, not only makes treatment by resection or conventional methods difficult, but results in greatly increased rates of morbidity. Cancer is accompanied by many hallmarks within the tumor microenvironment that enable disease progression at the local level, such as enhanced proliferation, replicative immortality, increased survival signaling of cancer cells, and tumor vascular remodeling [22]. However, late stage cancers present with advanced hallmarks including anti-tumor immune suppression and metastasis to regional lymph nodes as well as distant tissues that result in poor disease outcomes.

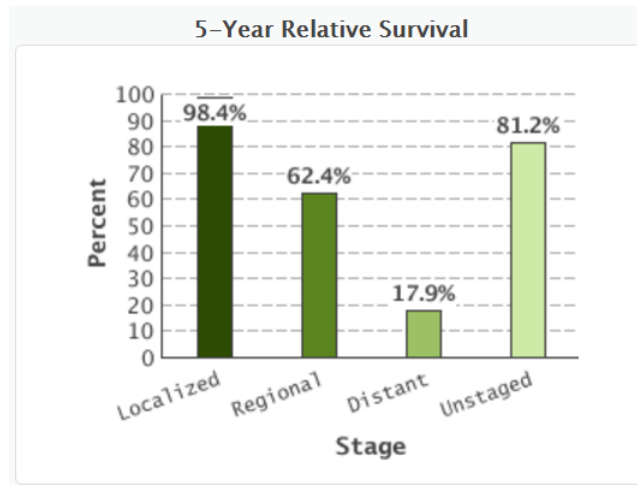


**Figure 2.1 Survival Statistics for Melanoma of the Skin by Stage at Time of Diagnosis. (National Cancer Institute, SEER 18 2006-2012)**

Specifically, melanoma remains a significant clinical problem with an estimated 10,000 deaths in the US population in 2016 alone (American Cancer Society). While the 5 year survival rate for localized melanoma of the skin in 2000 for both sexes was 98.4%, it drops to an unfortunate 17.9% when distant metastasis is involved (Figure 2.1).

Moreover, the main sites of melanoma metastasis—bone, brain, liver, and lung, are within tissues that make detection and treatment challenging. Additionally, mechanisms initiated by cancer cells have been shown to result in enabling tumor progression through evasion of immune destruction and promoting anti-tumor immune suppression [23]. Together these data rationalize further exploring the underlying signaling of advanced cancer associated pathologies to develop better preventative and remedial treatment options.

## **2.2 Tumor-secreted Soluble Factors**

### *2.2.1 Soluble Factor Signaling within the Tumor Microenvironment*

SF (soluble factors) produced within the tumor microenvironment play important and multifaceted roles in the regulation of malignant disease progression. TSF such as cytokines, chemokines, proteases, and microparticles (including microvesicles and exosomes) mediate intercellular signaling at the cell- and tissue-levels to regulate cellular proliferation [24], angiogenesis [25] and lymphangiogenesis [20], recruitment of regulatory immune cells [26, 27], as well as extracellular matrix remodeling [28] via their direct effects or nucleic acid and/or protein transfer (Figure 2.2). Accordingly, numerous TSF and their associated signaling pathways active within the primary tumor have emerged as potential therapeutic targets given their implicated role in the promotion of malignant disease progression associated with poor prognosis including metastasis and anti-tumor immune suppression. However, the bioavailability and potential for TSF to mediate extratumoral signaling processes are relatively understudied which hinders the development of effective treatments against systemic disease progression.

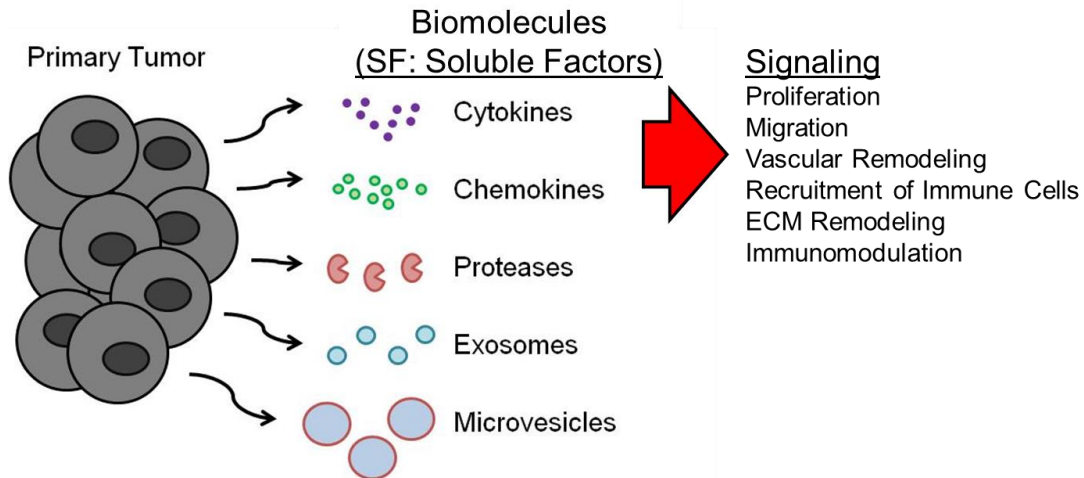


**Figure 2.2 Categories of Endogenous TSF and Their Potential Signaling Outcomes.**

### 2.2.2 Alterations in Soluble Factor Quality and Quantity with Disease Progression

A multitude of either tumor or stromal cell-secreted biomarkers exhibit altered levels of expression in the tumor microenvironment, which make them useful prognostic markers [29-31], and implicate their signaling pathways in disease progression. Tumor growth and the unchecked proliferation of cancer cells accumulating genetic mutations drive the upregulation and diversity of TSF [32, 33]. For example, metallothionein (cysteine-rich proteins with molecular weights of 500-14,000 Da) overexpression observed in IHC analysis of tumor sections, which also correlated with CD68+ macrophage infiltration, has been linked to tumor progression and increased risk of metastasis in cutaneous malignant melanoma [29]. Other overexpressed melanoma-derived SF include matrix metalloproteinase-2[34] (a 72,000 Da type IV collagenase), transforming growth factor- $\beta$  [35] (a 25,000 Da autocrine growth factor), and indoleamine 2,3-dioxygenase[30] (a 45,000 Da heme-containing enzyme). In addition to proteins, mRNA, miRNA, DNA, and other genetic materials are packaged and secreted from cells in vesicular bodies termed exosomes (~20-100 nm in diameter) and microvesicles (100-1000 nm in diameter) [36]. These vesicles provide a high

concentration of signaling molecules that has been shown to play roles in cancer progression such as through influencing metastasis [37] and immunosuppression [38]. The range in TSF sizes and forms indicate the need for further studying how the physical and functional properties of these tumor-derived signaling factors influence systemic disease progression.

TSF are specifically involved in melanoma progression through promotion of invasion [39], metastasis [40], cytokine secretion [41], and anti-tumor immune suppression [41]. For example, melanoma inhibitory activity (MIA) is a soluble protein derived from macrophages that was observed to enhance the further production of MIA by melanoma cells and increase their invasive behavior *in vitro* [39]. In another study, a soluble form of VEGFR-1 was identified to play a role in modulating the invasiveness of melanoma cells and their metastatic loci [40]. Soluble program death-ligand 1 (sPD-L1) has also recently been implicated in melanoma as higher levels in the blood were associated with increased levels of pro-inflammatory cytokines and an immunosuppressive phenotype with decreased overall survival [41]. These examples indicate specific TSF signaling pathways that are relevant in melanoma, which is considered herein, but TSF profiles may differ for other forms of cancer.

## **2.3 Implications of TSF in the Systemic Effects of Cancer**

### *2.3.1 Evidence of Tumor Soluble Factor Bioavailability in Circulation*

Molecules secreted within the tumor microenvironment that may be found in blood circulation have become useful as serological biomarkers [42-45], but also provide evidence for the bioavailability and potential signaling of TSF in systemic tissues as a possible mechanism of disease progression in multiple forms of cancer. These markers, identified from blood samples, rather than tumor biopsy which aids in clinical evaluation and treatment of many cancers include S100B and lactate dehydrogenase (LDH) in advanced melanoma[42], prostate-specific antigen (PSA) levels in prostate cancer[43],

and heat shock protein 90A (HSP90A) for early breast cancer detection[44], amongst a multitude of others. Vesicular forms of soluble factors may also be present in the serum of cancer patients, such as increased concentrations of exosomal miR-373 in women with estrogen- and progesterone-negative breast cancers[45]. Interestingly, many studies of vesicle-borne signaling in mediating cancer progression implicate extratumoral functions [37, 38] indicating the need for further studying the clearance and biodistribution of these tumor-derived signaling particulates to determine how TSF macromolecular versus vesicular form impacts tissue- and cellular-level exposure profiles.

### *2.3.2 Tumor-derived Soluble Factors Implicated in Metastasis, Immunosuppression, and Cancer-associated Thrombosis*

In addition to SF function within the tumor microenvironment, tumor-derived SF have been reported to be active in signaling within distant tissues, such as the lymph nodes, liver, lungs, kidneys, and spleen. For example, intravenous (i.v.) infusion of melanoma-derived exosomes promotes metastasis by directing host progenitor cell differentiation toward a pro-metastatic phenotype [46]. Treatment with mammary tumor-conditioned media can also induce lung and lymph node remodeling to accelerate spontaneous metastasis [47]. Moreover, tumor antigen presentation in tumor-draining lymph nodes (TDLN) is implicated in directing anti-tumor immune suppression [20, 48]. These data therefore suggest mechanisms of signaling to distributed tissues that direct the activity of SF in facilitating disease progression that are not restricted to the primary tumor.

Mechanisms of SF clearance from the tumor microenvironment and distribution to disseminated tissues are anticipated to play important roles in the regulation of SF signaling locality and of resulting function in cancer. This has been widely considered in the context of tumor lymphatic transport function, in particular for its role in facilitating cellular invasion and metastasis [49-51] and as a conduit for immune modulatory SF to

reshape the TDLN immune microenvironment [20, 52]. The role of SF clearance via the blood vasculature and resulting distribution in systemic tissues on the other hand has been largely overlooked. However, treatment with melanoma-conditioned media redirects Lewis lung carcinoma metastasis from the lung to the kidney, spleen, intestine, and oviduct [5], tissues more typical of melanoma dissemination, suggesting a potential role for systemically circulating tumor-derived SF in directing organism-wide responses to growing tumors. Interestingly, TDLN-targeted, but not systemically infused, toll-like receptor ligand adjuvant therapy has been shown to be efficacious in reducing tumor burden [48] by exploiting localized depots of endogenously produced tumor antigen within TDLN delivered via tumor-draining lymphatics. As cancer-associated thrombosis is also a significant cause of patient morbidity in cancer, tumor-derived microparticles expressing tissue factor have been demonstrated to exhibit procoagulant activity and are associated with acute thrombocytopenia when injected into mice [53]. Thus, the relative contribution of blood versus lymphatic-mediated SF clearance and resulting accumulation in associated tissues may not only influence SF signaling activity and role in disease progression but also susceptibility to therapeutic interventions neutralizing or exploiting SF function. Furthermore, the vast majority of cancer-related deaths are due not to the local effects of the primary tumor, but rather the systemic effects of cancer such as metastasis [54]. Thus, there is a clear need to develop understanding of the mechanism of SF dissemination to and bioavailability within systemic tissues.

### *2.3.3 Systemic Tissues Adversely Impacted by Melanoma Progression*

Most cancers, including melanoma, exhibit organ-specific pre-metastatic niche formation which implicates TSF pre-conditioning as a directed process in specific tissue sites. Major tissues afflicted by melanoma metastasis include lung, brain, bone, liver, dLN, and other areas of the skin [55]. Melanomas are observed to metastasize primarily to regional dLN [55]. Moreover, tumor dLN, but not contralateral non-draining LN, are

bathed in TSF by virtue of their proximity to the tumor and lymphatic drainage function [20, 48]. Because the dLN and other tissues are organotropic sites of metastasis, it would greatly benefit the development of advanced cancer treatments and understanding the role of TSF in pre-metastatic niche formation by identifying the extent of TSF exposure within these sites over the course of disease progression.

## **2.4 Tissue Physical Properties Regulating Soluble Factor Transport Profiles**

### *2.4.1 Blood and Lymphatic Clearance of Biomolecules from the Interstitium*

Principles of size exclusion and mass transport along with physical tissue properties regulate TSF clearance and biodistribution profiles which determines their potential to signal in local versus disseminated tissues. Within the healthy interstitium (e.g. the skin) the processes underlying SF dissemination via blood or lymphatic-mediated clearance are controlled by the physical parameters of the tissue microenvironment as well as the size of the SF. Clearance of SF less than 5.4 nm in hydrodynamic diameter occurs rapidly via resorption into the venous blood capillaries [56], whereas SF 5-100 nm in diameter are too large to be resorbed directly into systemic circulation due to the physiological pore size limits for transcapillary transport and are cleared instead from the interstitium via interstitial flow and lymphatic transport mechanisms [56]. Changes in the biophysical characteristics of the interstitium and vasculature may therefore result in altered molecular transport and modify TSF signaling.

### *2.4.2 Impact of Interstitial Fluid Pressure on Molecular Transport*

While diffusion, the process by which the net movement of molecules proceeds along a concentration gradient, can facilitate molecular transport over short length-scales, another important factor mediating interstitial molecular transport over longer length scales is hydrostatic pressure gradients and solvent-solute drag. Capillary filtration and fluid reabsorption drives the bulk fluid exchange within the interstitium. The interstitial fluid hydrostatic pressure is also maintained by lymphatic vessels constantly draining

excess fluid from the interstitium to prevent edema. Solvent-solute drag then mediates transport of molecules; however, in cases of altered hydrostatic pressure gradients, transport by diffusion may become more dominant [57].

#### *2.4.3 Extracellular Matrix Effects on Soluble Factor Transport*

The extracellular matrix constrains the transport of larger SF, such that molecules greater than ~100 nm in hydrodynamic diameter must be removed from peripheral tissues and transported to dLN by dendritic cell-mediated trafficking mechanisms which transpire over a period of several days [58, 59]. While steric and hydrodynamic interactions primarily influence the transport of molecules, electrostatic forces may affect interstitial diffusion as well when the fiber size is comparable to the Debye length (i.e. important for interactions with small glycosaminoglycans, but not larger collagen fibers) [60]. Thus, the use of near neutral molecules is desirable to avoid hindered diffusion by electrostatic effects in drug delivery [60]. Overall, solvent-solute drag, solute diffusion, hemodynamic forces, charge, and colloid osmotic gradients in combination with SF size direct the clearance and biodistribution profiles of SF from interstitial tissues [61].

### **2.5 Tumor-induced Microenvironmental Remodeling in Cancer**

#### *2.5.1 Role of VEGF-A and -C Signaling Axes in Vascular Remodeling*

Local vascular remodeling in diseased states has the potential to dramatically influence blood versus lymphatic-mediated clearance and biodistribution of SF by altering SF transport mechanisms and barriers. For example, hyper-angiogenic signaling via VEGF-A upregulation during tumor formation and growth causes haphazard tissue remodeling and spurs a tortuous, dilated, and hyper-permeable [12, 13, 62] tumor blood vascular network. VEGF-C overexpression was found to result in lymphatic hyperplasia, increased volumetric flow rates of peritumoral lymphatics, and increased metastasis to tumor dLN by four-fold [14]. Additionally, increased interstitial fluid pressure [63, 64]

has been shown to limit the penetration and efficacy of molecular drug delivery to tumors [65-67] as well as the biophysical changes in extracellular matrix properties within some tumors including increased collagen density [68, 69]. Tumor vascular remodeling is well recognized to manifest in the enhanced permeability and retention effect in which systemically circulating particulates at the nano- and microscales accumulate to a greater extent within malignant relative to healthy tissues [15]. Yet while changes in the tumor vasculature have been studied and exploited for tumor-targeted drug delivery applications, the impact of vascular remodeling changes on the clearance and biodistribution of endogenous SF from a primary tumor is unknown.

## **2.6 Molecular Transport in Lymph Nodes**

### *2.6.1 Transport and Organization within the Lymph Node*

Lymph nodes function as the body's major hubs for lymphocyte transport, passage through which is intrinsically complex. Cells and lymph-borne solutes from local tissues are delivered and incompletely removed via lymphatics acting in a unidirectional manner due to one-way valves. Once in the lymph node, cells are subdivided into T and B cell zones while fluids and small molecules (<70 kDa) are shuttled within the lymph node via fibroblastic reticular cell-lined conduits. High endothelial venules (HEVs) also facilitate entry of cells as well as exchange of solutes and fluids with the systemic blood circulation (Figure 2.3). [70]

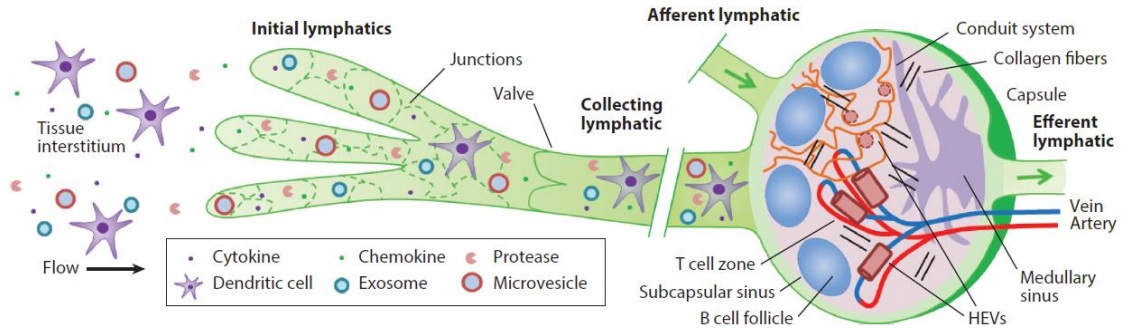


**Figure 2.3 Lymph Node Transport and Organization.** Lymphatic uptake of small molecules, particulates, and cells within the tissue interstitium results in carriage to dLNs, tissues whose microstructure orchestrates the comingling of lymph and lymphocytes to facilitate adaptive immunity and tolerance. The transport role of the lymphatics in the delivery of peripheral tissue-derived antigens, cytokines and chemokines, immune modulatory particles, and immune cells can thus modulate the immunological and biophysical microenvironment of dLNs to influence adaptive immune response in multiple ways.

### 2.6.2 Lymph Node Substructure and Remodeling with Disease

The cellular and molecular distribution profiles within lymph nodes are significantly influenced by lymphatic transport function. For example, in the absence of dermal lymphatics, disorganized stromal cell distributions, minimal B cell follicle definition, and smaller or collapsed high endothelial venules [71] are found in skin draining but not other lymph node localities (Figure 2.4), consistent with remodeling responses induced within dLNs when afferent lymph flow is occluded [72]. These lymph node organizational changes correspond with abnormal distributions of CCL21 and chemokine (C-X-C motif) ligand (CXCL) 13 [71], chemokines that direct T and B cell positioning within the lymph node, respectively, as well as T cell zone fibroblastic reticular cells and reticular fibers [71], which regulate T cell migration [73]. Together with *in vitro* observations of T zone fibroblastic reticular cell organization, proliferation, and secretion of CCL19 and CCL21 sensitivity to flow [74] suggests that lymphatic

transport-regulated intranodal fluid flow may modulate chemokine-dependent organizational and structural remodeling within the lymph node interstitium.

In addition to flow putatively providing organizational cues, lymph-borne solutes and cells are implicated in directing lymph node remodeling. For example, vascular endothelial growth factor (VEGF) drained from the inflamed skin in a delayed-type hypersensitivity skin model induce lymphatic vessel remodeling and expansion within dLNs [75]. Additionally, microparticles containing tumor necrosis factor secreted by peripheral tissue-resident mast cells and transported via lymphatics induce lymph node hypertrophy [76]. Lymph migrating dendritic cells also direct the remodeling of the lymph node fibroblastic reticular network after immunogenic challenge [77], while the extent of cellular remodeling of the lymph node interstitium has been shown to be proportional to the number of mature lymph-transported dendritic cells [78]. Dendritic cells also direct the proliferation of endothelial cells and HEV expansion within dLNs after either immunization or subcutaneous adoptive transfer of dendritic cells [79].

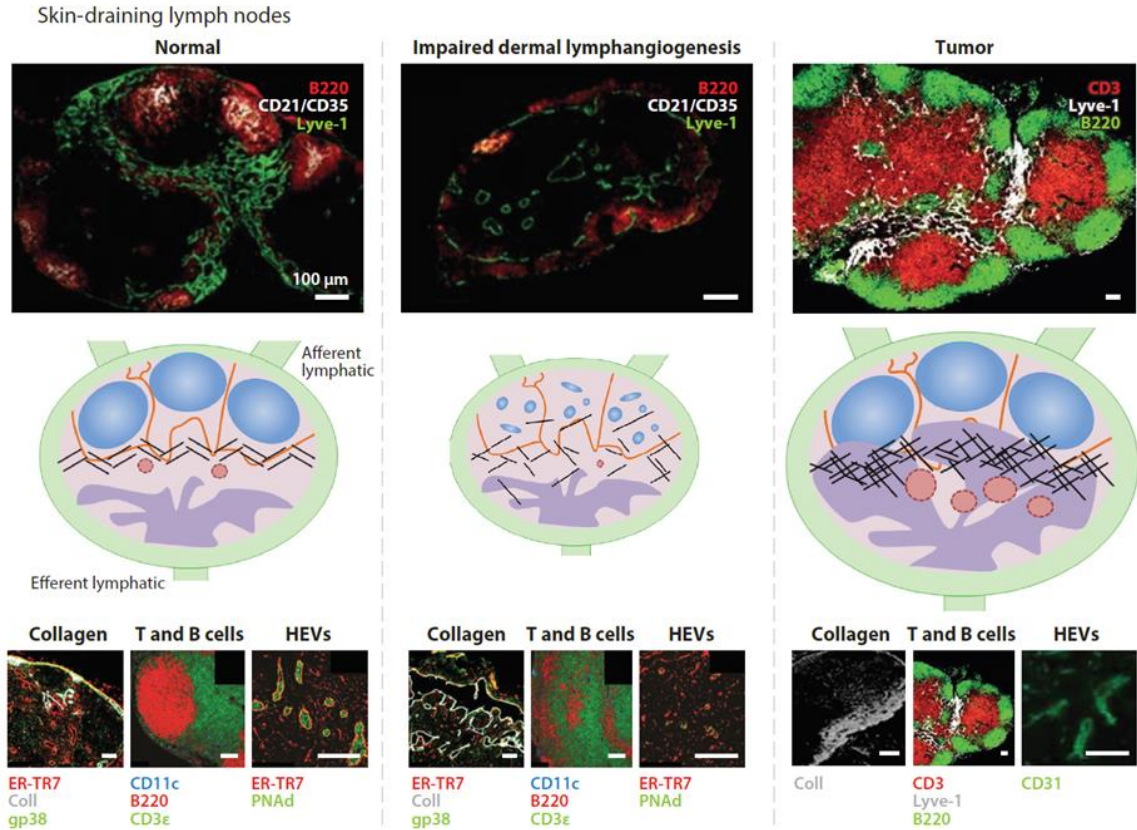


**Figure 2.4** Microstructures of skin dLNs. Normal (left), impaired (middle), and tumor (right) lymphatic transport are shown immunohistochemically and schematically, emphasizing representative collagen organization, T and B cell segmentation, and HEV remodeling responses. Scale bars, 100 µm. Modified from references [70, 71, 80-82].

Given the importance of microstructural properties and cellular distributions in regulating lymph node efficacy at directing adaptive immune response and immunological tolerance, a potential pathophysiological role is suggested by the lymph node remodeling that accompanies numerous disease states. As one example, sentinel, or tumor-draining, lymph nodes are exposed to a high concentration of lymph-transported molecules from the tumor interstitium by virtue of their proximity to growing tumors [18, 48]. Signaling pathways active within the local tumor microenvironment that result in tissue remodeling associated with cancer cell survival [83], invasion [84-86], and

immune suppression [20] therefore have the potential to be operational within TDLN. We recently analyzed lymph nodes from B16 melanoma-bearing mice with respect to tumor stage and found that melanoma lymphatic drainage was associated with alterations in lymph node hyaluronic acid and collagen content corresponding with physical adaptations that manifest in tumors [83, 87, 88] including increased intranodal pressures [18, 89, 90] and increased lymph node tissue stiffness and viscoelasticity [18]. These and other remodeling responses are important as they have the capability to influence critical cellular processes in the lymph node, including cell proliferation, migration, and lymphocyte homing.

## **2.7 Biomaterial Design for dLN Targeted Immunotherapies and Vaccines**

### *2.7.1 Physicochemical Carrier Properties Influence Clearance and Dissemination*

Biomaterials-based formulation strategies offer many advantages for maximizing the therapeutic potential in target tissues while limiting off-target effects, which are controlled by drug clearance rates and profiles of biodistribution. It has been previously demonstrated that the size of antigen conjugated polystyrene spheres influenced antibody titers, LN cellular uptake, and anti-tumor immune response, although the exact mechanisms by which these were accomplished is still undetermined [91]. Similarly, a study by Manolova, et al. [92] demonstrated the effect of particle size on cellular transport and lymphatic uptake, which included many sizes of polystyrene particles and one virus-like particle, but had no direct, size-matched comparison between different formulations or flexibilities (the virus-like particle was 30 nm in diameter while the adjacent particle sizes were 20 and 100 nm). Additionally, the effect of biomaterial form and flexibility has been studied with respect to improving carrier circulation [93] and uptake of particles by cells [94], but has not been previously explored as a variable

influencing dermal retention or dLN accumulation which are pertinent to locoregional immunotherapy and vaccine design.

### 2.7.2 Locoregional Immunotherapy and Alternative Applications

Increasing the efficiency and selectivity of agent delivery or retention in order to prolong drug exposure in skin and dLN (Figure 2.522) is desirable in a variety of immunotherapeutic regimens. For example, intralymphatic immunotherapy [95, 96] as well as intradermal (or intralesional) injection for allergic contact dermatitis and plaque psoriasis [97] or oncolytic virus therapy in melanoma [98] would benefit from biomaterial strategies providing increased local concentrations, reduced off-target effects, and eliminating the need for repeated local injections. While some attempts have been made such as with skin-permeating nanogel systems [97], further studies are necessary to inform application-specific tailoring of biomaterial-based carriers for local tissue and dLN targeting.

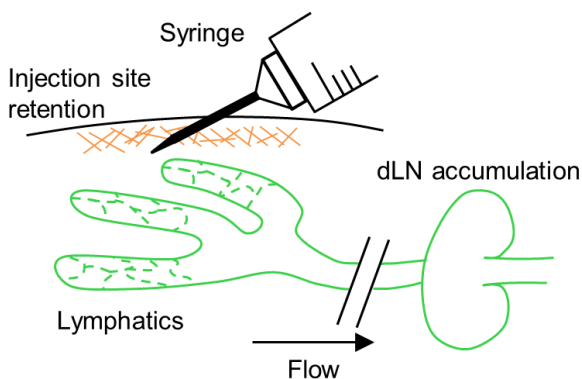


**Figure 2.5 Locoregional Therapeutic Administration Scheme.** Intradermal administration and biomaterial carrier system properties result in localized delivery that is influenced by balancing retention at the injection site, accumulation in dLN, and off-target systemic tissue levels.

## **CHAPTER 3. MELANOMA PROGRESSION REDUCES MOLECULAR CLEARANCE FROM TUMORS AND BIODISTRIBUTION TO DRAINING LYMPH NODES WHILE INCREASING SYSTEMIC TISSUE ACCUMULATION [62]**

### **3.1 Introduction**

Tumor-secreted soluble factors (TSF) such as cytokines, chemokines, proteases, and microparticles (including microvesicles and exosomes) mediate intercellular signaling at the cell- and tissue-levels to regulate cellular proliferation [24], angiogenesis [25] and lymphangiogenesis [20], recruitment of regulatory immune cells [26, 27], as well as extracellular matrix remodeling [28] via their direct effects or nucleic and/or protein transfer. Accordingly, numerous TSF and their associated signaling pathways activated within the primary tumor have emerged as potential therapeutic targets given their implicated role in the promotion of malignant disease progression associated with poor prognosis including metastasis and anti-tumor immune suppression.

In addition to their function within the tumor microenvironment, TSF have reported activities in signaling to distant tissues, such as the lymph nodes, liver, lungs, kidneys, and spleen, which exacerbate disease progression. For example, intravenous (i.v.) infusion of melanoma-derived exosomes promotes metastasis by directing host progenitor cell differentiation toward a pro-metastatic phenotype [46]. Treatment with mammary tumor-conditioned media can also induce lung and lymph node remodeling to accelerate spontaneous metastasis [47]. Moreover, tumor antigen presentation in TDLN is implicated in directing anti-tumor immune suppression [20, 48]. These data therefore suggest mechanisms of signaling to distributed tissues that direct the activity of TSF in facilitating disease progression that are not restricted to the primary tumor.

As such, mechanisms of TSF clearance from the tumor microenvironment and distribution to disseminated tissues likely play important roles in the regulation of TSF

signaling locality and resulting function in cancer. This has been widely considered in the context of tumor lymphatic transport function, in particular for its role in facilitating cellular invasion and metastasis [49-51] and as a conduit for immune modulatory TSF to reshape the TDLN immune microenvironment [20, 52]. The role of TSF clearance via the blood vasculature and resulting distribution in systemic tissues on the other hand has been largely overlooked. However, treatment with melanoma-conditioned media redirects Lewis lung carcinoma metastasis from the lung to the kidney, spleen, intestine, and oviduct [5], tissues more typical of melanoma dissemination, suggesting a potential role for systemically circulating TSF in directing organism-wide responses to growing tumors. Interestingly, TDLN-targeted, but not systemically infused, toll-like receptor ligand adjuvant therapy has been shown to be efficacious in reducing tumor burden [48] by exploiting localized depots of endogenously produced tumor antigen within TDLN delivered via tumor-draining lymphatics. Thus, the relative contribution of blood versus lymphatic-mediated TSF clearance and resulting accumulation in associated tissues may not only influence TSF signaling activity and role in disease progression but also susceptibility to therapeutic interventions neutralizing or exploiting TSF function.

An added level of complexity in this problem is the influence of vascular remodeling that occurs within growing tumors. Hyper-angiogenic signaling during tumor formation and growth causes haphazard tissue remodeling and a tortuous, dilated, and leaky [12, 13] tumor blood vascular network that is accompanied by lymphatic hyperplasia [14]. These characteristics are well recognized to manifest in the enhanced permeability and retention effect in which systemically circulating particulates at the nano- and microscales accumulate to a greater extent within malignant relative to healthy tissues [15]. Yet while this is often exploited for tumor-targeted drug delivery applications, its impact on the clearance and biodistribution of TSF and therapeutic agents administered directly to the tumor remains as-of-yet unknown.

Hence, although TSF and intratumorally administered therapeutic agents have been regarded for their role in local signaling within the tumor microenvironment, their bioavailability in distributed tissues and the impact of disease course on these biodistribution profiles has been overlooked. Unfortunately, detection and quantification of endogenously produced TSF are limited by significant dilutional effects as well as uncertainty in the spatial and temporal source of constitutive or inducible reporter systems. Furthermore, biodistribution analysis of specific exogenously supplied TSF is challenging due to degradation *in vivo*. To circumvent these limitations, we established a panel of near-infrared fluorescent tracers comprised of inert polymers that are resistant to hydrolysis and proteolytic degradation. Since TSF and therapeutic agents such as small molecule drugs and engineered drug delivery vehicles vary widely in hydrodynamic diameter and the rate and extent of blood versus lymphatic clearance from healthy tissues are acutely size-dependent [56, 58], tracers over a physiological biomolecule size-matched range of 5-500 nm in hydrodynamic diameter were chosen. We examined in a temporal- and tissue-resolved manner the clearance and biodistribution of fluorescent tracers after infusion into the B16F10 melanomas of C57Bl6 mice at prescribed tumor growth phases or in the skin of naïve animals. Our findings support the hypothesis that lymphatic drainage significantly enriches levels of tumor-derived factors in dLN, that melanoma progression attenuates lymphatic-mediated transport but not the predominant molecular size regime accumulating within TDLN, and that vascular remodeling within advanced melanomas increases the access of factors derived from the tumor interstitium to systemic tissues.

## **3.2 Materials and Methods**

### *3.2.1 B16F10 Mouse Melanoma Cell Culture*

B16F10 murine melanoma cells were cultured in Dulbecco's Modified Eagle Medium supplemented with 10% heat-inactivated fetal bovine serum and 1%

penicillin/streptomycin/amphotericin B. Media, serum, and antibiotics were obtained from Life Technologies (Carlsbad, CA). Cell lines were routinely checked and confirmed to be negative for mycoplasma infection and rodent pathogens.

### *3.2.2 TSF Analysis in Tumor Cell Conditioned Media*

48 hour B16F10 cell-conditioned serum-free medium, concentrated 20x by lyophilization after removing any possible cells by centrifugation at 300xg for 5 minutes, was fractionated in a size-resolved manner on a Sepharose CL-6B (GE Healthcare, Pittsburgh, PA) gravity chromatography column. The protein and deoxyribonucleic acid (DNA) content in fractionated media was analyzed using the bicinchoninic acid assay (Thermo Fisher Scientific Pierce, Waltham, MA) or by incubation with a 0.5x solution of GelRed (Biotium Inc., Hayward, CA) on an orbital shaker followed by absorbance or fluorescence measurements (BioTek Instruments Inc, Winooski, VT), respectively.

### *3.2.3 Near-infrared Fluorescent Tracers and Conjugation*

500 and 50 nm fluorescent (580/610 nm and 660/680 nm excitation/emission, respectively) carboxylate-modified microspheres were purchased from Life Technologies. 500 kDa or 10 kDa amine-dextran (Sigma-Aldrich, St. Louis, MO) were covalently labeled by incubation for 4 hours in 0.1 M NaHCO<sub>3</sub> buffer at pH 8.4 on a shaker with Alexa Fluor 700 NHS-Ester or Alexa Fluor 610-X NHS-Ester dye (Life Technologies), respectively. Individual fluorescent dextran conjugates were purified from unreacted free dye by Sepharose CL-6B gravity column chromatography. Purified dextran-fluorophore conjugates were confirmed to be free of unconjugated dye by Sepharose CL-6B gravity column chromatography analysis. The size and zeta potentials of 500 and 50 nm fluorescent microspheres as well as 500 and 10 kDa dextran-AF700

conjugates suspended in Dulbecco's Phosphate Buffered Saline (D-PBS, Life Technologies) were confirmed using a Zetasizer Nano ZS (Malvern Instruments Ltd, WR14 1XZ, United Kingdom). All reagents were used and maintained under sterile conditions.

#### *3.2.4 B16F10 Mouse Melanoma Animal Model*

C57Bl6 mice were purchased from Jackson Laboratories. All protocols were approved by the Institutional Animal Care and Use Committee.  $0.5 \times 10^6$  B16F10 murine melanoma cells were intradermally implanted into the left dorsal skin of 6-8 weeks old mice on day 0. Tumors were monitored in anesthetized mice by caliper measurements of melanoma width, length, and depth and reported as an ellipsoidal volume. For intradermal injections, a depth-marked 27 gauge needle (Becton Dickinson, Franklin Lakes, NJ) was inserted perpendicularly into the center of the tumor of mice anesthetized with isoflurane and 10  $\mu$ L of the fluorescent tracer solution ( $1.2 \times 10^8$  500 nm spheres,  $7.9 \times 10^{11}$  50 nm spheres, 23.8  $\mu$ g 500 kDa AF700-dextran, and 3  $\mu$ g of 10 kDa AF610-dextran) in saline was co-infused by syringe pump at a rate of  $\sim 300$  nL per sec for a slow infusion rate that resulted in minimal alterations in interstitial pressure. In the results, day post B16F10 implant refers to the day on which tracer injections were made. Alternatively, naïve mice were injected in the same manner with the same fluorescent tracer panel solution in the dermal layer of the left dorsal skin. For i.v. injections, 3  $\mu$ g of 10kDa AF610-dextran in 100  $\mu$ L saline was injected with a 29 gauge insulin syringe into the jugular vein of mice. The syringe was aspirated to withdraw a small amount of blood before and after injection to confirm that the entire volume was administered i.v.

#### *3.2.5 Micro-computed Tomographic Imaging and Quantification of Vasculature*

Animals were perfused with neutral buffered formalin for 10 minutes, a saline wash for five more minutes, and MicroFil (Flow Tech Inc., Carver, MA) catalyzed at a viscosity appropriate for small vessels (5 mL lead-based contrast agent: 2.5 mL diluent: 0.25 mL curing agent) by syringe with the application of constant pressure. Afterwards, perfused mice were carefully stored at 4°C overnight to cure the contrast agent. The following day, skin or tumor samples were harvested and stored in D-PBS. Micro-computed tomographic imaging was performed using a SCANCO Medical  $\mu$ CT50 (SCANCO USA, Inc., Wayne, PA, USA).  $\mu$ CT image slices were constrained using manual selection of the sample outline and processed with a Gaussian filter at a global threshold via the SCANCO Medical  $\mu$ CT Evaluation Program before 3-dimensional reconstruction. In-house designed algorithms were used to calculate the vascular volume, vascular surface area, and mean vessel diameter within tissue samples [99].

### *3.2.6 Tracer Biodistribution Analysis*

At prescribed times post injection (p.i.), the tumor-draining and non-tumor-draining axillary and brachial lymph nodes, tumor or skin at the injection site, along with the spleen, lungs, liver, and kidneys were harvested and homogenized in D-PBS using 1.4 mm acid washed zirconium grinding beads (OPS Diagnostics LLC, Lebanon, NJ) with a FastPrep-24 Automated Homogenizer (MP Biomedicals, Santa Ana, CA). Tissue homogenate fluorescence was measured using a Synergy H4 BioTek plate reader and fluorescent tracer standard curves were made in individual tissue homogenates. Prism 6 (GraphPad, LaJolla, CA) was used to calculate exposure (as area under the curve from 1-72 hours, AUC) as well as the fluorescent tracer half-life of residence within the site of injection using one-phase decay least-squares regression. Error propagation analysis was

used to calculate the standard error of AUC measurements. Concentrations are presented as the percent of tracer injection amount per tissue volume calculated from the respective tissue's weight and assuming a density of water.

### 3.2.7 *Statistical Analysis*

Data are represented as the mean with S.E.M. and statistics were calculated using Prism 6. Statistical significance was defined as  $p < 0.05$  following two-way ANOVA and post-hoc analysis with Tukey tests or one-way ANOVA followed by Fisher's Least Significant Difference (LSD) test. One, two, three, and four symbols denoting statistical significance represent  $p < 0.05$ , 0.01, 0.001, and 0.0001, respectively, unless otherwise specified.

## 3.3 **Results**

### 3.3.1 *Tumor Secreted Soluble Factors and Fluorescent Tracer Representatives*

As a proxy for TSF produced in vivo, we first analyzed the size distribution of protein- and DNA-containing species within B16F10 cell-conditioned media. Using gravity column chromatography, we found protein and DNA to be contained in fractions in both the large (fractions 6-10 corresponding to hydrodynamic diameters ranging from ~10-1000 nm) and small (fractions 15-24 corresponding to sizes  $< 10$  nm) hydrodynamic size regimes (Figure 3.1A). We thus chose to model this large size range of physiological TSF that also corresponds to the broad size range of various anti-cancer therapeutic agents using a panel of near-infrared fluorescently labeled tracers (Table 3.1) verified free of unconjugated dye (Figure 3.2) with similar physiological levels of negative charge

(Table 3.1) spanning from 5 to 500 nm in hydrodynamic diameter (Figure 3.1B): 10kDa (5 nm) and 500kDa (30 nm) chain-like dextrans were chosen to represent small peptides and larger protein complexes while 50 and 500 nm polystyrene spheres were selected to model exosomes or nanoparticles and microvesicles or microparticles, respectively (Figure 3.1B-C).

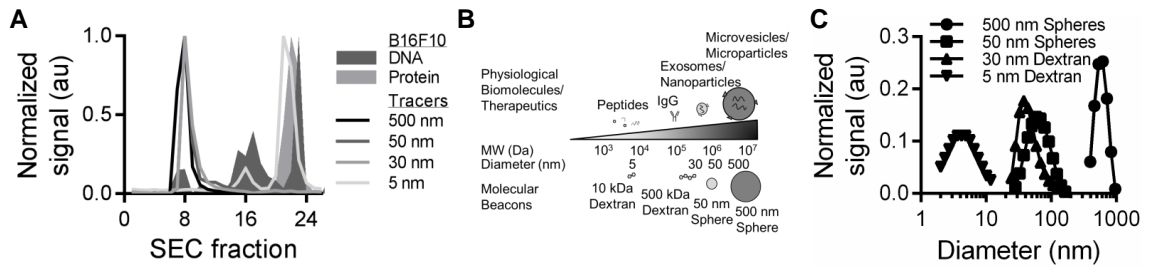


**Figure 3.1 Analysis of B16F10 Conditioned Media and Fluorescent Tracers. (A) Size exclusion chromatography analysis of protein and DNA containing B16F10 conditioned media fractions and fluorescent tracers. (B) Physiological TSF, typical anti-cancer therapeutic agents, and their size-matched tracers used for this study. (C) Dynamic light scattering measurements of tracers.**

**Table 3.1 TSF Tracer Panel Zeta Potentials and Fluorescent Excitation/Emissions**

Fluorescent Tracer	500 nm Polystyrene Sphere	50 nm Polystyrene Sphere	500 kDa (30 nm) Dextran	10 kDa (5 nm) Dextran
Zeta Potential (mV)	-31.3	-15.1	-2.2	-1.7
Fluorescent Tag ( $\lambda$ Ex/Em)	580/610	660/680	700/720	610/630

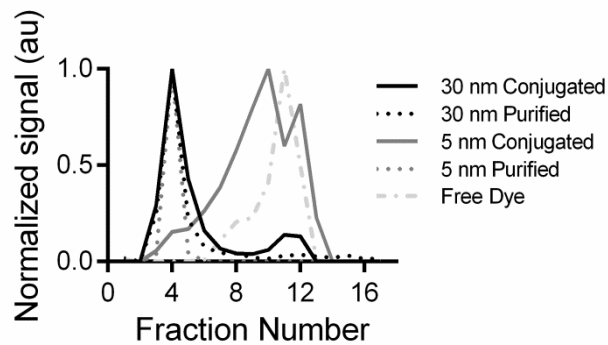


**Figure 3.2 Preparative and analytical size-exclusion chromatography demonstrating separation of free dye from TSF tracer dextran conjugates.**

### 3.3.2 *Size-dependent Rates and Extents of Clearance from the Naïve Skin*

To determine the rate of clearance from the skin and resulting distribution into disseminated tissues, we co-infused the fluorescent tracer cocktail into the lateral dorsal skin of naïve animals and analyzed at timescales over which passive drainage (1-24 hr) versus active cell mediated trafficking (72 hr) from peripheral tissues transpire [71, 100]. Tracer fluorescence was quantified via endpoint analysis of homogenized individual tissues rather than commonly used whole animal imaging techniques, providing superior spatial resolution and limits of detection (Table 3.2). As such, the amount and resulting concentrations of infused tracers within various tissue compartments could be quantified with high sensitivity.

**Table 3.2 TSF Tracer Detection Limits (pM) within Tissue Homogenates.**

Limit of detection (pM) for:	10 kDa Dextran (610/630)	500 kDa Dextran (700/720)	50 nm Sphere (660/680)	500 nm Sphere (580/610)
Lymph Node	290	180	5.0	3.72E-04
Tumor	7000	280	30	4.54E-03
Spleen	660	210	10	3.40E-03
Lung	1460	460	6.0	1.88E-03
Liver	10000	800	180	2.60E-02
Kidney	3350	270	30	4.35E-03

We found the 5 nm tracer to be most extensively cleared, with less than 10% of the injected amount retained after 1 hour p.i. whereas the tracers of larger sizes experienced much more restricted clearance (Figure 3.3A). In terms of the percent remaining 72 hours after injection (Figure 3.3B) and tissue half-life (Figure 3.3C), we found a linear increase with respect to tracer size up to 50 nm. For example, the amount remaining in the dermis after 72 hours was only 3% of the initial injection for the 5 nm tracer, but approximately 50 and 80% for the 30 versus 50 and 500 nm tracers, respectively (Figure 3.3B). The 5 nm tracer was also cleared most quickly, with a calculated retention half-life of only about 10 minutes, while the larger tracers were transported away more slowly with retention half-lives on the order of tens to hundreds of hours (Figure 3.3C).

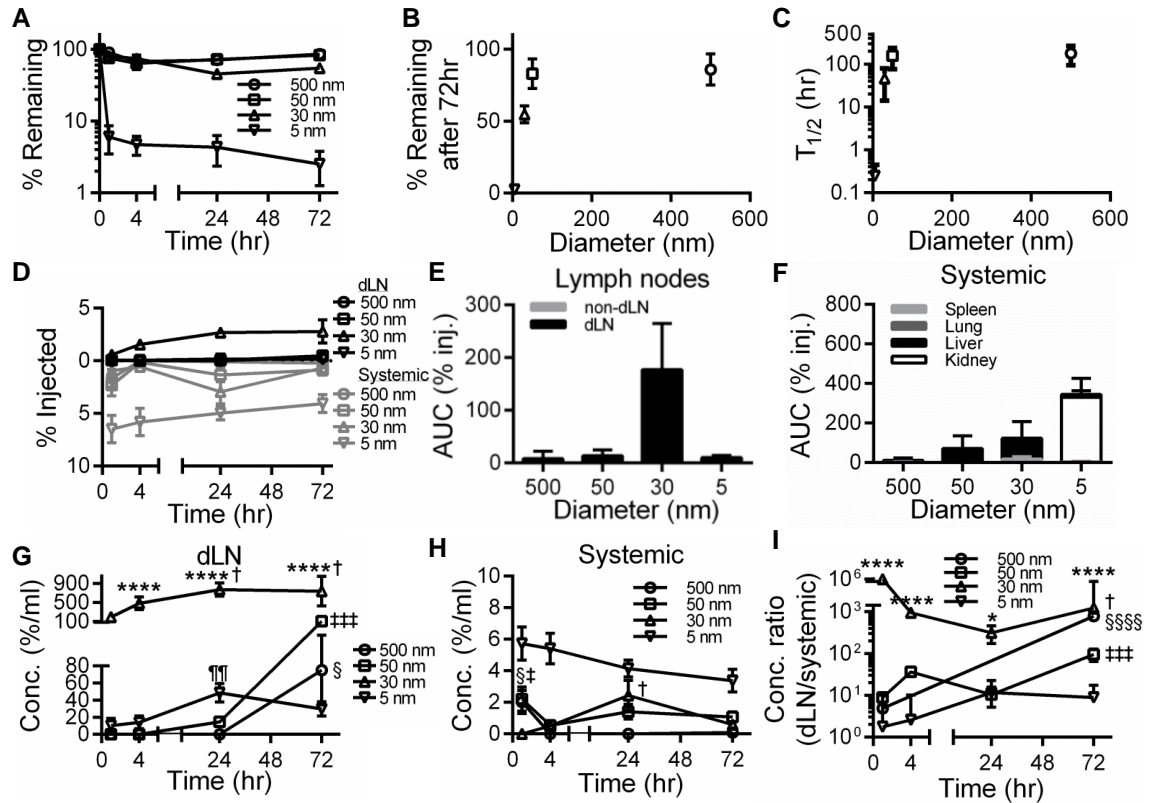


**Figure 3.3** Size-dependent clearance and biodistribution of tracers into local versus systemic tissues after intradermal injection in naïve mice. Time-resolved retention profiles (A), % remaining after 72 hr (B), and retention half-lives ( $T_{1/2}$ , C) of tracers within skin. Time-resolved accumulation (D) and exposure (E-F) of tracers in dLN and non-dLN (E) versus systemic tissues including the spleen, lungs, liver, and kidneys (F). E, \*\*\* indicates significance relative to all other tracers by one-way ANOVA and post-hoc Fisher's LSD tests. F, \*\*\* indicates significance relative to all other tracers and kidneys vs all other tissues for 5 nm tracer by two-way ANOVA and post-hoc Tukey's tests. AUC from 1-72 hr p.i. Tracer concentrations in dLN (G) and systemic tissues (H). (I) Ratio of accumulating tracer concentrations within dLN to systemic tissues. G-I, \* indicates significance relative to all other tracers at the same time point by two-way ANOVA and post-hoc Tukey's tests. § indicates significance for 500 nm tracer relative to all other time points (H-I), ‡ for 50 nm tracer relative to all other time points in (G,I) but only vs 4 hr in (H), † for 30 nm tracer vs 1 hr in (G) but relative to all other time points in (H,I), and ¶ for 5 nm tracer vs 1 and 4 hr in (G) by one-way ANOVA and post-hoc Fisher's LSD tests; results representative of n=9 mice per group performed in three independent experiments.

### 3.3.3 Size-dependent Tracer Biodistribution after Clearance from Naïve Skin

Concurrent with analyzing their clearance from naïve skin, we measured the accumulation of infused tracers within dLN or into systemic tissues, including the lungs, spleen, liver, and kidneys, in excised tissue homogenates via fluorescence. We found that 30 nm dextran accumulated most appreciably within dLN at all measured time points (Figure 3.3D). This resulted in a dramatically higher exposure (% injected) of the 30 nm tracer within dLN relative to both smaller (5 nm) and larger tracers (50 and 500 nm) tested here (Figure 3.3E). No exposure (% injected) was seen in non-dLN (Figure 3.3E), confirming this clearance was lymphatic mediated. Conversely, 5 nm dextran was most appreciably found within systemically distributed tissues (lungs, spleen, liver, and kidneys) (Figure 3.3D) resulting in the highest levels of total systemic exposure (% injected) of all tracers (Figure 3.3F). Exposure (% injected) in these tissues for the 5 nm tracer was highest in the kidneys whereas larger tracer sizes accumulated predominantly in the liver (Figure 3.3F). When accounting for tissue volumes, these biodistribution profiles resulted in appreciable levels of dLN accumulation for 50 and 500 nm tracers only after 72 hr p.i., suggesting their transport was primarily via cell-mediated uptake and migration to dLN (Figure 3.3G). 5 nm dextran also accumulated in dLN, though to a more modest extent, peaking at 24 hr p.i., suggesting a mechanism of passive lymphatic drainage (Figure 3.3G). Corroborating previous reports [101], 30 nm dextran, on the other hand, demonstrated sustained accumulation within dLN at significantly higher levels (5-20 fold) relative to all other tested tracer sizes at all tested time points p.i. (Figure 3.3G). By comparison, all tracer sizes exhibited dramatically lower concentrations in systemic tissues (Figure 3.3H). Over the size regimes tested, we consequently found a significant enrichment in tracer concentrations within dLN relative

to systemic tissues (Figure 3.3I). Most strikingly, the 30 nm tracer exhibited a three to six order of magnitude increase in dLN concentration relative that seen in systemic tissues at all measured time points and 50 and 500 nm tracers were found to be enriched by two to three orders of magnitude at 72 hours p.i. (Figure 3.3I).

#### *3.3.4 Remodeling of the Tumor Vascular Plexus with Tumor Growth*

In order to evaluate the effect of melanoma growth and remodeling on tracer clearance and resulting biodistribution from the dermis, we next evaluated the changes in the dorsolateral dermal vasculature induced by growth of the B16F10 melanoma in immune-competent C57Bl6 mice (Figure 3.4A). The melanoma vascular plexus exhibited branching irregularities as early as day 5 post tumor implantation and by day 7 exhibited a striking hyper-vascularized expansion (Figure 3.4B). This was reflected in a more than doubling of vascular volume and surface area between days 5 and 7 post tumor implantation (Figure 3.4C). The mean vessel diameter also increased throughout the course of tumor growth ( $p < 0.05$ ) to grow by as much as 75% by day 9 post tumor implantation (Figure 3.4D). The blood vasculature of growing B16F10 melanomas also exhibited a dramatic enhancement in permeability that increased with time post tumor implantation ( $p < 0.01$ ), as demonstrated by the accumulation of i.v. infused 5 nm dextran within the tumor interstitium at 4 hours p.i. (Figure 3.4E).

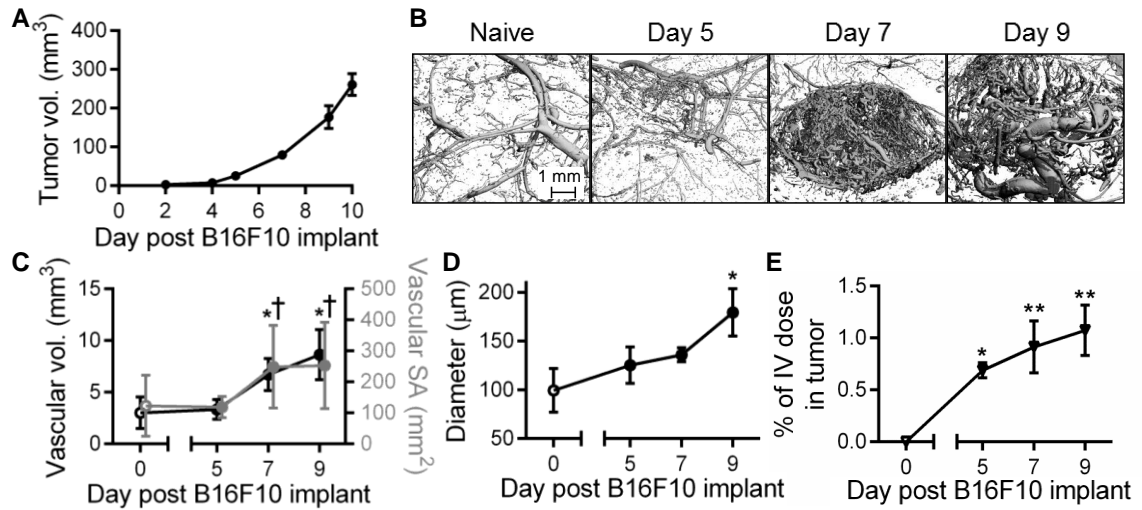


**Figure 3.4 B16F10 melanoma vascular remodeling.** Representative B16F10 melanoma growth curve (A) and micro-computed tomography 3D reconstructions of the tumor blood vasculature (B). Mean vascular volume (C), vascular surface area (SA, C), and vessel diameter (D). (E) Intratumoral accumulation of i.v. injected dextran. \* indicates significance relative to day 0 (naïve) and † relative to day 5 by ANOVA and post-hoc Tukey’s tests; n=3-5 mice per group.

### 3.3.5 Malignancy Increases Locoregional Tracer Exposure

Given these remodeling responses, we evaluated the rate of clearance from the growing melanomas at prescribed time points p.i. We found exposure (% injected) of 30-500, but not 5, nm tracers in all analyzed tumors was higher relative to that of naïve skin tissues (Figure 3.5A). When analyzed with respect to tumor stage, 50 and 500 nm tracers exhibited higher levels of tumor exposure (% injected) relative to naïve skin as early as 5 days post tumor implantation whereas increased tumor exposure (% injected) began only at day 7 post tumor implantation for 30 nm dextran (Figure 3.5B). Although not statistically significant, trends demonstrated that as a result of the slower clearance profiles from malignant tissues, the exposure (% injected) within tumors increased by only 20% with malignant progression for the 500 and 50 nm tracers for days 5, 7 and 9 post tumor implantation, but increased up to 50% more for the 30 nm tracer at days 7 and

9 (Figure 3.5C). 5 nm dextran exposure (% injected) in the tumor also increased by ~60% at day 5 post tumor implantation but then decreased thereafter, reaching ~40% of that seen in naïve skin in day 9 tumors (Figure 3.5C).

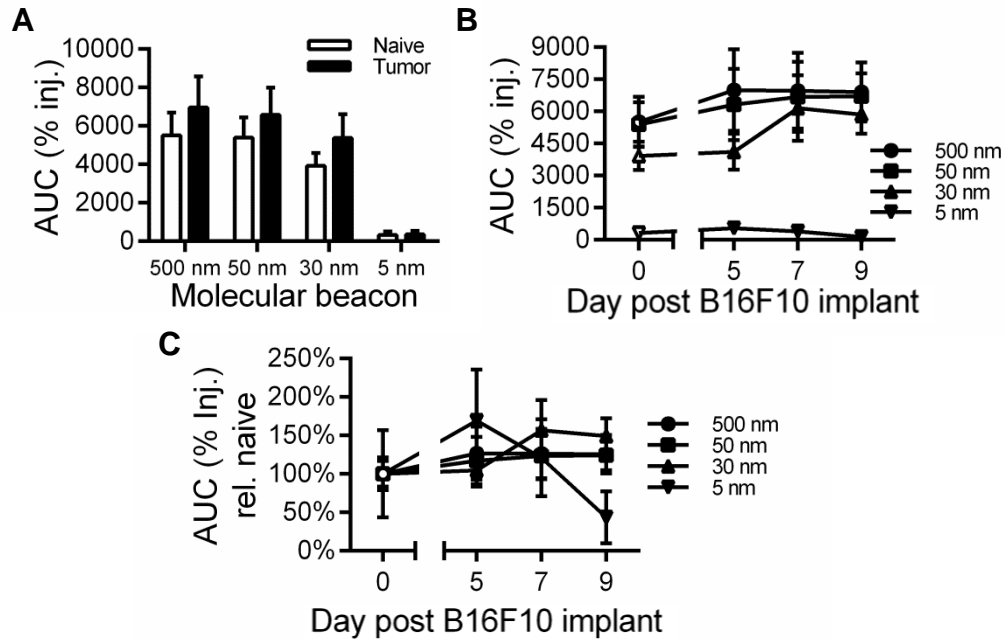


**Figure 3.5 Tracer exposure is modestly increased in the tumor interstitium. (A-B) Tracer exposure within the skin or melanoma site of injection. (C) Tracer exposure resolved by tumor day normalized to levels in naïve skin. AUC from 1-72 hr p.i. Results representative of n=6-9 mice per group performed in two to three independent experiments.**

### 3.3.6 Tumor Progression Reduces dLN Accumulation and Increases Systemic Exposure to Tumor-derived Factors

We next analyzed the biodistribution of systemically distributed tracers after infusion. At day 5 and 7 post tumor implantation we noted a surprising increase in exposure (% injected) in systemic tissues, which increased further by day 9 post tumor implantation for 5 nm dextran but not for other larger tracers (Figure 3.6A). Similar to the biodistribution seen after clearance from naïve skin (Figure 3.3F), the tissue subjected to

the most significant exposure (% injected) to 30, 50 and 500 nm tracers was the liver (Figure 3.6B). Contrastingly, whereas the 5 nm dextran disseminated primarily to the kidneys when cleared from the naïve skin tissue (Figure 3.3F), 5 nm dextran was found to also accumulate in tumor-bearing animals in the liver (Figure 3.6B). These results corresponded to increases in the maximum concentrations of tracer accumulating in the spleen, lungs, liver, and kidneys (Figure 3.6C). Notably, the maximum concentrations of 500 and 50 nm tracers were significantly non-zero in the lung tissue of day 9 melanoma-bearing animals in distinct contrast to naïve and day 5 and 7 post tumor implantation animals (Figure 3.6C). These concentration profile changes resulted in an initial increase in exposure (% injected) of 500 and 50 nm tracers in the spleen and 500 nm tracer exposure (% injected) in the liver days 5 and 7 post tumor implantation that was greatly diminished in day 9 tumors (Figure 3.6D). Exposure (% injected) in day 9 tumor bearing animals was reduced relative to naïve animals with respect to 30 and 5 nm tracers in the spleen and the 30 nm tracer in the liver, whereas liver exposure (% injected) to the 5 nm tracer was elevated relative to that seen in naïve animals at all tumor stages analyzed (Figure 3.6D). Accumulation of 30 nm dextran in the spleen and liver also occurred at earlier times post-injection in day 7 and 9 melanoma bearing animals, shifting from a 24 hour p.i. concentration peak in naïve animals to a peak in concentration at 1-4 hour p.i. (Figure 3.6E).

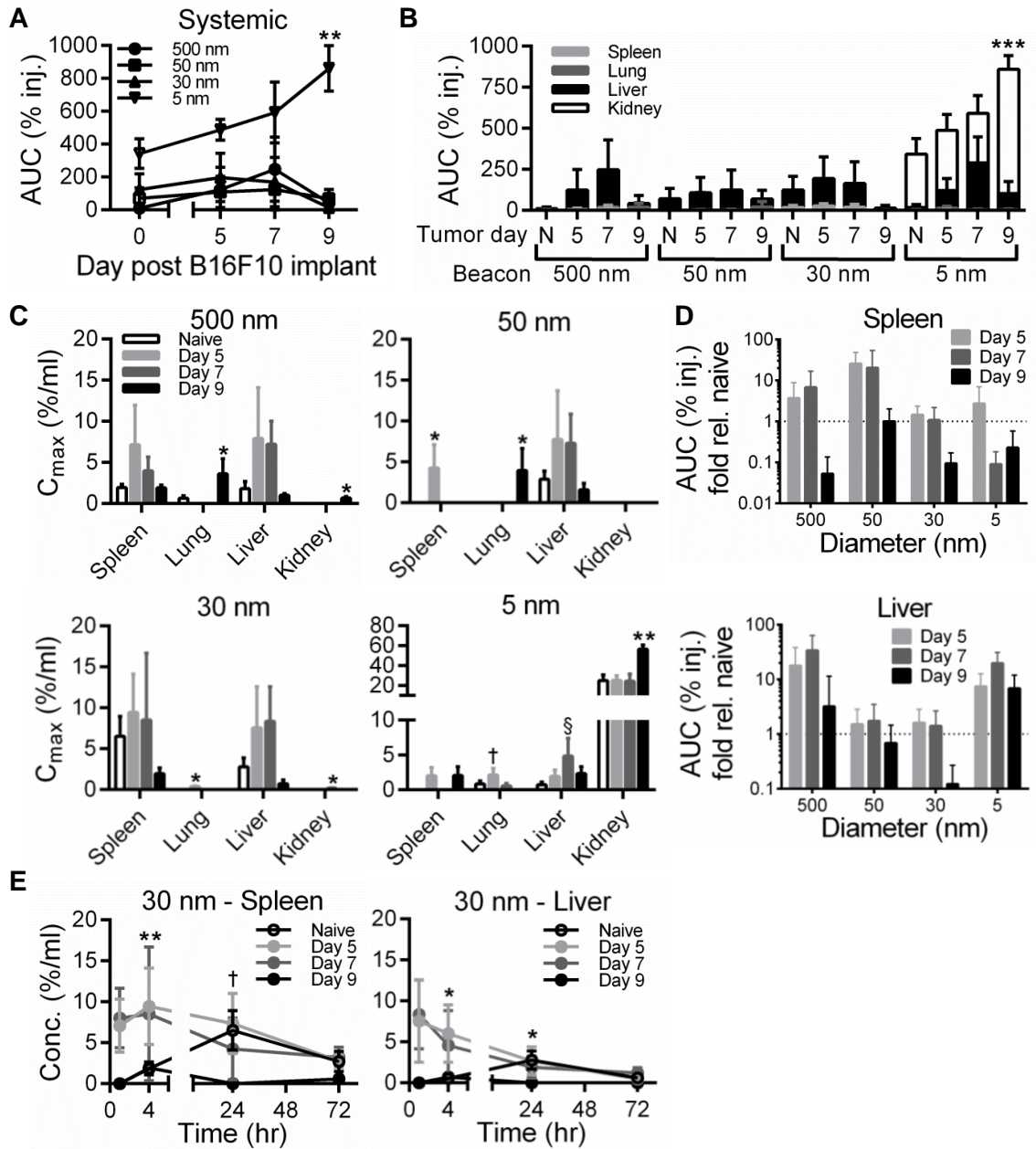


**Figure 3.6** Fluorescent tracers exhibit increased accumulation in systemic tissues with tumor progression. (A-B) Total tracer exposure in systemic tissues including the spleen, lungs, liver, and kidneys. \*\* indicates significance for day 9 vs naïve for same tracer. \*\*\* indicates significance for 5 nm tracer at day 9 in kidney vs all other groups by two-way ANOVA and post-hoc Tukey's tests. (C) Maximum tracer concentrations measured over 72 hr experimental timeframe. \* indicates significance for day 9 vs all other groups of same tissue and tracer, †  $p < 0.001$  for day 5 vs all other groups of same tissue and tracer, and §  $p < 0.001$  for day 7 vs all other groups of same tissue and tracer by one-way ANOVA with post-hoc Fisher's LSD tests. (D) Fold change in tracer exposure within spleen and liver tissues

**resulting from melanoma growth with respect to exposure measured after injection in naïve skin. (E) Time-resolved concentration of 30 nm tracer in spleen and liver tissues. † p<0.05 for naïve 24 hr time point vs 1 and 4 hr naïve time points, \*\* p<0.01 for day 9 4 hr time point vs all other day 9 time points, \* p<0.05 for naïve 24 hr time point and day 9 four hr time point vs all other by one-way ANOVA with post-hoc Fisher's LSD tests. AUC from 1-72 hr p.i. Results representative of n=6-9 mice per group performed in two to three independent experiments.**

When analyzed in a time-resolved fashion, as in naïve animals (Figure 3.3G), clearance through active cell-mediated trafficking via the lymphatics remained appreciable in day 5 tumor bearing animals, as indicated by significant concentrations of the 500 and 50 nm tracers within dLN only 72 hours p.i (Figure 3.7A-B). This transport activity, however, was abolished in day 7 and 9 tumors (Figure 3.7A-B). Similarly, passive lymphatic drainage was also decreased with tumor progression, as indicated by reduced levels of sustained 5 and 30 nm tracer concentrations in dLN at all times p.i. (Figure 3.7C-D). As a result, dLN exposure (concentration) to all tracer sizes was significantly attenuated in tumor-bearing animals relative to naïve animals (Figure 3.7E-F). Specifically, relative dLN exposure (concentration) to all tracer sizes decreased rapidly with tumor progression, reaching near zero levels by day 7 for 5 and 50 nm tracers and for all tracer sizes at day 9 post tumor implantation (Figure 3.7F). Notably, however, exposure (concentration) of 30 nm tracers at even their most attenuated levels (day 9 post tumor implantation) remained significantly higher (nearly two-fold) than that of all other tracer sizes in even naïve animals (Figure 3.7E).

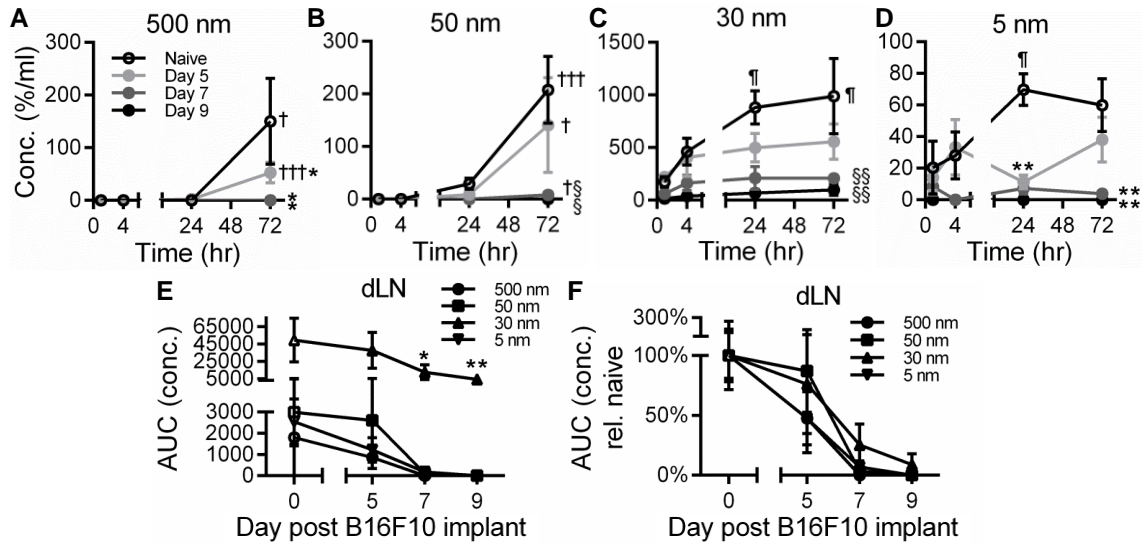


**Figure 3.7 Tumor progression reduces tracer accumulation within TDLN. (A-D) Time-resolved tracer concentrations within TDLN. † indicates significance relative to all other time points for same group, ¶ relative to 1 hr time point for same group, \* relative to naïve, and § relative to naïve and day 5 groups by one-way ANOVA with post-hoc Fisher’s LSD test. Tracer exposure within dLN is attenuated by tumor growth (E) relative to naïve skin (F). \* indicates significance relative to all other tracers within same tumor day group by one-way ANOVA with post-hoc Fisher’s LSD test. AUC from 1-72 hr p.i. Results representative of n=6-9 mice per group performed in two to three independent experiments.**

When comparing the relative levels of exposure (concentration) of different tracer sizes with respect to tumor stage in dLN versus systemic tissues, we found an increase in the relative extents of transport of tracers 500, 50, and 5 nm in size into systemic tissues as indicated by a decreasing ratio of dLN to systemic concentration AUC (Figure 3.8A-C). While the 30 nm tracer exhibited a reduced level of accumulation within dLN post tumor injection (Figure 3.7E-F), exposure (concentration) in dLN still remained two to three orders of magnitude higher relative to that seen in systemic tissues (Figure 3.8A). When normalized relative to the measured ratios of naïve animals, the 500 nm tracer experienced the most significant redirection into systemic relative to dLN tissues at all tumor stages analyzed (Figure 3.8B). However, both the 50 and 5 nm tracers also

exhibited a bias towards increased accumulation in systemic tissues rather than dLN by days 7 and 9 post tumor implantation (Figure 3.8B). Changes in the accumulation profile of 30 nm dextran, however, were less pronounced, even in day 9 tumor-bearing animals (Figure 3.8B). This is because whereas for 500, 50, and 5 nm tracers an increasing proportion accumulates in systemic tissues as the disease progresses, the 30 nm tracer primarily accumulates (>99%) instead in dLN at all tumor growth stages analyzed (Figure 3.8C).

When assessing the relative exposure of each tracer size in individual tissues, we found changes in size-dependent accumulation profiles that result from tumor formation and growth, despite no substantial differences in the relative levels of exposure within the skin versus tumor after injection (Figure 3.8D). Specifically, 500, 50, and 30 nm tracers each accounted for approximately a third of the total exposure at the site of injection irrespective of tumor stage (Figure 3.8D). The 5 nm tracer on the other hand exhibited little to no local exposure (Figure 3.8D), consistent with its rapid clearance (Figure 3.3A). Irrespective of tumor stage, 30 nm was the predominant tracer size that accumulated within dLN and the proportion of 30 nm tracer of total accumulating within the dLN increased with tumor growth (Figure 3.8D). Strikingly, the livers of melanoma-bearing animals day 5 and 7 post tumor implantation exhibited profiles of exposure strikingly similar to those seen within the tumor (albeit with higher 5 nm tracer levels) rather than naïve liver (Figure 3.8D). Day 9, but not 5 or 7, melanoma-bearing animals also exhibited lung exposure profiles more similar to that of the tumor rather than naïve lung, with exposure to only higher molecular weight tracers (equally shared between 500 and 50 nm tracers) versus predominantly 5 nm, respectively (Figure 3.8D).

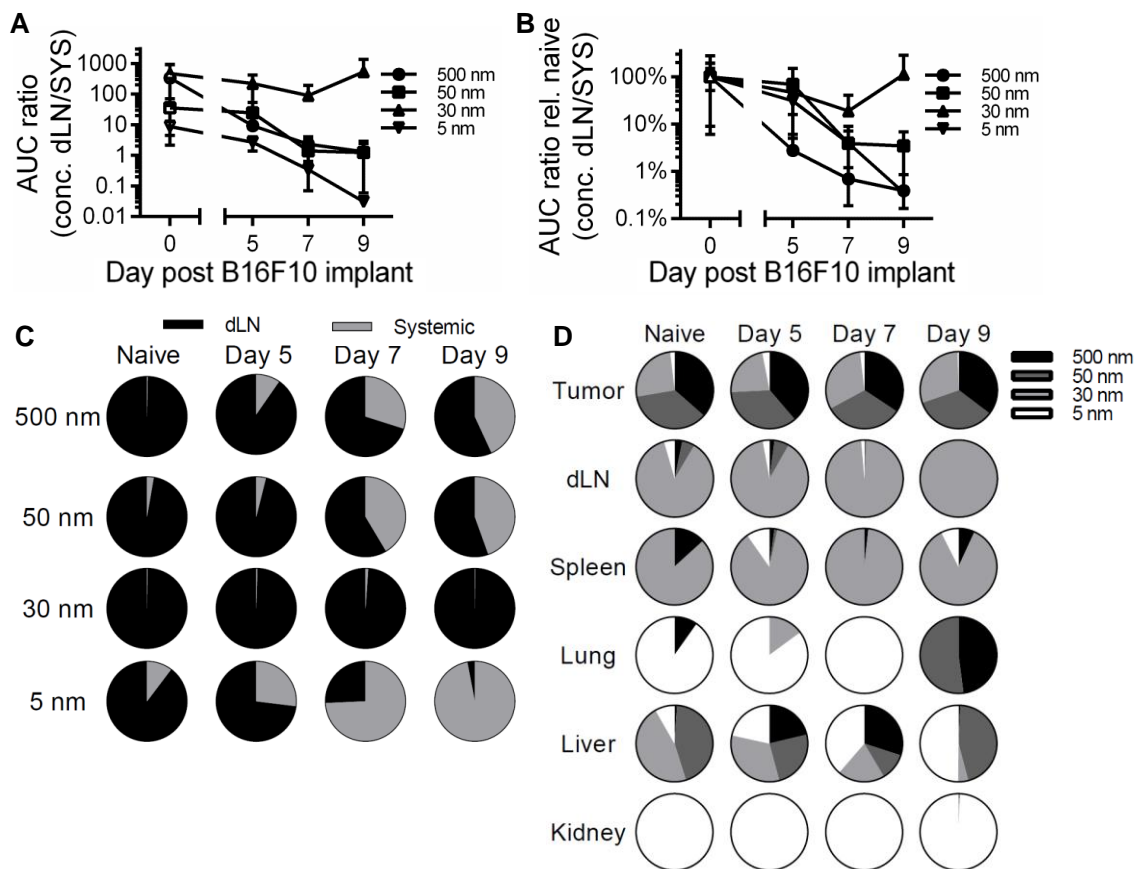


**Figure 3.8 Melanoma disease progression has no effect on the proportion of 30 nm tracer exposure in TDLN while increasing the exposure of other tracer sizes in systemic tissues. (A) Ratio of accumulating tracer concentrations within dLN to systemic tissues with respect to tumor stage and (B) normalized to naïve skin. (C) Proportion of dLN versus systemic tissue exposure (concentration). (D) Proportion of accumulating tracers with respect to hydrodynamic size. AUC from 1-72 hr p.i. Results representative of n=6-9 mice per group performed in two to three independent experiments.**

### 3.4 Discussion

The deleterious effects of cancer are not limited to the primary tumor itself, as evidenced by the sentinel lymph node's role in tumor immune suppression [20, 48] as well as the high number of cancer-associated complications and mortalities associated with both metastasis [102, 103] and thrombosis [104, 105]. Distant intercellular signaling can occur even prior to metastasis to precipitate such effects, for example via remodeling

of sentinel lymph nodes [18], VEGFR1+ haematopoietic progenitor cell recruitment to pre-metastatic niches [5], and secretion of tumor-derived pro-coagulants and cytokines driving thrombosis [106]. Paracellular communication between cancer cells, their secreted factors, and the endothelium within the malignant melanoma microenvironment that regulate vascular permeability thus have a putative role in a myriad of pathways implicated in disease progression.

In numerous cancer types including melanoma [46], breast carcinoma [107-109], and prostate carcinoma [110], amongst others [111, 112], circulating inflammatory cytokine [110], chemokine [108, 113], enzyme [107], exosome [46], and/or microvesicle [111] levels and qualities are altered relative to healthy controls and with respect to disease stage in both patients and pre-clinical tumor models. These changes have been attributed to both higher production of such factors within the tumor [5, 107, 113] and extratumoral host tissue response to tumor growth [114]. Our data support the notion that increased systemic exposure to TSF may accompany tumor growth (Figure 3.6) in a manner independent of TSF abundance since higher levels of exposure in systemic tissues were noted in animals with late stage malignancies despite the same amount of tracer being infused into each animal. These changes occurred before formation of apparent metastases, suggesting that altered rates, magnitudes, and mechanisms of TSF clearance arise as a result of tissue remodeling within the primary tumor microenvironment.

Increased systemic exposure to intratumorally infused tracers (Figure 3.6) accompanied enhanced intratumoral accumulation of a systemically administered tracer (Figure 3.4E). For example, in as early as day 5 lesions, the exposure of spleen and liver

tissues to large 500 and 50 nm tracers was elevated (Figure 3.6B) approximately two- to 30-fold (Figure 3.6D). Reduced exposure was seen in animals with more advanced (day 9) lesions (Figure 3.6B-D) and is likely the result of interstitial matrix remodeling within the tumor [60, 68] leading to larger tracer entrapment since levels of systemic exposure to 5 nm dextran continued to increase at this tumor stage (Figure 3.6A-B). Liver and spleen accumulation of large (30-500 nm) tracers peaking at 1-4 hours p.i. in animals bearing early stage (day 5 and 7) malignancies rather than 24 hr in naïve animals (Figure 3.6E) also supports the concept that these increases in systemic exposure were the result of direct tracer uptake into the blood rather than enhanced lymphatic clearance and return to the systemic circulation. Increased tumor vascular permeability, as has been previously reported for this and other tumor models [115-117], thus may also enhance blood-mediated clearance that manifests as increased tumor-derived factor exposure in systemic tissues. Injection resulted in a small (~ 1 mmHg) increase in interstitial pressure that was similar between naïve and tumor tissues that returned to pre-injection levels after removal of the needle (data not shown). However, it should be noted that measured tracer pharmacokinetics could differ from those of native tissues *in vivo*.

Our data support the concept that tumor growth and remodeling confer the potential of TSF to mediate signaling in distant tissues that is absent in healthy animals. Tumor-secreted microparticles, including exosomes and microvesicles, which range in hydrodynamic diameter from 30-100 nm and 100-1000 nm [118], respectively, have reported capacities to support neovascularization [119], extracellular matrix remodeling [28], and immunomodulation [109]. Here we demonstrate 500 and 50 nm tracers cleared from the tumor to accumulate at elevated levels in the liver and spleen (Figure 3.6D).

Moreover, we found these tracers to accumulate appreciably within the lungs of animals with advanced (day 9) malignancies (Figure 3.6C), a redirection in their biodistribution that occurred concurrently with attenuated transport to TDLN (Figure 3.7). TSF signaling that would take place within dLN in naïve animals appears to instead be redirected to lungs of tumor-bearing animals. Small to intermediate size biomolecules secreted by tumors such as peptides, proteins, and other biopolymers have also been implicated in a multitude of roles that exacerbate disease progression [109, 113]. We provide evidence that exposure of small molecules ~5 nm in hydrodynamic size is also appreciably increased in systemic relative to dLN tissues in tumor-bearing animals (Figure 3.6). Overall, accumulation of 500, 50 and 5 nm tracers shifted significantly from dLN to systemic tissues over the time course of disease progression evaluated here (Figure 3.8). As a result, profiles of TSF tracer accumulation in the liver and lung diverged from that seen in naïve animals and instead more closely mirrored those of the primary tumor (Figure 3.8D). This suggests that signaling processes active within the tumor microenvironment have the potential to be operational in systemic tissues of melanoma-bearing animals and may significantly regulate and negatively influence the course of disease progression. They also indicate that therapeutic agents administered intralesionally, for example oncolytic immunotherapy talimogene laherparepavec [120], may also result in significant signaling activity outside of the primary tumor in distributed systemic tissues.

The effect of melanoma growth on tracer clearance and biodistribution diverged with respect to its effects on blood versus lymphatic mediated transport. As opposed to increased levels of uptake via the blood vasculature, melanomas at day 7 and later post

implantation demonstrated a dramatic attenuation in lymphatic function, which is regulated by local inflammatory [121] and biomechanical [122] signaling, as evidenced by reduced levels of tracer accumulation within dLN relative to that seen in naïve animals (Figure 3.7C-F). Parallel reductions in lymphatic-mediated cellular migration to dLN, which are regulated by flow-organized chemokine gradients and vascular signaling [123-125], were also observed (Figure 3.7A-B, E-F). These reductions coincided with tumor vascular volume and surface area doubling relative to naïve skin tissues at day 7 and 9 post tumor implantation (Figure 3.4C). In line with previous reports [101], the predominant lymph-draining tracers were found to be 30 nm in size in both healthy (Figure 3.3D-E,G) and malignant (Figure 3.7E) skin. Interestingly, despite reduced total levels of dLN accumulation, the relative accumulation of 30 nm tracer in dLN relative to systemic tissues remained relatively unchanged. This indicates that despite reductions in lymphatic transport function (Figure 3.7), TSF approximately 30 nm in diameter such as exosomes and large protein complexes continue to primarily signal extratumorally within TDLN (Figure 3.8C-D). These results also underscore the potential utility of drug formulations ~30 nm in size to accumulate substantially in sentinel lymph nodes when intralesionally administered.

### **3.5 Conclusions**

In summary, we have demonstrated that tracer clearance from primary melanomas is concurrently altered with tumor vascular remodeling and results in distinct biodistribution profiles relative to those seen in healthy animals. These are the first measurements juxtaposing the size-resolved biodistribution profiles of tumor-derived factors in naïve versus tumor-bearing animals to elucidate the influence of disease. Our

results highlight the role lymphatic drainage function plays in enriching TSF accumulation in dLN. Furthermore, these data suggest that melanoma growth redistributes TSF signaling to systemic tissues by compromising transport barriers in healthy tissues and that despite attenuation of total levels of accumulation, previously developed principles of size-dependent lymph node drug targeting are conserved in melanomas over the course of disease progression. Our findings contribute evidence that tumor vascular remodeling not only manifests in the enhanced permeability and retention effect in solid tumors, but also increased access of factors from the tumor interstitium to systemically distributed tissues. These results will inform the rational design of sentinel lymph node-targeted drug delivery strategies as well as future studies on how angioplastic therapy might be used to mitigate the pathological effects of TSF in disease progression.

## **CHAPTER 4. Flexible macromolecule versus rigid particle retention in the injected skin and accumulation in draining lymph nodes are differentially influenced by hydrodynamic size [179]**

### **4.1 Introduction**

Immunotherapy is increasingly employed for the treatment of a variety of pathologies, such as cancer and autoimmune disease. Accordingly, biomaterial-based formulation approaches have been explored to improve the bioactivity and therapeutic efficacy of numerous immunotherapeutic interventions.[126-128] These include strategies to co-deliver multiple immunotherapeutic drugs,[129, 130] provide sustained and/or controlled drug release,[131-133] and improve drug circulation half-lives,[129, 134, 135] the success of which are critically influenced by the adequate and selective accumulation or retention of drug within target tissues. To this end, biomaterials have been used to improve drug bioavailability within healthy[136, 137] and diseased skin,[138-140] key targets in vaccine, skin graft, and cancer immunotherapy applications. Notwithstanding approaches leveraging the enhanced permeability and retention effect for tumor-enhanced delivery after intravenous injection, dermal delivery is largely accomplished via direct injection.[138, 139] Consequently, designing drug carriers to achieve prolonged retention at the site of injection has been widely explored to improve drug bioavailability and potency.[136, 139]

LN's are emerging as key immunotherapeutic targets given their role in directing adaptive immunity and tolerance.[70, 141, 142] Notably, the efficacy of infectious disease and cancer vaccines is improved by LN-targeting[48, 80, 91, 143, 144] resulting from the localized modulation of immunological signaling to alter adaptive immune

response. As an example of such an approach, delivery to melanoma dLN mediated by lymphatic-draining synthetic polymer nanoparticles improves adjuvant activity, in particular increasing dendritic cell maturation as well as Th1 and anti-tumor CD8+ T cell immunity, resulting in reduced tumor growth, a response lost by adjuvant delivery in a non-targeted manner or to LN not draining the melanoma.[48] In another example, corticosteroid delivery to skin graft dLN mediated by encapsulation within block copolymer micelles has demonstrated success in delaying rejection.[145] Localizing drug activity to dLN can thus provide significant advantages to immunotherapy in improving immunological outcomes in addition to achieving dose sparing to minimize off target effects/toxicities.[146, 147]

Given the local immunological signaling associated with pathogenesis in both the diseased skin and its dLN, therapeutic immunomodulation in either the skin or its dLN or, conversely, in both tissues simultaneously is potentially desirable for numerous therapeutic scenarios. However, despite recent advances in targeted immunotherapeutics using biomaterials,[143, 144, 146, 148] there is limited understanding of how carrier design simultaneously affects retention and accumulation in both the skin injection site and its dLN. Previous studies have explored the effects of biomaterial carrier size[91, 92], charge[149, 150], hydrophobicity[151, 152], and shape[153, 154] on various aspects of transport, cellular uptake, and adaptive immune response. How the coupled effects of both size and form influence carrier transport, especially with respect to dermal and dLN targeted applications, however, remains to be described. Since biomaterial-based delivery systems are increasingly explored for immunotherapeutic delivery[128, 155], we sought to analyze the differences in profiles of spherical particulate versus macromolecular

retention as a function of hydrodynamic size in the site of dermal injection as well as the corresponding extent of accumulation in dLN and systemic off-target tissues. This was achieved by implementing a panel of tracers comprised of inert polymers (polystyrene particles and dextran macromolecules) that are resistant to hydrolysis and proteolytic degradation that span a size range of widely used drug carrier systems and are labeled with fluorophores with minimal tissue absorbance and spectral overlap.[62] Tracers were intradermally infused into naïve C57Bl6 mice and their biodistribution among the skin injection site, dLN, and systemic tissues was examined by endpoint analysis and fluorescent measurement of homogenized tissues. Our results demonstrate that chain-like, flexible macromolecular but not rigid, spherical particulate retention within the skin injection site is size-dependent, that enrichment within the skin relative to systemic tissues increases with size for both macromolecules and particles, and macromolecules accumulate in dLN more extensively and selectively than rigid, spherical particles.

## **4.2 Materials and Methods**

### *4.2.1 Fluorescent Tracers*

FITC (Fluorescein isothiocyanate) labeled 2 MDa dextran was purchased from Sigma-Aldrich (St. Louis, MO, USA). 500, 50, and 25 nm fluorescent (580/610 nm, 660/680 nm, and 625/645 nm excitation/emission, respectively) carboxylate-modified polystyrene microspheres and 70 and 40 kDa fluorescent (490/520 nm and 555/585 nm excitation/emission, respectively) dextrans were purchased from Thermo Fisher Scientific (Waltham, MA, USA). 500 kDa or 10 kDa amine-dextrans (Sigma-Aldrich) were covalently labeled by incubation in 0.1 M NaHCO<sub>3</sub> buffer at pH 8.4 for 4 hr with Alexa Fluor 700 N-hydroxysuccinimide (NHS) ester or Alexa Fluor 610-X NHS-ester

dye (Thermo Fisher Scientific), respectively. Individual fluorescent dextran conjugates were purified from unreacted free dye and confirmed to be free of unconjugated dye by Sepharose CL-6B gravity column chromatography as previously described.[62] All reagents were maintained and used under sterile conditions. Hydrodynamic sizes of individual fluorescently conjugated tracers were measured by dynamic light scattering using a Zetasizer Nano ZS (Malvern Instruments Ltd, Malvern, United Kingdom), except for the 25 nm polystyrene spheres for which the manufacturer's sizing data was used due to fluorophore incompatibility with our Zetasizer Nano ZS.

#### 4.2.2 *Biodistribution Experiments and Analysis*

C57Bl6 mice were purchased from Jackson Laboratories (Bar Harbor, ME, USA). All protocols were approved by the Institutional Animal Care and Use Committee. 30  $\mu$ L of fluorescent tracer solution normalized for equivalent material volumes using the respective radius or hydrodynamic radius (either  $1.2 \times 10^8$  500 nm spheres,  $7.9 \times 10^{11}$  50 nm spheres, 23.8  $\mu$ g of 500 kDa AF700-dextran, and 3  $\mu$ g of 10 kDa AF610-dextran (n=9 for 24 hr, n=9 for 72 hr in 6 independent experiments); or  $8.3 \times 10^{11}$  25 nm spheres and 1.38  $\mu$ g of 2 MDa FITC-dextran (n=3 for 24 hr, n=6 for 72 hr in 4 independent experiments); or  $8.3 \times 10^{11}$  25 nm spheres, 1.93  $\mu$ g of 40 kDa TRITC (Tetramethylrhodamine isothiocyanate)-dextran and 0.81  $\mu$ g of 70 kDa FITC-dextran (n=3 for 24 hr, n=3 for 72 hr in 4 independent experiments)) in saline was infused intradermally into the shaved lateral dorsal skin using a syringe pump at a rate of  $\sim$ 300 nL per sec as previously described.[62] Tracers with similar labels were injected into separate animal cohorts. 24 or 72 hr post injection (p.i.), the brachial LNs ipsilateral and contralateral to the site of injection, the skin at the injection site, and the spleen, lungs, liver, and kidneys were

harvested and homogenized in D-PBS using 1.4 mm acid washed zirconium grinding beads (OPS Diagnostics LLC, Lebanon, NJ, USA) with a FastPrep-24 Automated Homogenizer (MP Biomedicals, Santa Ana, CA, USA). Tissue homogenate fluorescence was measured using a Synergy H4 BioTek plate reader (BioTek Instruments Inc.), compensation for fluorescence overlap was applied, and fluorescent tracer standard curves were made in individual tissue homogenates. Concentrations were calculated as the percent of tracer injection amount per whole tissue volume (%/mL). Prism 6 (GraphPad Software Inc., La Jolla, CA, USA) was used to calculate exposure from the area under the curve (AUC) of tracer concentrations measured between 0 and 72 hr. Error propagation analysis was used to calculate AUC standard error. Systemic tissues used in ratio calculations included the spleen, lungs, liver, and kidneys. Due to high systemic tissue (spleen, lungs, liver, and kidneys) autofluorescence around FITC wavelengths, FITC labeled tracers (70 kDa and 2 MDa dextrans) were not included in concentration ratio analyses.

#### 4.2.3 *Statistical Analysis*

Data are represented as the mean with standard error. Statistics were calculated and linear regressions were performed using Prism 6 (GraphPad Software Inc.). Statistical significance was defined as  $p < 0.05$  following Mann-Whitney U tests or one-way ANOVA followed by Fisher's Least Significant Difference (LSD) test. One, two, and three symbols denoting statistical significance represent  $p < 0.05$ , 0.01, and 0.001 respectively, unless otherwise specified.

### **4.3 Results**

#### 4.3.1 Skin Retention versus Exposure in Systemic Tissues Increases with Increasing Tracer Size

A panel of eight dextran and polystyrene sphere tracers spanning 5-54 and 25-500 nm in hydrodynamic diameter, respectively (Figure 4.1A-B), was used to interrogate the effect of size versus form on skin retention and biodistribution. Because we wanted to explore whether size-based principles of dLN drug delivery are similar for macromolecule- and particle-based delivery systems, two size-matched tracer subsets in the size range of passive lymphatic transport (25 nm polystyrene vs 30 nm dextran and 50 nm polystyrene vs 54 nm dextran) were used to enable the direct comparison of carrier form on dermal retention and dLN accumulation. 5 nm dextran and 500 nm polystyrene spheres were also included as benchmarks for modes of tracer transport from the interstitium besides passive lymphatic uptake for tracers with low retention at the site of injection due to absorption into the bloodstream and requiring active cell-mediated transport from the site of injection to the dLN, respectively. Measured profiles of biodistribution (Figure 4.2A) and size-exclusion column chromatography elution (Figure 4.2B) confirmed that individually versus co-infused tracers behaved identically with minimal to no interaction or aggregation effects.

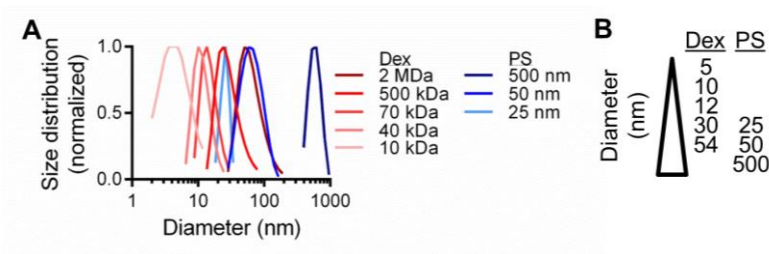


**Figure 4.1 Measured hydrodynamic sizes (A) of fluorescent dextran (Dex) and polystyrene sphere (PS) tracer panel (B).**

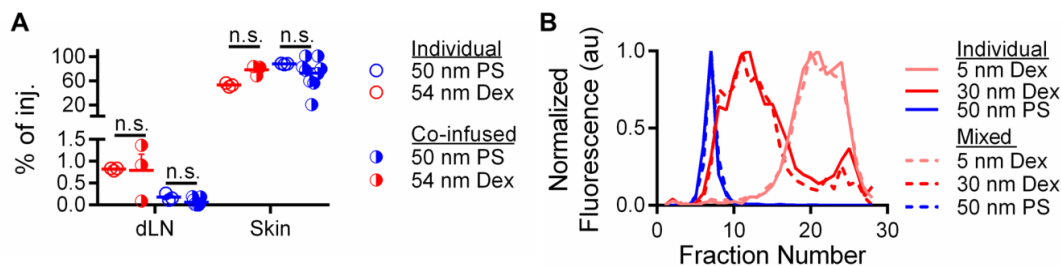


**Figure 4.2 Characterization of individual versus mixtures of fluorescent tracers. (A) Measured dLN accumulation and dermal retention of dextran (Dex) and polystyrene spheres (PS) either individually infused into the dorsal skin of separate animals or with tracers mixed together and co-infused into the dorsal skin. (B) Comparison of tracer molecules after addition to a CL-6B column (Sigma-Aldrich) individually or mixed.**

After infusion into the skin, the smallest (5 nm) dextran was cleared most quickly from the injection site, with less than 5% of the injected amount remaining after 24 hr and only around 3% left at 72 hr p.i. (Figure 4.3A). In contrast, around 20-40% of the 10 and 12 nm dextrans, 50% of the 30 nm dextran, and 85-100% of the 25-500 nm polystyrene sphere and 54 nm dextran tracers were measured in the dermis at 24 and 72 hr p.i. (Figure 4.3A). As a result, the concentrations of the larger tracers (25, 50, 54, and 500 nm) in the skin were significantly greater than that of the 5, 10, and 12 nm dextran at 24 and 72 hr p.i. (Figure 4.3A). When also considering the concentration of tracer that accumulated in systemic tissues, the relative amount of tracer localized to the skin tissue surrounding the site of skin injection versus systemic organs increased with tracer size for dextrans 24 hr p.i. ( $p=0.050$ ) and increased for both dextrans ( $p=0.006$ ) and polystyrene spheres ( $p=0.001$ ) 72 hr p.i. (Figure 4.3B). The fold enrichment also increased over time, presumably due to tracer elimination via excretion,[156] save for the 25 nm polystyrene spheres (Figure 4.3B).

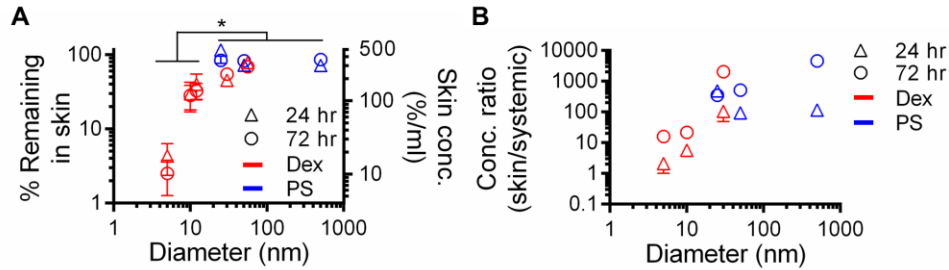


**Figure 4.3 Tracer retention in skin injection site increases with macromolecular but not particle hydrodynamic size but relative enrichment relative to systemic tissues increases with size for all tracer forms. (A) Percent of injection amount and resulting concentration of tracer within the dermal injection site 24 and 72 hr p.i.. (B) Ratio of tracer concentrations within the injected skin versus systemic tissues (spleen, lungs, liver, and kidneys) 24 and 72 hr p.i.. \* indicates significance for 5-12 vs 25, 50, 56, and 500 nm tracers at 24 and 72 hr p.i. by one-way ANOVA and post-hoc Fisher's LSD tests.**

#### 4.3.2 Accumulation within dLN is Greatest for Macromolecules and Increases with Size over 72 hr for Particles, albeit at Lower Levels of dLN-Specific Enrichment Relative to Macromolecules

We next evaluated the extent of tracer accumulation within LN draining the injected skin. We found 30 nm dextran to exhibit the highest levels of dLN accumulation (~2% of injected tracer, approximately 10-20 fold higher than 5 nm dextran or polystyrene sphere tracers of other sizes) at 24 and 72 hr p.i. (Figure 4.4A). Dextrans 10, 12, and 54 nm in hydrodynamic diameter also accumulated within dLN at appreciable levels (~1%), approximately half the amount of 30 nm dextran and when similarly sized, accumulated within LN at 5-10-fold higher levels relative to polystyrene spheres (Figure 4.4A). 5 nm dextran, on the other hand, and 25, 50, and 500 nm polystyrene spheres accumulated in dLN the least at both 24 and 72 hr p.i. (Figure 4.4A). However, the difference in dLN accumulation between 24 and 72 hr p.i. significantly increased with polystyrene sphere size ( $p=0.037$ ) presumably due to the increasing dependency on cell-mediated trafficking to dLN,[92] with 500 nm polystyrene spheres exhibiting an almost

40 fold change (Figure 4.4B). The dextran tracers' dLN accumulation, however, remained relatively constant from 24 to 72 hr p.i. (Figure 4.4B), suggesting a sustained, primarily passive lymphatic transport mechanism.[157] When compared to concentrations of tracers accumulating in systemic tissues, the 30 nm dextran demonstrated the highest dLN/systemic ratio at 24 and 72 hr p.i., around one to two orders of magnitude over that of the other dextran tracers, and interestingly, an order of magnitude higher than the similarly sized 25 nm polystyrene sphere tracer (Figure 4.4C). Considering concentrations of tracers accumulating in dLN relative to those in both skin and systemic tissues, dextran tracers exhibited an order of magnitude higher dLN enrichment, while the polystyrene tracers exhibited ratios at or less than one (Figure 4.4D). We also found higher levels of 30 nm dextran tracer accumulation within dLN relative to the skin and systemic tissues as compared to size-matched polystyrene spheres at 24 hr p.i. (Figure 4.4D).

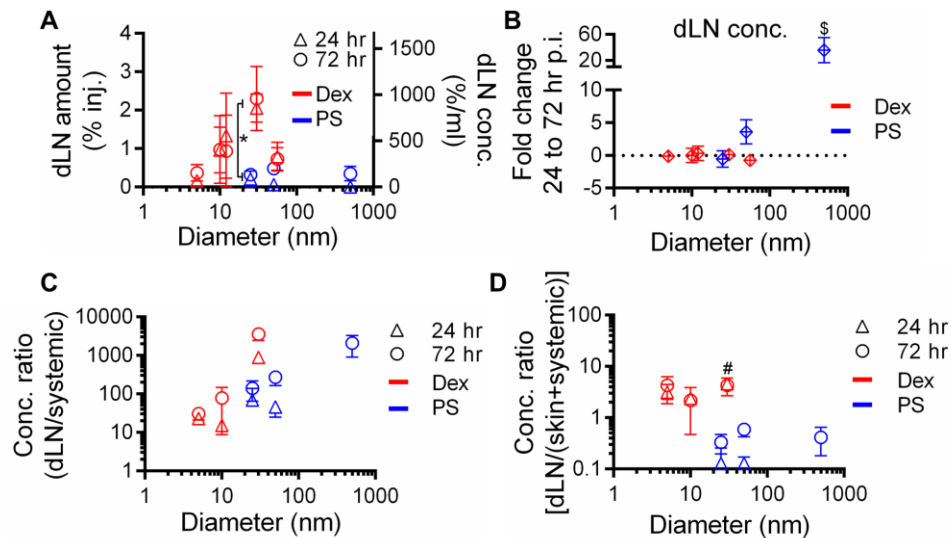


**Figure 4.4 Tracer accumulation within dLN is greatest for macromolecules, increases most appreciably over time with increasing particle size, and is the most specifically enriched relative to other tissues for macromolecules. (A) Percent of**

**injection amount and resulting concentration of tracer within dLN after dermal injection 24 and 72 hr p.i.. (B) Fold change in dLN tracer concentrations from 24 to 72 hr p.i.. (C) Ratio of accumulated tracer concentrations within the dLN versus systemic tissues at 24 and 72 hr p.i.. (D) Tracer accumulation within dLN versus the skin injection site and systemic tissues at 24 and 72 hr p.i.. \* indicates significant for 25 vs 30 nm tracers by Mann-Whitney U tests, \$ indicates significance for 500 vs 50 and 25 nm tracers and # indicates significance for 30 vs 25, 50 and 500 nm tracers at 24 and 72 hr by one-way ANOVA and post-hoc Fisher's LSD tests. The level of 500 nm tracer accumulation within dLN at 24 hr p.i. was not detectable.**

#### *4.3.3 Macromolecular but not Particulate Tracer Exposure within the Skin and dLN is Size-dependent*

Lastly, we sought to evaluate the effects of tracer size and form on total exposure (e.g., AUC) within the site of skin injection and the dLN from 0-72 hr p.i.. We found that skin exposure to injected dextran but not polystyrene sphere tracers increased with hydrodynamic size ( $p=0.022$ ), reaching levels similar to that measured for all polystyrene tracers (Figure 4.5A). The dextrans 10-54 nm in hydrodynamic diameter also exhibited the highest levels of exposure within LN draining the injected skin, levels up to four-fold higher than those measured in the skin itself and greatest for the 30 nm dextran tracer (Figure 4.5B). Contrastingly, polystyrene sphere tracer exposure within the injected skin was similar to the largest (54 nm) dextran tested and dLN exposure was similar irrespective of size and at levels similar to those found for the dextran tracer exhibiting the lowest exposure in dLN (5 nm, Figure 4.5A, B). Accordingly, the exposure of size-matched dextran and polystyrene tracers was similar in the skin but significantly greater (~3 to 10-fold) in dLN for both sizes of dextrans relative to the polystyrene spheres (Figure 4.5B-C). Taken together, when simultaneously considering exposure within the dLN versus skin, three separate tracer groups of dLN versus skin exposure emerged: the small macromolecule 5 nm dextran exhibited low exposure in both the dLN and skin, intermediate sized macromolecules (10-54 nm dextrans) exhibited high exposure in both

dLN exposure and skin (10-20-fold and 5-10-fold relative to 5 nm dextran, respectively), and particles of all tested sizes (25-500 nm polystyrene tracers) displayed low dLN exposure at levels similar to those seen with 5 nm dextran but 7-10-fold higher levels of skin exposure (Figure 4.5D).

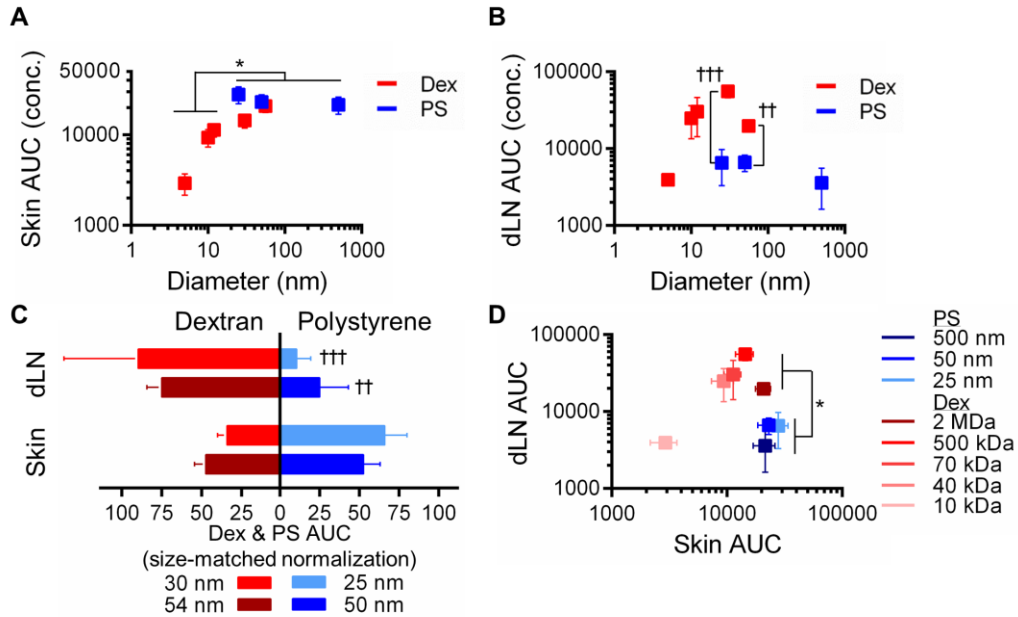


**Figure 4.5 Tracer exposure within dLN and skin is size and form dependent.** AUC of measured concentration profiles from 0 to 72 hr p.i. in (A) skin and (B) dLN. (C) Tissue exposure for size-matched dextran (red) and polystyrene spheres (blue) as percentage of total for both forms for the skin (left) and dLN (right). (D) AUC of tracers in skin and dLN. \* indicates significant for 5-12 vs 25, 50, and 500 nm tracers by one-way ANOVA and post-hoc Fisher's LSD tests, † indicates significance for 30 vs 25 and 56 vs 50 nm tracers by Mann-Whitney U tests.

#### 4.4 Discussion

Biomaterials-based formulation strategies offer numerous advantages for the maximization of immunotherapeutic drug bioavailability in target tissues[92, 132, 134, 139] while simultaneously limiting off-target effects.[139, 146, 147] Design criteria for increasing the efficiency and selectivity of agent delivery or retention in order to prolong

drug exposure in skin and dLN, tissue targets in a variety of immunotherapeutic regimens (e.g., intralymphatic immunotherapy[95, 96] as well as intradermal (or intralesional) injection for allergic contact dermatitis and plaque psoriasis[97] or oncolytic virus therapy in melanoma,[98] respectfully), using biomaterials thus has the potential to increase treatment efficacy, reduce off-target effects, and potentially eliminate the need for repeated local injections.[158-160]

In this study, we explored the effects of macromolecular versus particulate size on profiles of skin retention and selectivity of dLN accumulation. A range of fluorescent tracer sizes relevant to engineered macromolecular and particulate drug carriers was implemented and the time points of analysis (24 and 72 hr p.i.) were chosen to allow the interrogation of both lymphatic transport mechanisms: cell-mediated uptake and migration which peaks 2-4 d p.i.[100, 161] versus passive lymphatic drainage from the interstitial injection site.[48, 58, 70, 71, 162] Corroborating earlier reports,[62, 163] we find retention within the injected skin to be size-dependent (Figure 4.3A), as is the relative selectivity of skin exposure to injected agent relative to systemic tissues (Figure 4.3B). When size matched, macromolecular and particulate retention in the skin is equivalent (Figure 4.3A), resulting in similar, although somewhat higher in the case of ~25-30 nm sized tracers, skin exposure (Figure 4.5C). Levels of dLN accumulation were higher for dextrans relative to polystyrene spheres at all tested sizes, save 5 nm dextran (Figure 4.4A). However, the specificity of dLN accumulation relative to systemic tissues was highest for an intermediate-sized (30 nm) dextran and at 72 hr p.i. for the largest (500 nm) polystyrene sphere tested (Figure 4.4C), presumably due to these tracers exhibiting the most robust levels of lymphatic uptake[101] versus high level of retention

within (Figure 4.3A) and restriction to (Figure 4.3B) the skin as well as dependency of the 500 nm tracer on cell-mediated transport to dLN (Figure 4.4B). Furthermore, macromolecular tracers accumulated in dLN at levels roughly ten times that of size-matched polystyrene spheres (Figure 4.5B-D). Therefore, the interplay among hydrodynamic size and flexible, chain-like macromolecular versus rigid, spherical particulate form control the exposure at the site of skin injection versus simultaneous capacity to deliver payload to dLN, respectively. As previous studies[48, 144] have demonstrated that the extent of LN delivery influences immunotherapeutic outcomes,[48, 144] we show herein the importance of considering the coupled effects of both the size and form/flexibility of biomaterial carriers to potentially increase therapeutic efficacy in vaccine or immunotherapy applications.

Since after cellular uptake, drug carriers and their payload are presumably restricted to within migrating cells,[164] the mechanism of lymphatic-mediated delivery to dLN influences the signaling capacity of and the availability of intra- versus extracellular drug targets in migrating versus LN-resident cells to delivered payload.[92] Our results suggest that since dextran tracer concentrations in the dLN did not increase from 24 to 72 hr p.i. (Figure 4.4A, B), macromolecular transport from the skin to the dLN is primarily mediated via passive lymphatic drainage and is thus largely extracellularly available. Despite much lower total levels of dLN accumulation relative to tested dextrans, the same likely also holds for 25 nm polystyrene spheres (Figure 4.4B). However, the 50 and 500 nm polystyrene tracers exhibited an increase of approximately 5- and 40-fold, respectively, by 72 hr p.i. (Figure 4.4B), and are thus, in part, restricted within dLN to the cells that migrated there from the periphery. These results corroborate

previous work demonstrating that accumulation of large (500 and 1000 nm) particles within dLN is cell-mediated and absent in dendritic cell-depleted mice[92] or in mice lacking dermal lymphatics,[71, 165] whereas smaller (20 nm) particles are still able to drain in dendritic cell-depleted mice and be taken up by a variety of dLN-resident cells.[92] Together, these results demonstrate that both the size and form of biomaterial drug carriers may impact levels and intra- versus extracellular locality of payload within dLN.

Our results demonstrate the unexplored importance of carrier form for dermal and LN targeting applications as we noted a divergence between the size-dependency of macromolecule and rigid particle profiles of bioavailability within the skin and dLN. Most noteworthy, over 2% of the injected 30 nm dextran accumulated within the dLN, while dLN accumulation was only 0.2% of the injected amount for similarly sized 25 nm polystyrene spheres. We hypothesize these differences manifest as a result of the increased flexibility of chain-like macromolecular dextrans relative to that of rigid polystyrene spheres,[166-168] as differences in flexibility have been shown to influence both diffusion within skin[169] and lymphatic uptake.[101] How biomaterial rigidity and deformability influence the distribution of drug carriers throughout dLN as well as resulting profiles of resident cell uptake has yet to be fully elaborated. Also, whether particles with lower rigidities, such as those comprised of engineered biomaterials[170] rather than polystyrene, or particles with non-spherical shapes, such as rods or discs[171, 172], exhibit size-dependent biodistribution profiles more similar to macromolecules or polystyrene spheres remains to be determined. Lastly, whereas the primary focus of this work was to elucidate the influence of hydrodynamic size and form on skin retention and

dLN accumulation, the coupled effects of numerous other characteristics of engineered biomaterial-based drug carriers (charge, shape, lipophilicity, matrix affinity, etc.) likely play a significant role as well and have yet to be systematically analyzed for dermal retention and dLN accumulation.

#### **4.5 Conclusion**

In summary, our results demonstrate that macromolecule and particle retention within the skin as well as accumulation and enrichment in dLN relative to systemic tissues is acutely influenced by hydrodynamic size but in different respects. The maximization of immunotherapeutic drug therapeutic efficacy within the skin and/or dLN as well as simultaneous limiting off-target effects may thus be tailored by changing the size and/or form of engineered biomaterial-based carriers. These results will inform the rational design of drug targeting and delivery strategies to achieve locoregional immunomodulation.

## **CHAPTER 5. VEGF-A and -C-induced Disease Progression Effects on Size-Regulated Profiles of Tumor-derived Molecular Association with Immune Cells within Locoregional Lymph Nodes Versus Systemic Tissues**

### **5.1 Introduction**

While early stage melanoma can be treated through surgery, advanced stage disease, which usually presents with tumor-induced immune suppression and metastasis, results in poor patient prognosis given our currently limited knowledge of treating the disseminated effects of cancer. Cancer immunotherapy is emerging as a successful treatment approach that induces durable objective responses in patients with advanced melanoma, yet these responses are achieved in only a quarter to a third of patients [173, 174]. As tumor immune suppression involves multiple signaling pathways and several immune cell subtypes, including T cells, B cells, dendritic cells, and macrophages [175], it is difficult to target all the disseminated effects even with combination therapy [176], indicating a need for better understanding the pathways of crosstalk involved in cancer signaling to prevent disease progression.

A compounding factor in tumor immune suppression is that the effects are not limited to the primary tumor microenvironment. By virtue of lymphatic drainage mechanisms, pathways of tumor immune suppression have the potential to be active in both the tumor microenvironment as well as sentinel lymph nodes. These draining lymph nodes (dLN) are continuously receiving incoming extracellular vesicles, endogenous signaling molecules, and antigens, which are thought to be partitioned primarily by molecular weight within the healthy lymph node by either entering the conduit system [16, 17] or passing through the subcapsular sinus barrier [16, 177] after which they may

mediate signaling with resident lymphocytes in deeper areas of the lymph node. Alternatively, larger soluble molecules may be transported by flow around the lymph node sinuses, through downstream lymphatics, and into venous blood circulation. While the return of excess fluid is necessary to maintain tissue fluid balance and homeostasis, there is also the opportunity for the eventual dissemination of lymph-borne molecules to systemic tissues such as the spleen, lungs, liver, and kidneys. Moreover, the presence of tumor-derived factors have been observed in patient sera, including a variety of proteases, growth factors, and immunosuppressive cytokines [42, 178], which indicate the potential for tumor-secreted molecules to influence immune cell functions [11] and pre-metastatic niche development [37, 46] within disseminated tissues.

We have previously demonstrated that tumor progression modulates the size-dependent tissue-level distribution of tumor-derived factors [62]; however, the specific influence of tumor blood and lymphatic vascular remodeling on the capacity of tumor-secreted soluble factors (TSF - e.g. proteins, exosomes, and microvesicles) active in the regulation of immune signaling to distribute amongst subpopulations of systemic tissue-resident immune cells versus dLN-resident cells that exhibit distinct lymph node substructural distributions as well as immunological functions remains unexplored. We therefore sought to evaluate the effects of tumor vascular remodeling, including those resulting from tumor VEGF-C overexpression (OE) and VEGF receptor-2 inhibition, on exposure of sentinel lymph node-resident as well as systemic tissue-resident phagocytic and immune cell subpopulations to factors derived from the tumor microenvironment. To accomplish this goal, we examined the *in vivo* biodistribution and uptake by immune cell subtypes of a panel of fluorescently labeled macromolecular and particulate tracers size-

matched to physiological biomolecules ranging from 10-500 nm in hydrodynamic diameter after intradermal or intratumoral infusion in C57Bl6 mice in a temporal- and tissue-resolved fashion. Our results indicate that both VEGF-C OE and VEGFR-2 inhibition partially restore molecular transport to dLN while reducing systemic tissue accumulation of species >30 nm. Furthermore, tumor-induced changes in dendritic cell and macrophage organization may underlie the altered accumulation of 30 and 10 nm TSF within tumor-dLN that resulted in decreased TSF exposure to barrier, migratory, and dendritic cells, but not to T and B cells in tumor-dLN. Our findings have important implications in the role of tumor blood and lymphatic remodeling in the immunological crosstalk between tumors, their draining lymph nodes, and systemic tissues that may be targets for metastasis as well as in the development of drug delivery strategies to mitigate the deleterious disseminated effects of advanced cancers.

## **5.2 Materials and Methods**

### *5.2.1 Animal Tumor Models and Inhibitor Treatment*

C57Bl6 mice were purchased at 6 weeks of age from The Jackson Laboratory (Bar Harbor, Maine, USA). All protocols were approved by the Institutional Animal Care and Use Committee. For cohorts termed WT and VC,  $0.5 \times 10^6$  B16F10 or B16F10-VC murine melanoma cells were intradermally implanted into the left dorsal skin of 6-8 weeks old mice on day 0, respectively. For cohorts termed R2, from day 2 post B16F10 tumor implantation until endpoint, vandetanib at 50 mg/kg in 1% Tween 80 (Sigma-Aldrich, St. Louis, MO, USA) or vehicle alone was administered daily by oral gavage using a 22 gauge reusable small animal feeding needle (Cadence Science, Staunton, VA,

USA). Tumor dimensions were measured with calipers and reported as an ellipsoidal volume.

### *5.2.2 ELISA Measurements of Tissue VEGF-A and VEGF-C*

Tumor and skin tissues were dissected directly into Dulbecco's phosphate-buffered saline (D-PBS) (VWR International Inc, West Chester, PA, USA) containing tubes and homogenized with 1.4 mm acid washed zirconium grinding beads (OPS Diagnostics LLC., Lebanon, NJ, USA) using a FastPrep-24 Automated Homogenizer (MP Biomedicals, Santa Ana, CA, USA). Homogenized samples were stored at -80°C until analyses. 1:10 dilutions of thoroughly mixed tissue homogenates in reagent buffer were measured for VEGF-A and VEGF-C by ELISA (R&D Systems Inc., Minneapolis, MN, USA) per the manufacturer's protocol.

### *5.2.3 Micro-computed Tomography Imaging for Vascular Measurements*

Animals were perfused with saline followed by neutral buffered formalin (Thermo Fisher Scientific) for 10 minutes, then with saline to rinse, and lastly MicroFil (Flow Tech Inc., Carver, MA) catalyzed at a viscosity appropriate for small vessels (5 mL lead-based contrast agent: 2.5 mL diluent: 0.25 mL curing agent). Afterwards, perfused mice were carefully stored at 4°C overnight to cure the contrast agent. The following day, skin or tumor samples were harvested and stored in D-PBS. Micro-computed tomographic imaging was accomplished using a SCANCO Medical  $\mu$ CT50 (SCANCO USA, Inc., Wayne, PA, USA).  $\mu$ CT image slices were constrained using manual selection of the sample outline and processed with a Gaussian filter at a consistent global threshold via the SCANCO Medical  $\mu$ CT Evaluation Program before 3-dimensional reconstruction [99].

#### 5.2.4 *Fluorescent Tracers*

500 nm yellow-green and red fluorescent (505/515 and 580/605 excitation/emission, respectively) carboxylate-modified microspheres were purchased from Thermo Fisher Scientific Inc. 40,000 Da (Dalton) Tetramethylrhodamine isothiocyanate (TRITC) dextran was purchased from Sigma-Aldrich. 500,000 Da amino-dextran (Thermo Fisher Scientific Inc.) was covalently labeled by incubation with Alexa Fluor 647- or 700-NHS-Ester dyes (Thermo Fisher Scientific Inc.) in 0.1 M NaHCO<sub>3</sub> at pH 8.4 for 4 hours on a tube rocker. AF647 and AF700 dextran-dye conjugates were purified from unreacted free dye by Sepharose CL-6B gravity column chromatography after conjugation. Purified dextran-fluorophore conjugates were further confirmed free of unconjugated dye by a second Sepharose CL-6B column analysis [62]. All reagents were used and maintained under sterile conditions. Hydrodynamic sizes were confirmed pre-injection by dynamic light scattering using a Zetasizer Nano ZS (Malvern Instruments, Ltd., Malvern, U.K.).

#### 5.2.5 *Tracer Injections*

Fluorescent tracers suspended in saline were co-infused by syringe pump at a rate of ~300 nL per second directly into the center of tumors (groups WT, VC, and R2) using a 27 gauge needle while mice were under anesthesia via isoflurane. Alternatively, tracers were infused into the dermal layer of the skin of naïve mice (group termed N). For biodistribution experiments 500 nm red or yellow-green fluorescent microspheres (19 pM), 30 nm AF700 or AF647 dextran (4.8 μM), and 10 nm TRITC dextran (4.8 μM) were co-infused in 10 μl of saline total. Mice were euthanized via CO<sub>2</sub> asphyxiation at the prescribed times post tracer injection for each experiment.

### 5.2.6 *Tracer Biodistribution Analyses*

At 4, 24, and 72 hr post tracer injection, mice were sacrificed and the tumor or skin injection site, tumor-draining axillary and brachial lymph nodes, spleen, lungs, liver, and kidneys were harvested and homogenized in D-PBS using 1.4 mm acid washed zirconium grinding beads with a FastPrep-24 Automated Homogenizer. Whole tissue homogenate fluorescence was measured with a Synergy H4 BioTek plate reader (BioTek Instruments Inc, Winooski, VT, USA), compensation was applied, and fluorescent tracer amounts and concentrations were calculated from standard curves made by spiking individual naïve tissue homogenates with tracer solution.

### 5.2.7 *Tumor and Lymph Node Immunohistochemistry and Imaging*

Tumor, skin, and draining lymph nodes were frozen in optimum cutting temperature compound (Sakura Finetek USA, Inc., Torrance, CA, USA) in 2-methylbutane (Sigma-Aldrich) chilled by liquid nitrogen and frozen tissue blocks were immediately stored at -20°C. For imaging of tracer draining lymph nodes, coverslips were mounted onto lymph node tissue slices (10 µm thickness) using Vectashield mounting medium (Vector Laboratories, Burlingame, CA, USA) with no prior wash steps and within 30 minutes of imaging. Otherwise, lymph node, skin, and tumor tissue sections were fixed with pre-chilled acetone for 10 minutes at 4°C and subjected to standard immunofluorescence protocols using the following antibodies, which were obtained from Thermo Fisher Inc unless otherwise specified: FITC conjugated rat anti-mouse CD31 (1:50), rabbit anti-mouse Lyve-1 (1:250), Alexa Fluor 633 goat anti-rabbit (1:300), Armenian hamster anti-mouse CD3e (1:50), Alexa Fluor 647 goat anti-hamster (1:300, Abcam plc., Cambridge, MA, USA), Alexa Fluor 488 conjugated rat anti-mouse

CD169 (1:100, BioLegend Inc, San Diego, CA, USA), biotinylated rat anti-mouse F4/80 (1:200, Life Technologies), streptavidin-Alexa Fluor 555 (1:400, Life Technologies), biotinylated rat anti-mouse B220 (1:250), and Alexa Fluor 488 conjugated Armenian hamster anti-mouse CD11c (1:50, BioLegend Inc). Blocking and antibody dilutions were performed with 10% donkey serum (Sigma-Aldrich) in D-PBS. Slides were washed with 0.1% Tween 20 (Sigma-Aldrich) in D-PBS for washing steps, counter stained with DAPI (VWR International Inc), and imaged using a 710 NLO confocal microscope (Carl Zeiss Microscopy Ltd, Jena, Germany) with a 20x magnification objective.

#### *5.2.8 Tracer Flow Cytometry Analyses*

Axillary and brachial draining lymph nodes were pooled and incubated with 1 mg/ml Collagenase D (Sigma-Aldrich) in D-PBS with calcium and magnesium for 1 hr at 37°C, passed through a 70 micron cell strainer (Greiner Bio-One, Monroe, NC, USA), washed, and resuspended in a 96 well plate (VWR International Inc) for staining. Lung tissues were treated with the same procedure as lymph nodes. Spleen capsules were disrupted using needles and the cell suspension was passed through a 70 micron cell strainer, pelleted then incubated with red blood cell lysis buffer (Sigma-Aldrich) for 5 minutes at room temperature, diluted with D-PBS, washed, and resuspended. Liver tissues were disrupted with needles then passed through a 70 micron cell strainer, centrifuged at 60xg for 1 minute to remove large debris and the supernatant was collected into a different tube and centrifuged at 300xg for 5 minutes. The pellet was resuspended, layered onto lymphocyte separation medium (Thermo Fisher Scientific Inc), and centrifuged for 20 minutes at 400xg. The mononuclear cell layer was recovered, incubated with red blood cell lysis buffer as before, washed, and resuspended for

staining. All antibodies for flow cytometry were from BioLegend, Inc. unless otherwise stated. Cells were blocked with 2.4G2 (Tonbo Biosciences, San Diego, CA, USA) for 15 minutes on ice, washed, then stained with a fixable viability dye eFluor 455UV (1:1000, eBioscience, San Diego, CA, USA) for 15 minutes on ice before quenching with 0.1% bovine serum albumin in D-PBS (flow cytometry buffer). Antibodies were prepared in flow cytometry buffer at the following dilutions based upon preliminary titrations: PerCP anti-mouse CD45 (0.5:100), PE-Cy7 anti-mouse CD11b (0.625:100), BV421 anti-mouse CD11c (5:100), BV605 anti-mouse CD169 (5:100), BV650 anti-mouse B220 (2:100), BV711 anti-mouse CD3 (1.25:100), BV785 anti-mouse F4/80 (2.5:100). Cells were fixed with 4% paraformaldehyde (VWR International Inc) and kept at 4°C until analyzed with a customized BD LSRFortessa flow cytometer (BD Biosciences, Franklin Lakes, NJ, USA). Compensation was performed with AbC compensation beads (Thermo Fisher Scientific Inc) and data was analyzed using FlowJo software v10 (FlowJo, LLC, Ashland, OR).

#### *5.2.9 Tracer Diffusion Analyses*

Capillary tubes were loaded with 5.6 mg/ml rat tail collagen type I solution (Corning Inc., Corning, New York, USA) in D-PBS and allowed to gel overnight at 37°C. 500 nm yellow green spheres, FITC conjugated 30 nm dextran, and TRITC 10 nm dextran were loaded in separate tubes and fluorescence imaging was performed every 4 minutes for 2 hours at 37°C with a Zeiss AxioObserver Z1 inverted microscope (Carl Zeiss) with a 4x magnification objective. Image analysis was performed using ImageJ software.

#### *5.2.10 Statistical Analysis*

Data are represented as the mean accompanied by S.E.M. and statistics were calculated using Prism 6 software (GraphPad Software, Inc., La Jolla, CA, USA). Statistical significance was defined as  $p < 0.05$  following two-way ANOVA and post-hoc analysis with Tukey tests or one-way ANOVA followed by Fisher's Least Significant Difference (LSD) test. One, two, and three symbols denoting statistical significance represent  $p < 0.05$ , 0.01, and 0.001 respectively, unless otherwise specified. Area under the curve (AUC) was calculated using the built-in Prism analysis tool.

### **5.3 Results**

#### *5.3.1 Endogenous and Induced or Suppressed Angiogenic and Lymphangiogenic Signaling During Melanoma Progression*

The dynamic changes within the blood and lymphatic vasculature of B16F10 melanomas developing in the dorsolateral dermis of immune-competent C57Bl6 mice (Figure 5.1A) were assessed. First, VEGF-A concentrations within developing wildtype, untreated B16F10 melanomas (WT) were found to be increased with tumor growth (Figure 5.1B), changes that were reflected in a dramatic increase in tumor vascularity (Figure 5.1C, D). Conversely, VEGF-C concentrations within melanomas decreased with tumor growth (Figure 5.1B) and were accompanied by decreased lymphatic vessel densities (Figure 5.1B, bottom).

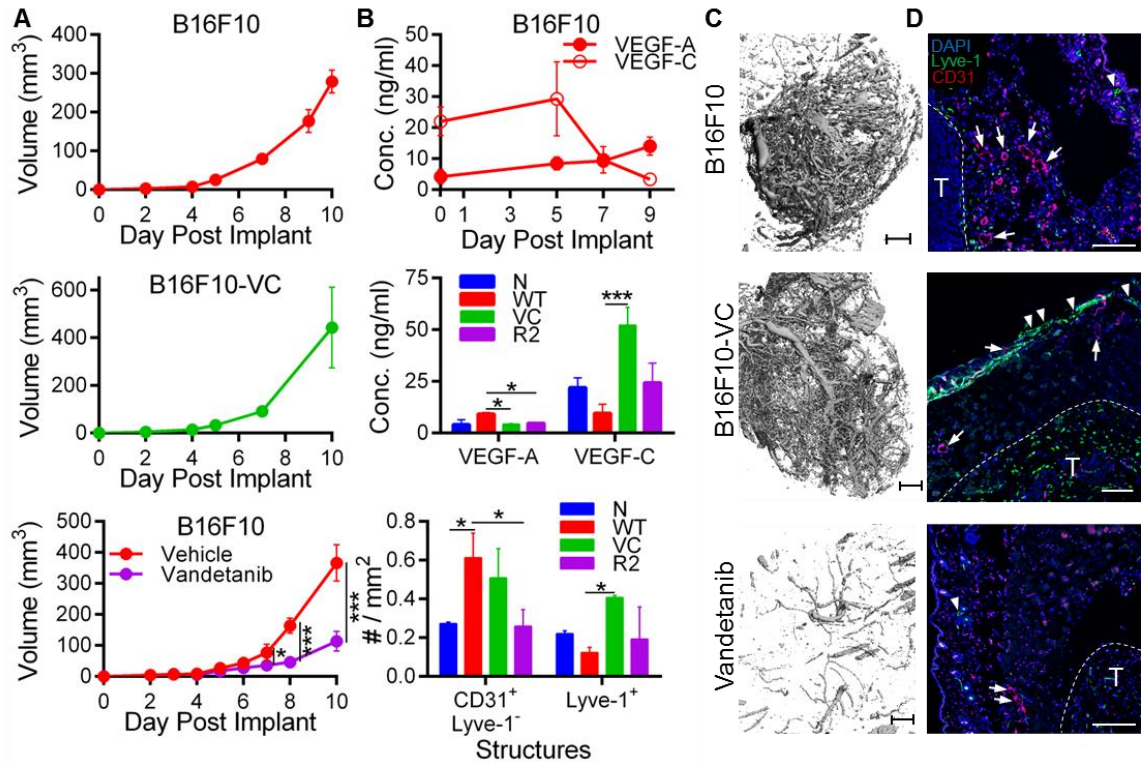


**Figure 5.1** Characterization of tumor models. B16F10 (A, top), B16F10-VC (A, middle), and vandetanib treated B16F10 melanoma tumor growth curves (A, bottom). Tissue VEGF-A and VEGF-C concentrations of B16F10 tumors over the course of tumor progression (B, top), comparison to B16F10-VC and vandetanib treated tumors at Day 7 post implant (B, middle), and blood and lymphatic vessel densities quantified from immunohistochemistry (B, bottom). 3D reconstructions of micro-computed tomography of the tumor blood vasculature at Day 7 post implantation for B16F10 (C, top), B16F10-VC (C, middle), and vandetanib treated B16F10 (C, bottom); scale bars = 1 mm. Representative immunohistochemistry images for tumor slices with arrows denoting blood vessel structures and arrowheads for lymphatic vessel structures; scale bars = 200 microns (D). \* indicates significance by multiple t-tests. (A) n =4-12; (B-D) n = 3-5 mice per group.

To mitigate the effects of endogenous vascular remodeling that accompany tumor growth and progression, two models of experimentally induced alterations in tumor vascular remodeling were established and characterized: B16F10 melanomas overexpressing VEGF-C (VC) (Figure 5.2A) and wildtype B16F10 melanomas grown in mice treated with a VEGFR-2 inhibitor vandetanib (R2). Rates of tumor growth were

similar between WT and VC tumor models, whereas R2 tumors resulted in significantly reduced tumor volumes from days 7-10 post implantation in comparison to vehicle control treated tumors (Figure 5.1A). As a result of VEGF-C o/e, VEGF-C levels in VC tumors were significantly elevated, ~five-fold (Figure 5.1B), and increased the peritumoral lymphatic density (Figure 5.1D). R2 tumors exhibited significantly reduced intratumoral VEGF-A levels, ~50% compared to WT melanomas (Figure 5.1B), an effect reflected in the dramatically reduced level of R2 tumor vascularity (Figure 5.1C, D). Both VC and R2 tumors, respectively, exhibited normalized (on par with naïve skin, Figure 5.2B) VEGF-A concentrations and vascular densities versus VEGF-C concentrations and lymphatic densities (Figure 1B-D).

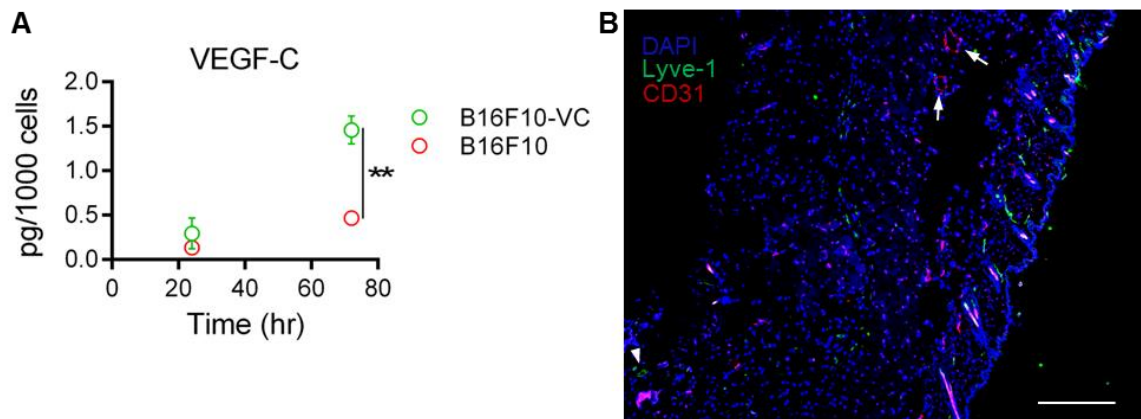


**Figure 5.2 VEGF-C Overexpression in Culture and Skin Section IHC.** VEGF-C measurements for B16F10-VC compared to B16F10 in culture per 1,000 cells plated (A). \*\* indicates  $p < 0.01$  by two-way ANOVA and post-hoc Tukey's test;  $n = 2$ . IHC image of naïve skin section; scale bar = 250 microns (B).

### 5.3.2 Clearance from Tumors is Increased with VEGF-C Overexpression and VEGFR-2 Inhibition

In order to evaluate the effects of tumor growth and experimentally induced alterations in (lymph)angiogenic signaling and remodeling on tumor-derived soluble

factor clearance from the tumor microenvironment, B16F10 tumors were implanted and mice received an intratumoral co-infusion of 500, 30, and 10 nm fluorescent tracers upon reaching day seven post tumor implantation, and were sacrificed at 4, 24, or 72 hours post-tracer injection (Figure 5.3A). 500 nm polystyrene spheres rely on cell-mediated transport as they are too large to be removed from the tissue interstitium site of injection by fluid transport alone due to extracellular matrix constraints [162]. 500 nm tracer distribution levels were thus used to evaluate the impact of endogenous and induced or suppressed angiogenic and lymphangiogenic signaling during melanoma progression on cell-mediated transport from the tumor. We next utilized dLN cellular association with 30 and 10 nm tracers to assess soluble lymphatic transport of tumor-derived molecules under the effects of altered angiogenic and lymphangiogenic signaling during melanoma progression.

As previously reported [62, 163, 179], retention within the skin site of injection is acutely size-dependent (Figure 5.3B) and is slowed by WT tumor growth (Figure 5.3C). 30 and 10 nm tracers were retained at reduced levels in VC and R2 tumors (Figure 5.3C). 500 nm tracer retention in R2 but not VC tumors was also restored to levels seen in N tissues (Figure 5.3C). These results suggest VEGF-A- and -C-dependent effects on tumor vascular remodeling result in the stagnant profiles of tissue clearance observed in WT tumors.

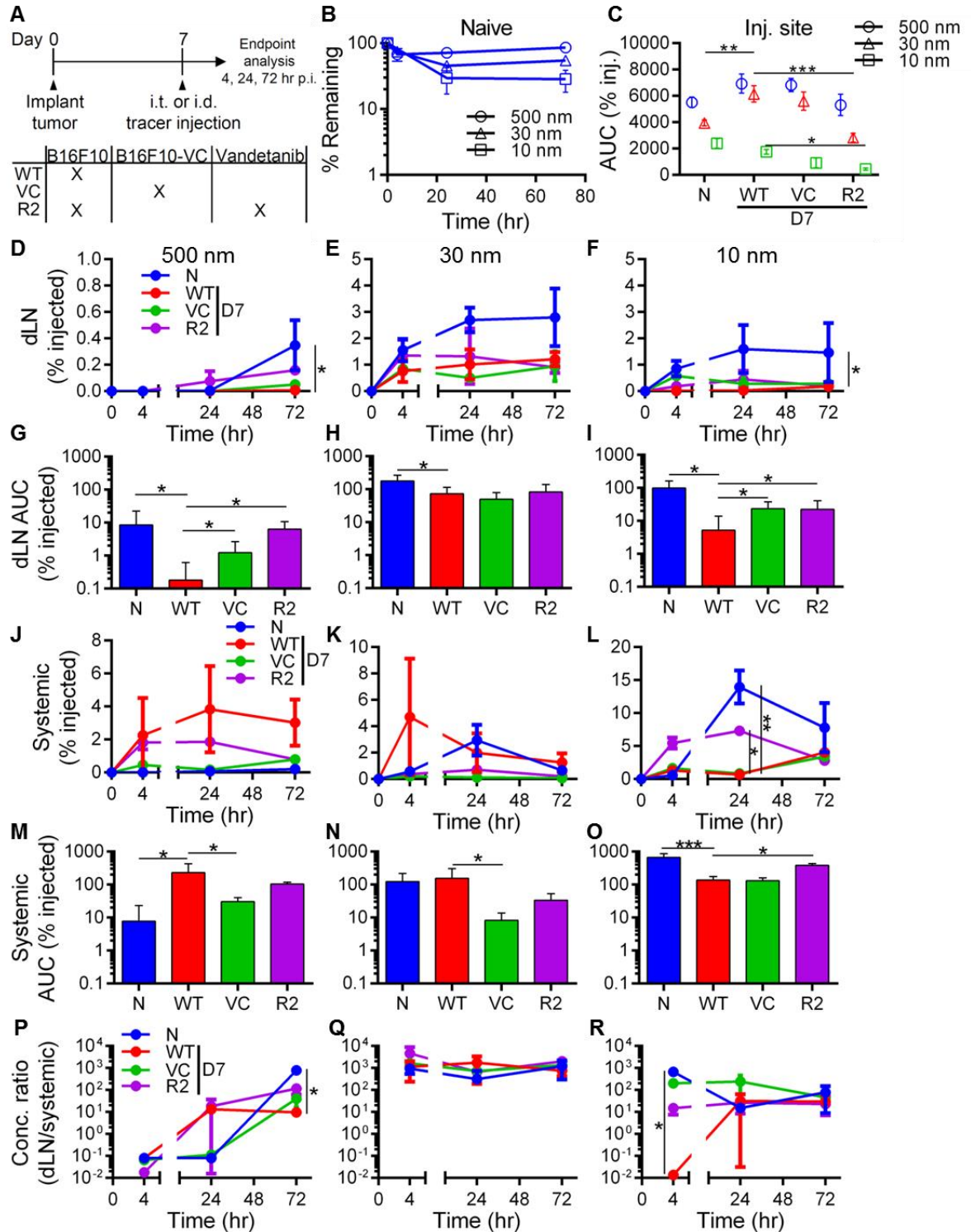


**Figure 5.3 VC and R2 Partially Recover 500 and 10 nm LN Drainage, while VC Prevents Enhanced 500 and 30 nm Tracer Systemic Dissemination. Timeline and group descriptions for tumor implantations with endpoint analyses at 4, 24, and 72 hr post intratumoral tracer injections (A). Percent of injected tracer remaining at**

**the dermal injection site in naïve (non-tumor implanted) mice representing size-dependent tracer clearance in healthy animals (B). Tracer exposure within the skin or intratumoral site of injection expressed as AUC of the 0-72 hours post-injection time series (C). Time-resolved tracer accumulation within dLN (D-F) and total exposure from 0-72 hrs (G-I). Systemic tissue tracer levels combined for spleen, lungs, liver, and kidneys (J-L) and associated total exposure from 0-72 hrs (M-O). Ratio of accumulating tracer concentrations within dLN vs systemic tissues (P-R). (D-F; J-L; M-O) \* indicates significance by one-way ANOVA; (G-I; M-O) \* indicates significance by multiple t-tests; n = 4-9 mice per group.**

### *5.3.3 VEGFR-2 Inhibition Partially Recovers 500 and 10 nm Tracer dLN Accumulation, while VEGF-C Overexpression Results in Reduced Systemic Tissue Exposure to 500 and 30 nm Tracers*

We next investigated the effects of altered (lymph)angiogenic signaling in the dissemination of tumor-derived molecules by measuring extratumoral tracer accumulation within the local dLN versus systemic tissues (spleen, lung, liver, and kidneys) in tumor-bearing mice. After injection, 500 and 10 nm tracers exhibited a significant reduction in accumulation profiles within dLN at 72 hours p.i. as compared to injections in the dermis of naïve mice, but for the 30 nm tracer only a modest reduction in dLN accumulation was observed at each measured time point (Figure 5.3D-F). VC and R2 tumors also demonstrated increased 500 nm exposure within dLN relative to WT tumor levels, approaching that of naïve animals (Figure 5.3G). This trend for increased dLN exposure for the VC and R2 groups over the WT melanomas was similarly observed for the 10 nm, but not for the 30 nm, tracer (Figure 5.3H-I). When examining systemic biodistribution profiles, 500 and 30 nm tracer accumulation within systemic tissues was increased for WT over naïve injected tissues as we have previously reported [62, 179], whereas, conversely, systemic accumulation of 10 nm tracer was significantly greater for naïve and R2 groups than WT tumors at 24 hours p.i. (Figure 5.3J-L). When considering 500 nm tracer exposure in systemic tissues, VC but not R2 tumors exhibited profiles

significantly diminished relative to WT tumors and more similar to that of N tissues (Figure 5.3M). Exposure of 30 nm tracer in systemic tissues on the other hand was reduced in VC tumors relative to WT tumors, which was unchanged relative to N tissues (Figure 5.3N). Conversely, systemic exposure to 10 nm dextran exposure was reduced in WT tumors relative to N tissues, an effect reversed in R2 but not VC tumors (Figure 5.3O). As a result of these altered profiles of dissemination and when considering the volume of the tissue in which the tracers are distributed to determine an average tissue concentration, all tested tumor types reduced the relative enrichment of 500 and 10 nm tracer exposure within dLN relative to systemic tissues at late (72 hr) versus early (4 hr) times post injection (p.i.), respectively (Figure 5.3P,R). 30 nm tracer on the other hand exhibited high levels of dLN enrichment relative to systemic tissues irrespective of time p.i. (Figure 5.3Q). These results indicate partially recovered lymphatic drainage and a reduction in systemic tissue over-exposure to tumor-derived factors resulting from tumor growth and experimentally induced alterations in tumor (lymph)angiogenic signaling.

#### *5.3.4 Hydrodynamic Size- and Tumor (Lymph)angiogenic Signaling-dependent Profiles of Tracer Association with Discrete Immune Cell Subpopulations within dLN*

Flow cytometry analysis confirmed detection of the 500 nm tracers primarily in CD11c, F4/80, and, to a lesser extent, B220 positive subsets (Figure 5.4A-B). When comparing between the N tissues to all tested tumor types, no significant differences in the frequency of 500 nm+ cells within cellular populations were observed (Figure 5.4B), yet higher total counts of 500 nm+ cells in VC dLN were measured (Figure 5.4C). This trend in accumulation within B220 positive cells - likely either B cells or plasmacytoid DCs - could be the result of an increased transfer of 500 nm tracer from migratory CD11c+ to dLN resident B220+ populations (Figure 5.4C).

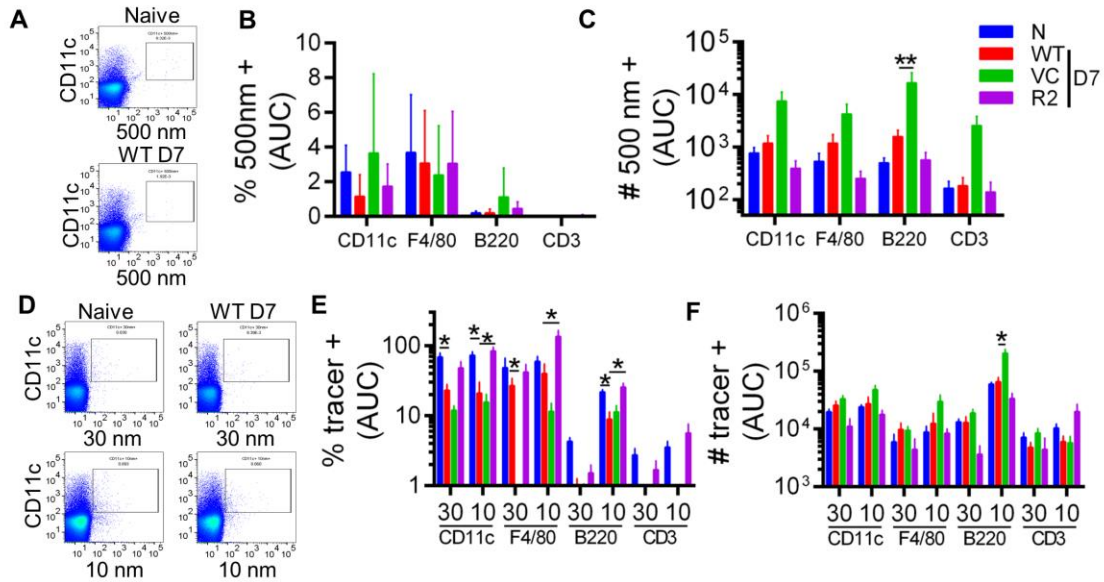


**Figure 5.4 Enhanced Cellular Tracer Exposure within VC and R2 dLN. Example flow cytometry gating of 500 nm tracers in N and WT dLN (A). Cell-mediated transport directs 500 nm tracer exposure calculated as AUC from 0-72 hr from the percent of each marker positive subpopulation (B) and from total cell counts (C). Lymph-soluble 30 and 10 nm tracer flow cytometry gating (D) and juxtaposition of exposure calculated similarly as percent of each marker positive subpopulation (E) and from total cell counts (F). \* indicates significance by one-way ANOVA; n = 4-6 mice per group.**

Uptake of lymph-soluble tracers by dLN-resident cells was next analyzed by flow cytometry (Figure 5.4D). Compared to naïve dLN, the frequency of 30 and 10 nm tracer positive CD11c+ and F4/80+ cells was reduced for WT dLN, an effect partially restored in R2 but not VC tumors (Figure 5.4E). Strikingly, in distinct contrast to 30 nm tracer that exhibited minimal to no association with B220+ and CD3+ cell populations, 10 nm tracer was taken up appreciably by both B220+ and CD3+ cells in N animals, levels that were reduced by WT tumors but restored in R2 tumors (Figure 5.4E). However, when considering the total number of tracer+ cells, many of the differences observed in the %+ analyses were not observed, yet the overall count of 10 nm+ B220+ cells in VC was greater than WT dLN potentially indicating the ability of small molecules to distribute

amongst a hyperplastic cellular population [18, 180] for increased exposure following lymphatic drainage (Figure 5.4F).

### *5.3.5 dLN Distributions of Tracers and Resident Cell Subpopulations are Influenced by Hydrodynamic Size-dependent Tumor Vascular Remodeling, Respectively*

Confocal imaging and analysis of tissue sections of tracer dLN demonstrated restriction of 30 nm dextran within the subcapsular sinus of N dLN while the 10 nm tracer penetrated deeper into the cortical areas and was more broadly distributed (Figure 5.5A). Contrastingly, 500 nm polystyrene spheres resulted in punctate, tracer positive areas within the paracortex of dLN at 72 hr, but not 4 hr, p.i. (Figure 5.5B). 500 nm tracers exhibited the farthest penetration at 72 hours p.i. while 10 nm tracers exhibited a moderate level of subcapsular infiltration at both time points (Figure 5.5A-B). The 30 nm tracers were restricted within close proximity to the capsule at 4 and 72 hr p.i. indicating accumulation within the subcapsular sinus and potentially dLN-resident barrier cells (Figure 5.5C). Immunohistochemistry images demonstrated cell subpopulation compartmentalization in the interior versus outer, capsule-adjacent regions of dLN of CD3<sup>+</sup> and CD11c<sup>+</sup> versus B220<sup>+</sup>, CD169<sup>+</sup>, and F4/80<sup>+</sup> cells, respectively (Figure 5.5C), which suggests that tracers with differing dLN distribution profiles likely accumulate within different resident cell subpopulations.

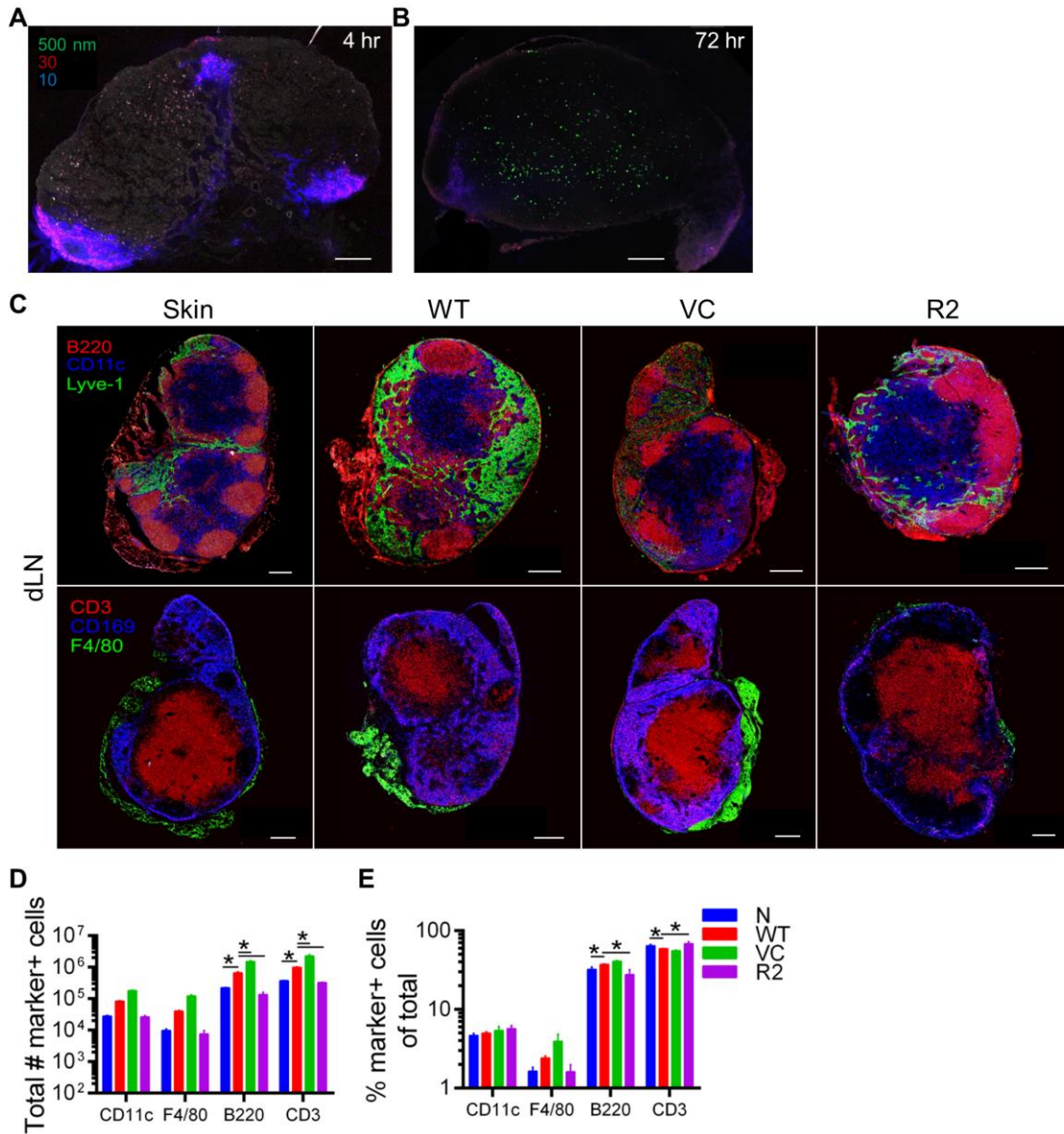


**Figure 5.5 Tracer Localization, Cellular Frequencies, and Organizational Remodeling within dLN.** Tracer drainage and localization within skin dLN at 4 (A) and 72 hr (B) p.i. in the naïve dermis. Total cell counts (D) and percentages for each marker subpopulation (E) within naïve and tumor-dLN. Scale bars = 200 microns; n = 4-6 sections from 2-3 separate LN per group (A-C); n = 4-6 mice per group (D-E).

We next characterized whether (lymph)angiogenic signaling influenced dLN cellular organization and frequencies. For WT versus N dLN, B220+ and Lyve-1+ zones were enlarged, CD169+ barrier cells (which includes subcapsular sinus macrophages and

medullary sinus macrophages) were greatly disorganized, CD169+ cells were no longer restricted to the dLN periphery, and we noted an overall reduction in F4/80+ areas (Figure 5.5C). For VEGF-C overexpressing tumor-dLN, B220+ areas were increased from WT dLN, with CD169+ maintaining their location near the subcapsular sinus similar to that observed in naïve dLN (Figure 5.5C). Upon imaging VEGFR-2 inhibited tumor-dLN, we found increased B220+ areas with irregular patterns of localization and reduced CD169+ and F4/80+ areas resembling WT dLN (Figure 5.5C). Total numbers of B220+ and CD3+ cells were elevated in WT relative to N tissues yet there was a reduction in CD3+ relative to B220+ frequency when quantified as a percent of the total dLN cells (Figure 5.5D, E). The total number of dLN B220+ and CD3+ cells were increased for VC, but reduced for R2 tissues as compared with WT (Figure 5.5D), yet only the R2 exhibited significant differences from WT dLN in B220+ and CD3+ percentages of total cells (Figure 5.5E).

#### *5.3.6 Overall Tissue Cellular Association with Tumor Progression Increased for 500 nm, Especially in Spleen Cells, but Decreased for 10 nm Tracers*

When analyzing the frequency of each cell subpopulation with detectable levels of associated tracer in assayed tissues, we found 500 nm tracers were primarily associated with CD11c and F4/80 populations within naïve dLN and spleen, 30 nm tracers were more prevalent in splenic cell populations, and 10 nm tracers were distributed amongst both spleen and lung immune cells (Figure 5.6A-C).

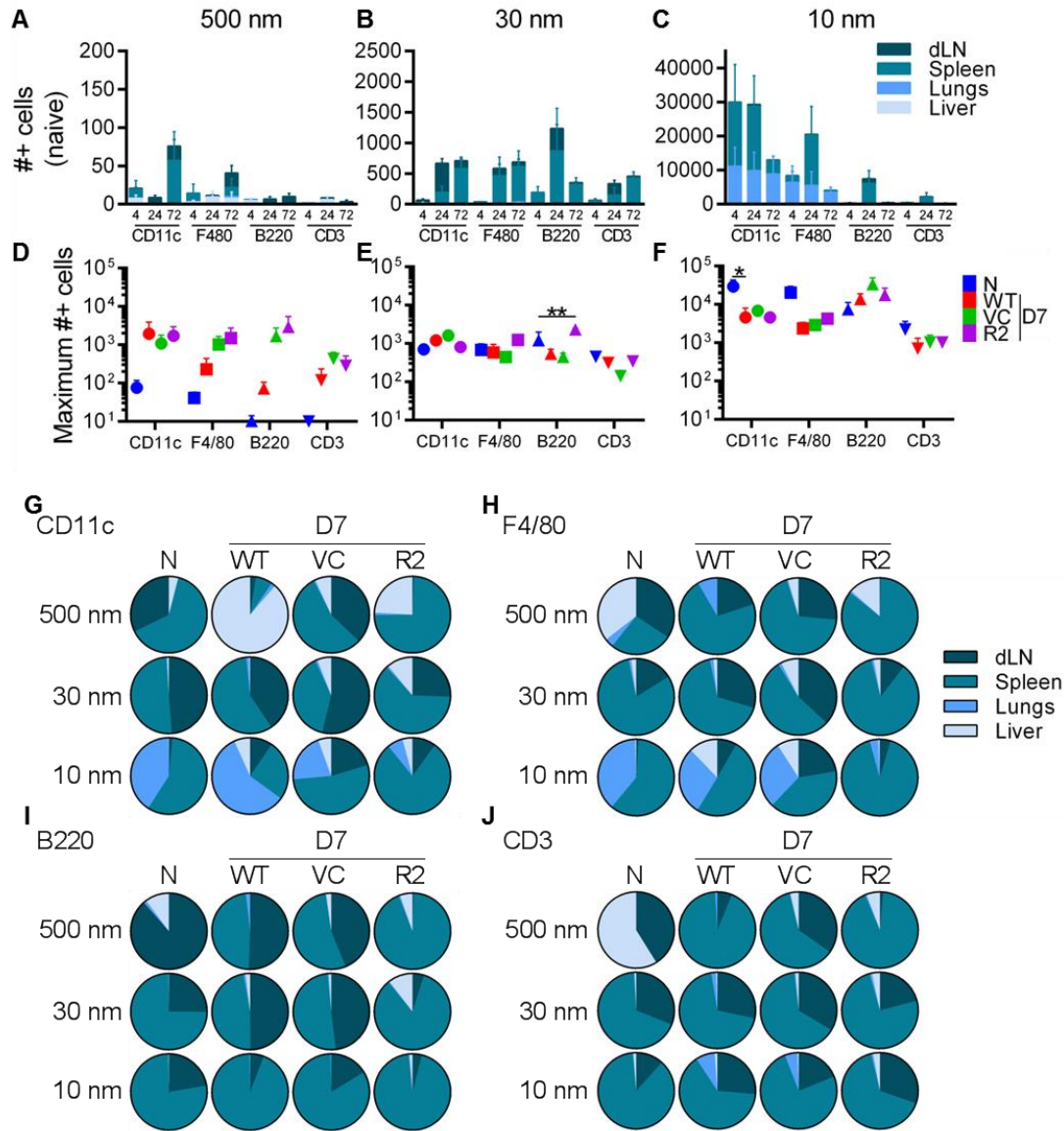


**Figure 5.6 Systemic Tracer Cellular Exposure.** Counts for tracer positive cells expressing CD11c, F4/80, B220, or CD3 in local dLN and systemic tissues including spleen, lungs, and liver (A-C). Summation of maximum number of tracer positive cell counts within all tissues at either 4, 24, or 72 hr post tracer injection (D-F). Proportional tracer exposure represented as AUC of tracer positive cell counts from 0-72 hr in disseminated tissues (G-J). \* indicates significance by two-way ANOVA with post-hoc Tukey's tests; n =4-6 mice per group.

However, upon examining the number of tracer positive cells and comparing the maxima among the tumor groups, trends suggest an increased amount (summed for all

tissues analyzed) of CD11c, F4/80, B220, and CD3 populations are associated with 500 nm tracers in WT, VC, and R2 animals (Figure 5.6D). The maximum number of 30 nm tracer positive cells in all tissues combined was relatively similar amongst all groups, with the exception that B220+ cellular exposure increased with VEGFR-2 inhibition (Figure 5.6E). 10 nm tracer maximum cell numbers were actually lower for WT as compared with naïve tissues for CD11c+ populations and trends suggest lower levels as well for organism-wide 10 nm positive F4/80+ and CD3+ cell counts (Figure 5.6F) which corroborates the previous tissue-level biodistribution data (Figure 5.3O).

Analyzing the relative extent of tracer exposure as AUC of tracer positive cell numbers per each tissue, the exposure for all cell subtypes was decreased for dLN and increased for systemic tissues for the 500 nm, but not 30 or 10 nm tracers in WT versus naïve groups (Figure 5.6G-J). Meanwhile, 500 nm exposure to F4/80+, B220+, and CD3+ cells in the liver of naïve mice shifts towards the spleen in WT mice, but this trend is reversed with CD11c+ cells in WT liver receiving more of the total 500 nm tracer exposure, and is only partially recovered with VEGFR-2 inhibition (Figure 5.6G-J). 30 nm exposure profiles remained relatively constant between naïve and WT groups, with only the B220+ population showing a shift in total exposure from the spleen to dLN for WT and VC groups versus N (Figure 5.6I), potentially due to greater numbers of B cells (Figure 5.5D). The lung and spleen received the majority of 10 nm tracer exposure in naïve mice, but increased dLN and liver exposure was observed for WT and VC groups (Figure 5.6G-H). Interestingly, VEGFR-2 inhibition seemed to skew CD11c+ and B220+ cell exposure towards the spleen for 500 nm tracer as compared to WT trends (Figure 5.6G-J).

*5.3.7 Altered 30 and 10 nm Tracer Exposure for Tumor-dLN Dendritic, Barrier, and Migratory Cellular Populations, but not B and T Cells, while 500 nm Exhibits Size-dependent Restriction of Diffusion by Cross-linked Collagen*

We further subdivided tracer association by cellular localization within dLN among paracortex cells (B cells (B), T cells (T), plasmacytoid dendritic cells (pDC), and conventional dendritic cells (cDC)), barrier cells (subcapsular sinus macrophages (SSM), medullary sinus macrophages (MSM), and medullary cord macrophages (MCM)), and migratory cells (dermal dendritic cells (dDC) and Langerhans' cells (LC)). 30 and 10 nm TSF exposure to pDC and cDC paracortex cells was reduced in WT versus N dLN, while 500 nm %<sup>+</sup> exposure profiles were relatively unaffected by malignant status (Figure 5.7A) confirming previous trends for the generalized marker<sup>+</sup> cells (Figure 5.4B, E). SSM and MCM barrier macrophages showed reduced association with 30 and 10 nm tracers, respectively, in WT dLN, which were only partially restored in R2 but not VC models (Figure 5.7B). We also observed that 30 and 10 nm exposure was reduced in WT dLN migratory cells and that LC, but not dDC exposure profiles were moderately recovered with R2 but not VC conditions (Figure 5.7C).

Soluble molecular transport within tissues, such as the tumor interstitium, may be hindered by the collagen matrix, thus altering TSF clearance and accumulation profiles independent of changes in vascular remodeling; hence, we measured TSF diffusion within collagen filled capillary tubes. All tubes were loaded evenly with tracer solutions at time zero (Figure 5.7D) and imaged every 4 minutes for 2 hours after which a size-dependent separation was notable (Figure 5.7E). Measurements of the fluorescence intensity profiles within the collagen gel areas showed that the 10 nm dextran exhibited the quickest diffusion into the gel followed by the slightly hindered 30 nm dextran, while

the 500 nm polystyrene spheres experienced greatly hindered diffusion (Figure 5.7F). Curve fitting of intensity profiles showed that the time constant for 10 nm tracer was on the order of 10 minutes while the 30 nm tracer's was approximately 60 minutes, both of which were significantly less than the ~6.5 hours calculated for the 500 nm tracer (Figure 5.7G). Interestingly, this profile mirrored the average accumulation profiles within paracortex-resident B and T cells in dLN (Figure 5.7A) indicating a potential role for diffusion in TSF uptake by these cell types.

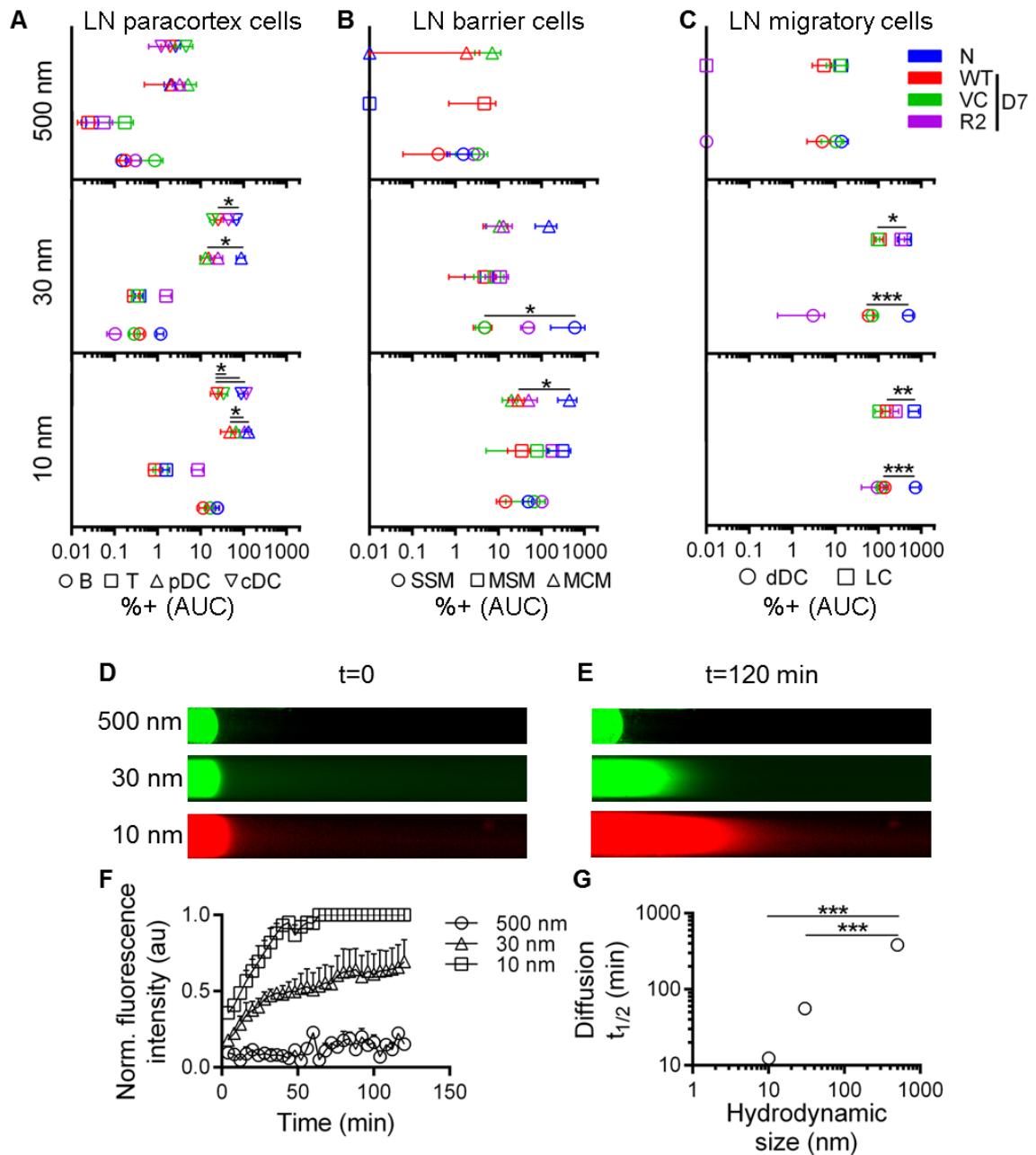


**Figure 5.7 Size-dependent Tracer Distribution Profiles Among Paracortex, Barrier, and Migratory Cells and Tracer Diffusion through Collagen.** Tracer exposure profiles within dLN were separated by location into paracortex (A), barrier (B), and migratory (C) cell groups. Fluorescent images of tracer diffusion in collagen filled capillary tubes at (D) time of individual tracer addition and (E) 120 minutes later. Normalized fluorescence intensity of diffusing tracer signal into the collagen gel (F). Diffusion time to half max derived from one phase non-linear fitting of diffusion profiles plotted against tracer hydrodynamic diameter (G). \* indicates significance

**by two-way ANOVA with post-hoc Tukey's tests. n = 4-6 mice per group (A-C); n = 3 experiments per group (D-G).**

#### **5.4 Discussion**

Tracer biodistributions amongst immune cell subtypes reveal unexpected effects of altered angiogenic and lymphangiogenic signaling. VEGFR-2 inhibition was expected to normalize blood vessels and, therefore, tracer exposure to systemic tissues. While we observed systemic exposure profile AUCs return to near naïve levels for the 10 nm tracer (Figure 5.3O), VEGFR-2 inhibitor treatment also resulted in partially normalized 500 and 10 nm dLN accumulation as compared to WT animals (Figure 5.3G, I) which may be attributed to normalized intratumoral fluid pressure [65, 101] and/or a partial reduction of tumor blood vessel pore sizes [66] creating opportunity for enhanced lymphatic transport. Contrarily, VEGF-C OE was expected to maximally influence 30 nm tracer profiles in dLN as this is the primary lymphatic draining molecule of the tracer panel [179]. However, we saw no significant change between WT and VC groups in 30 nm tracer exposure to dLN (Figure 5.3H), yet VEGF-C OE increased dLN AUC levels significantly for the 500 and 10 nm tracers in VC versus WT dLN (Figure 5.3G, I) indicating the potential for tumor lymphangiogenic remodeling to exert a greater effect on migratory cell populations or the transport of lymph-soluble 10 nm tracer, rather than larger 30 nm species. Combined, these findings demonstrate that inhibiting tumor angiogenic remodeling can impact TSF cell-mediated and soluble-lymphatic drainage of TSF, yet modulating tumor lymphangiogenic remodeling can influence systemic tissue exposure in a size-dependent manner.

Previous studies of dLN responses to cancer have been primarily focused upon remodeling of cellular subsets, particularly lymphatic endothelial cells [20], stromal cells [19], and B cells [18], or reorganization of extracellular matrix structure and composition [18], yet the influence of tumor remodeling and endogenous or induced angiogenic and lymphangiogenic signaling on the partitioning of macromolecular and particulate species within these adapted dLN has been largely unexplored. It is known that molecular passage into the conduit system is usually restricted to molecules below 70 kDa, while larger molecular weight species entering the lymph node are filtered around the subcapsular sinus and even with Vaccinia virus-induced remodeling of the dLN, size-based fluorescent tracer distribution do not change [16]. Additionally, subcapsular and medullary sinus macrophages have been observed to play an important barrier function in the capture and presentation of lymph-borne pathogens that would otherwise overwhelm the dLN [181]. In our current study, we noted a disruption in the F4/80+ CD169+ SSM layer surrounding WT and VEGFR-2 inhibitor treated LNs (Figure 5.5C) and our flow cytometry results demonstrated a significantly lower percentage of 30 nm tracer positive exposure for SSMs and 10 nm tracer exposure for MCMs in WT dLNs (Figure 5.7A, B). While the 30 nm dLN exposure profile is lower for WT animals (Figure 5.3H), our other metrics of flow cytometry and IHC suggest that this may be due to disorganization of SSM barrier cells in the remodeled tumor dLN that results in reduced uptake and accumulation of 30 nm tracer that may coincide with a reduction in tracer lymphatic transport. Also, 30 and 10 nm tracer exposures to LN paracortex-resident cDC, pDC, dDC, and LC are decreased (Figure 5.7C) in accord with reductions in tissue-level accumulation profiles (Figure 5.3H, I) in WT as compared to naïve dLN, yet T and B cell

exposure levels in WT versus naïve dLN are not significantly different (Figure 5.7A). These data indicate that tissue-level changes in transport to and molecular abundance within the dLN do not always translate to an equally proportional change in molecular association and/or uptake by all dLN cell subtypes, specifically for tumor dLN.

While the disseminated effects of tumor-derived molecules in systemic tissues are an emerging area of study, a recent report for an E.G7 mouse tumor model indicated that the immune suppressive effects due to tolerance induction by marginal zone monocytes on CD8<sup>+</sup> T cells were absent in splenectomized mice [11]. Our results indicate that neither VEGF-C OE nor VEGFR-2 inhibition could mitigate the exposure of tracer molecules on spleen-resident cells (Figure 5.6G-J). However, VEGFR-2 inhibition in WT tumors did result in less 10 nm tumor-derived molecular exposure in lung-resident CD11c<sup>+</sup> and F4/80<sup>+</sup> cellular populations as compared to WT exposure (Figure 5.6G-H), which is a common site for melanoma metastases [55, 182]. While the use of angioplastic therapies may be desirable for reducing primary tumor growth, our results indicate changes in tumor-derived molecular exposure profiles and other examples demonstrating enhanced metastasis following angiogenic inhibition [49, 183] indicate the need to further assess adverse TSF signaling effects.

## **5.5 Conclusions**

Through both tissue- and cellular-level analyses, our results inform that VEGF-C OE and VEGFR-2 inhibition reduce systemic tissue accumulation of 500 and 30 nm species while partially restoring molecular transport to dLN. Altered accumulation profiles of 30 and 10 nm TSF within tumor-dLN, specifically with decreased molecular exposure to dendritic, migratory, and barrier cell subsets, were accompanied by dendritic

cell and macrophage disorganization. Our findings have important implications in the role of tumor blood and lymphatic remodeling in modulating tumor immune suppression and metastasis, and for informing the development of therapeutic or preventive strategies against advanced cancer progression.

## CHAPTER 6. CONCLUDING REMARKS AND FUTURE DIRECTIONS

### 6.1 Contributions to the Field

#### 6.1.1 *Multi-tool Integration to Determine In Situ Soluble Factor Clearance, Accumulation, and Biodistribution at Picomolar Levels*

This thesis dissertation work integrated concepts of lymphatic and vascular physiology with unique and state-of-the-art bioengineering tools to analyze the influence of cancer progression and vascular remodeling on SF transport and resulting profiles of tissue and cellular distribution. This strategy is fundamentally different from widely-used *in vitro* studies that merely analyze TSF production by the co-incubation of cells without any influence of clearance into the blood versus lymphatic vascular systems and distribution to disseminated tissues. Major advantages of the molecular tracer methodology include its cell-source unbiased basis, facile implementation for in situ tracing, high performance in terms of limit of detection, and format that allows for integration with other analytical platforms such as single-cell surface marker profiling and co-localized imaging studies. The extremely low limits of detection enable quantification of transport to and concentration within very small murine lymph nodes. For example, detection and quantification of endogenously produced SF are limited by significant dilutional effects as well as uncertainty in the spatial and temporal source of constitutive or inducible reporter systems. Furthermore, biodistribution analysis of specific exogenously labeled and supplied SF can be challenging due to degradation *in vivo*. To circumvent these limitations, a panel of near-infrared fluorescently labeled molecular tracers comprised of inert polymers that are resistant to hydrolysis and proteolytic degradation was established. Near infrared fluorophore selection was

performed to minimize tissue absorbance and light scattering as well as minimize fluorescence overlap to achieve simultaneous limits of detection in the picomolar range for multiple tracers, thus reducing the number of animals needed for analysis. Using an endpoint approach with plate reader detection also overcomes conventional live animal imaging methods where depth of tissue penetration, signal to noise ratio, and light scattering limit the sensitivity of detection.

Since SF and therapeutic agents such as small molecule drugs and engineered drug delivery vehicles vary widely in hydrodynamic diameter and the rate and extent of blood versus lymphatic clearance from healthy tissues are acutely size-dependent [56, 58], tracers over a range of 5-500 nm in hydrodynamic diameter were chosen to size match a range of physiological biomolecules. Thus, the designed methodology enables not only analysis of the effect of molecule size on clearance, but also distinguishes between blood versus lymphatic mediated SF clearance mechanisms. This approach provided broad insight into the pathophysiology of SF in cancer as well as provided design criteria for tumor and TDLN targeted therapeutic approaches and delivery design.

#### *6.1.2 Validating Conservation of Size-dependent Lymph Node Drug Targeting in Melanomas over the Course of Disease Progression*

In line with previous reports [101], the major lymph-draining tracers were found to be 30 nm in hydrodynamic size in both healthy (Figure 3.3D-E,G) and malignant (Figure 3.7E) skin. Interestingly, despite reduced total levels of dLN accumulation, the relative accumulation of 30 nm tracer in dLN relative to systemic tissues remained relatively unchanged. This indicates that despite reductions in lymphatic transport function (Figure 3.7), TSF approximately 30 nm in diameter such as exosomes and large protein

complexes continue to primarily signal extratumorally within TDLN (Figure 3.8C-D) as opposed to systemic tissues. These results also highlight the potential utility of drug formulations ~30 nm in size to accumulate substantially in sentinel lymph nodes when intralesionally administered which is an important discovery for immunotherapeutic drug delivery applications.

### *6.1.3 Demonstrating Enhanced Systemic Tissue Accumulation of Tumor-derived Factors with Advanced Malignancy*

Herein the results show that 500 and 50 nm tracers cleared from the tumor accumulate at elevated levels in the liver and spleen (Figure 3.6D). Moreover, we found these tracers to accumulate appreciably within the lungs of animals with advanced (day 9 post-implant) malignancies (Figure 3.6C), a redirection in their biodistribution that occurred concurrently with attenuated transport to TDLN (Figure 3.7). TSF signaling that would take place within dLN in naïve animals appears to instead be redirected to lungs of tumor-bearing animals.

Small to intermediate size biomolecules secreted by tumors such as peptides, proteins, and other biomolecules have also been implicated in a multitude of roles that exacerbate disease progression [109, 113]. We provide evidence that exposure of small molecules ~5 nm in hydrodynamic size is also appreciably increased in systemic relative to dLN tissues in tumor-bearing animals (Figure 3.6). Overall, accumulation of 500, 50 and 5 nm tracers shifted significantly from dLN to systemic tissues over the time course of disease progression evaluated here (Figure 3.8). As a result, profiles of TSF tracer accumulation in the liver and lung diverged from that seen in naïve animals and instead more closely mirrored those of the primary tumor (Figure 3.8D). This suggests that

signaling processes active within the tumor microenvironment have the potential to be operational in systemic tissues of melanoma-bearing animals and may significantly regulate and negatively influence the course of disease progression. They also indicate that therapeutic agents administered intralesionally, for example oncolytic immunotherapy, may also result in significant signaling activity outside of the primary tumor in distributed systemic tissues.

#### *6.1.4 Informing the Rational Design of Drug Targeting and Delivery Strategies to Achieve Locoregional Immunomodulation in Skin and dLN*

As previous studies[48, 144] have demonstrated that the extent of LN delivery influences immunotherapeutic outcomes,[48, 144] we show herein the importance of considering the coupled effects of both the size and form/flexibility of biomaterial carriers. While Fifi et al. [91] showed that the size of antigen conjugated polystyrene spheres influenced antibody titers, LN cellular uptake, and anti-tumor immune response, the study did not include a size-matched comparison versus any other carrier formulation. Similarly, the study by Manolova et al. [92] demonstrated the effect of particle size on cellular transport and lymphatic uptake, which included many sizes of polystyrene particles and one virus-like particle, but had no direct, size-matched comparison between formulation or flexibility (the virus-like particle was 30 nm in diameter while the adjacent particle sizes were 20 and 100 nm). Additionally, the effect of biomaterial form and flexibility has been studied with respect to improving carrier circulation [93] and uptake of particles by cells [94], but has not been previously explored as a variable influencing dermal retention or dLN accumulation. Therefore, the effect of different forms on size-matched biomaterial carrier performance for dermal retention and dLN delivery is a knowledge gap in the field that this dissertation addresses by using

comparisons between eight tracers (5, 10, 12, 30, and 54 nm dextran and 25, 50, and 500 nm polystyrene spheres) within an order of magnitude of the known optimum hydrodynamic size range for lymphatic delivery with two size matched, direct comparisons between 500 kDa (30 nm) dextran and 25 nm polystyrene spheres as well as 2000 kDa (54 nm) dextran and 50 nm polystyrene spheres. The time points of analysis (24 and 72 hr p.i.) were chosen to allow the interrogation of both lymphatic transport mechanisms: cell-mediated uptake and migration which peaks 2-4 d p.i.[100, 161] versus passive lymphatic drainage from the interstitial injection site [48, 58, 70, 71, 162].

Corroborating earlier reports [163, 179], we find retention within the injected skin to be size-dependent (Figure 4.3A), as is the selectivity of skin exposure to injected agent relative to systemic tissues (Figure 4.3B). When size matched, macromolecular and particulate retention in the skin is equivalent (Figure 4.3A), resulting in similar, although somewhat higher in the case of ~25-30 nm sized tracers, skin exposure (Figure 4.5C). Levels of dLN accumulation were higher for dextrans relative to polystyrene spheres at all tested sizes, save 5 nm dextran (Figure 4.4A). However, the specificity of dLN accumulation relative to systemic tissues was highest for an intermediate-sized (30 nm) dextran and at 72 hr p.i. for the largest (500 nm) polystyrene sphere tested (Figure 4.4C), presumably due to these tracers exhibiting the most robust levels of lymphatic uptake[101] versus high level of retention within (Figure 4.3A) and restriction to (Figure 4.3B) the skin as well as dependency of the 500 nm tracer on cell-mediated transport to dLN (Figure 4.4B). Furthermore, macromolecular tracers accumulated in dLN at levels roughly ten times that of size-matched polystyrene spheres (Figure 4.5B-D). Therefore, the interplay among hydrodynamic size and flexible, chain-like macromolecular versus

rigid, spherical particulate form control the exposure at the site of skin injection versus simultaneous capacity to deliver payload to dLN, respectively.

#### *6.1.5 Providing Insight of Molecular Mechanisms of Tumor Vascular Remodeling Influencing Soluble Factor Transport and Cellular Association*

Tracer biodistribution data in this dissertation work show interesting, yet unexpected trends for dLN versus systemic tissue accumulation profiles under the effects of altered angiogenic and lymphangiogenic signaling. VEGFR-2 inhibition was expected to normalize blood vessels and, therefore, tracer exposure to systemic tissues. While we observed systemic exposure profile AUCs return to near naïve levels for small molecules around 10 nm in hydrodynamic diameter, VEGFR-2 inhibitor treatment also resulted in partially normalized 500 and 10 nm dLN accumulation as compared to WT animals which may be attributed to normalized intratumoral fluid pressure and/or a partial reduction of tumor blood vessel pore sizes creating opportunity for enhanced lymphatic transport. Contrarily, VEGF-C OE was expected to maximally influence 30 nm tracer profiles in dLN as this is the primary lymphatic draining molecule of the tracer panel [179]. However, we saw no significant change between WT and VC groups in 30 nm tracer exposure to dLN, yet VEGF-C OE increased dLN exposure levels significantly for the 500 and 10 nm tracers in VC versus WT dLN indicating the potential for tumor lymphangiogenic remodeling to exert a greater effect on the lymphatic transport of cells and small 10 nm (40 kDa) molecules, rather than larger 30 nm (500 kDa) species. Combined, these findings demonstrate the inherent relationship between tissue angiogenic and lymphangiogenic signaling and the subsequent remodeling that impacts the blood clearance versus lymphatic drainage of interstitial molecules in a size-dependent manner.

## 6.2 Future Directions

### 6.2.1 *Developing Therapeutic Strategies to Curtail the Aberrant Transport Profiles and Negative Disease Outcomes of Cancer Soluble Factors*

By better understanding the transport of tumor-derived molecules throughout the body and the effects of tumor vascular remodeling on such transport, this work informs a new avenue of therapy development against systemic signaling and progression of cancer by exposing the timing and tissue locations in which inhibitor or neutralizing therapies may have the greatest benefit. Increased understanding of endogenous tumor-secreted molecular profiles could also be used as prognostic indicators of cancer progression as we have observed increased accumulation of TSF in systemic tissues in association with increased vascular leakiness.

Future studies could involve combining angioplastic and immunotherapy treatments with the knowledge gained from this dissertation work on how vascular remodeling affects dLN transport. Spontaneous development of adaptive immunity against melanomas is associated with improved clinical outcome [184], indicating the potential for melanoma immunotherapy. However, current immunotherapy results demonstrate limited efficacy due to the impaired surveillance of tumor antigen from rapidly mutating cancer cells and the influence of high concentrations of immune modulatory cytokines in the local immune milieu [185, 186]. Furthermore, normalizing the tumor's vascular plexus may result in a more effective anti-tumor immune response by improving drainage of tumor antigens as well as cell-mediated transport to dLN and reducing the stagnant accumulation of immune modulatory cytokines within the tumor.

Characterizing changes in TSF heterogeneity, size distributions, and physical properties over the course of cancer progression and their potential effects on biodistribution profiles should be the focus of future studies. In ovarian cancer, exosomes from healthy ovarian epithelial cells were significantly larger than from malignant cell lines [187]. Additionally, the size distribution of exosomes changes with microenvironmental factors such as substrate stiffness and composition in an *in vitro* tumor model [188]. Potential changes in membrane thickness and the number of amphiphilic molecules incorporated in vesicle membranes may also influence the size distribution and, of equal importance given our current results, the stiffness of vesicles as indicated by energetic and thermodynamic models [189]. While our results herein provide a baseline understanding of molecular clearance and biodistribution from a primary melanoma, further studies on how the evolving physicochemical properties of TSF influence their transport is necessary to develop strategies to prevent their deleterious effects.

### 6.2.2 *Clinical Applications of Targeted Locoregional Immunotherapies*

As opposed to systemic immunotherapy, the benefits of locoregional therapies targeting the afflicted tissue of interest and the dLN are evident in higher local drug concentrations resulting in dose sparing and reduced off-target effects depending upon the engineered biomaterial platform used. Additionally, controlled release platforms administered in local tissues may provide more consistent drug exposure levels, reduce the need for repeated injections, and be cleared from the body less quickly than any platform introduced directly into circulation which will have to overcome first pass elimination by the reticuloendothelial system. Biomaterial-based locoregional

immunotherapy could be implemented in any disease case in which the diseased tissue and dLN are both desirable targets, such as the targeting of PD-L1 expressed by cancer cells in the tumor as well as antigen presenting cells in the TDLN using monoclonal antibody therapy. Further examples include intralymphatic immunotherapy [95, 96], allergic contact dermatitis, plaque psoriasis [97], and oncolytic virus therapy [98].

### 6.2.3 *Evaluation of Soluble Factor Transport in Other Inflammatory Diseases*

Future studies of chronic inflammatory diseases and wound healing applications that involve vascular remodeling may benefit from similar studies of soluble factor dissemination to reveal aberrant signaling pathways. Alternatively, accumulation of systemically-derived soluble factors could be enhanced by local vascular remodeling resulting in disease progression. Observations indicate patients with active rheumatoid arthritis exhibit circulating microparticles (0.2-1  $\mu\text{m}$  in diameter, derived from platelets) at levels four to six times higher than healthy patients [190]. Interestingly, CD41+ platelet-derived microparticles, but not platelets themselves, were recently shown to present in the synovial fluid of patients with rheumatoid arthritis [191]. Surprisingly, such microparticles were not observed in the synovial fluid of osteoarthritis patients [191]. These microparticles were also shown to bind directly to leukocytes in the synovial fluid and play a role in amplifying the pathophysiology of rheumatoid arthritis, although the process by which these microparticles accumulate in the synovial fluid remains unknown. Investigating the role of SF in disease progression in other diseases which involve chronic inflammatory signaling and vascular remodeling may be worthwhile, including chronic inflammatory periodontal disease, asthma and chronic obstructive pulmonary

disease (COPD), pulmonary hypertension, certain cardiovascular diseases, Crohn's disease, and diabetes induced obesity.

## REFERENCES

1. Yang, L. and H.L. Moses, *Transforming Growth Factor  $\beta$ : Tumor Suppressor or Promoter? Are Host Immune Cells the Answer?* Cancer Research, 2008. **68**(22): p. 9107-9111.
2. Wai, P.Y. and P.C. Kuo, *Osteopontin: regulation in tumor metastasis*. Cancer and Metastasis Reviews, 2008. **27**(1): p. 103-118.
3. Peinado, H., et al., *Pre-metastatic niches: organ-specific homes for metastases*. Nat Rev Cancer, 2017. **advance online publication**.
4. Psaila, B. and D. Lyden, *The metastatic niche: adapting the foreign soil*. Nat Rev Cancer, 2009. **9**(4): p. 285-93.
5. Kaplan, R.N., et al., *VEGFR1-positive haematopoietic bone marrow progenitors initiate the pre-metastatic niche*. Nature, 2005. **438**(7069): p. 820-827.
6. Gupta, G.P., et al., *ID genes mediate tumor reinitiation during breast cancer lung metastasis*. Proc Natl Acad Sci U S A, 2007. **104**(49): p. 19506-11.
7. Hoshino, A., et al., *Tumour exosome integrins determine organotropic metastasis*. Nature, 2015. **527**(7578): p. 329-335.
8. Lu, X. and Y. Kang, *Organotropism of Breast Cancer Metastasis*. Journal of Mammary Gland Biology and Neoplasia, 2007. **12**(2): p. 153.
9. Kowanzet, M., et al., *Granulocyte-colony stimulating factor promotes lung metastasis through mobilization of Ly6G+Ly6C+ granulocytes*. Proceedings of the National Academy of Sciences, 2010. **107**(50): p. 21248-21255.
10. Seubert, B., et al., *Tissue inhibitor of metalloproteinases (TIMP)-1 creates a premetastatic niche in the liver through SDF-1/CXCR4-dependent neutrophil recruitment in mice*. Hepatology, 2015. **61**(1): p. 238-248.
11. Ugel, S., et al., *Immune Tolerance to Tumor Antigens Occurs in a Specialized Environment of the Spleen*. Cell Reports, 2012. **2**(3): p. 628-639.
12. Less, J.R., et al., *Microvascular Architecture in a Mammary Carcinoma: Branching Patterns and Vessel Dimensions*. Cancer Research, 1991. **51**(1): p. 265-273.

13. Yuan, F., et al., *Time-dependent vascular regression and permeability changes in established human tumor xenografts induced by an anti-vascular endothelial growth factor/vascular permeability factor antibody*. Proceedings of the National Academy of Sciences, 1996. **93**(25): p. 14765-14770.
14. Hoshida, T., et al., *Imaging steps of lymphatic metastasis reveals that vascular endothelial growth factor-C increases metastasis by increasing delivery of cancer cells to lymph nodes: therapeutic implications*. Cancer Res, 2006. **66**(16): p. 8065-75.
15. Matsumura, Y. and H. Maeda, *A New Concept for Macromolecular Therapeutics in Cancer Chemotherapy: Mechanism of Tumorotropic Accumulation of Proteins and the Antitumor Agent Smancs*. Cancer Research, 1986. **46**(12 Part 1): p. 6387-6392.
16. Gretz, J.E., et al., *Lymph-borne chemokines and other low molecular weight molecules reach high endothelial venules via specialized conduits while a functional barrier limits access to the lymphocyte microenvironments in lymph node cortex*. J Exp Med, 2000. **192**(10): p. 1425-40.
17. Roozendaal, R., et al., *Conduits mediate transport of low-molecular-weight antigen to lymph node follicles*. Immunity, 2009. **30**(2): p. 264-76.
18. Rohner, N.A., et al., *Lymph node biophysical remodeling is associated with melanoma lymphatic drainage*. FASEB J, 2015. **29**(11): p. 4512-22.
19. Riedel, A., et al., *Tumor-induced stromal reprogramming drives lymph node transformation*. Nat Immunol, 2016. **17**(9): p. 1118-1127.
20. Lund, A.W., et al., *VEGF-C promotes immune tolerance in B16 melanomas and cross-presentation of tumor antigen by lymph node lymphatics*. Cell Rep, 2012. **1**(3): p. 191-9.
21. Hiratsuka, S., et al., *Primary tumours modulate innate immune signalling to create pre-metastatic vascular hyperpermeability foci*. Nature Communications, 2013. **4**: p. 1853.
22. Hanahan, D. and R.A. Weinberg, *Hallmarks of cancer: the next generation*. Cell, 2011. **144**(5): p. 646-74.
23. Hargadon, K.M., *Tumor-altered dendritic cell function: implications for anti-tumor immunity*. Front Immunol, 2013. **4**: p. 192.
24. Vetvicka, V. and J. Vetvickova, *Procathepsin D and cytokines influence the proliferation of lung cancer cells*. Anticancer Res, 2011. **31**(1): p. 47-51.
25. Pepper, M.S., et al., *Potent synergism between vascular endothelial growth factor and basic fibroblast growth factor in the induction of angiogenesis in vitro*.

- Biochemical and Biophysical Research Communications, 1992. **189**(2): p. 824-831.
26. Shields, J.D., et al., *Induction of Lymphoidlike Stroma and Immune Escape by Tumors That Express the Chemokine CCL21*. Science, 2010. **328**(5979): p. 749-752.
  27. Crane, C.A., et al., *Soluble factors secreted by glioblastoma cell lines facilitate recruitment, survival, and expansion of regulatory T cells: implications for immunotherapy*. Neuro Oncol, 2012. **14**(5): p. 584-95.
  28. Mu, W., S. Rana, and M. Zöller, *Host Matrix Modulation by Tumor Exosomes Promotes Motility and Invasiveness*. Neoplasia, 2013. **15**(8): p. 875-IN4.
  29. Emri, E., et al., *Correlation among metallothionein expression, intratumoural macrophage infiltration and the risk of metastasis in human cutaneous malignant melanoma*. J Eur Acad Dermatol Venereol, 2013. **27**(3): p. e320-7.
  30. Holmgaard, Rikke B., et al., *Tumor-Expressed IDO Recruits and Activates MDSCs in a Treg-Dependent Manner*. Cell Reports, 2015. **13**(2): p. 412-424.
  31. Wu, A.A., et al., *Reprogramming the tumor microenvironment: tumor-induced immunosuppressive factors paralyze T cells*. Oncoimmunology, 2015. **4**(7): p. e1016700.
  32. Geiger, T., J. Cox, and M. Mann, *Proteomic Changes Resulting from Gene Copy Number Variations in Cancer Cells*. PLOS Genetics, 2010. **6**(9): p. e1001090.
  33. Bendall, S.C. and G.P. Nolan, *From single cells to deep phenotypes in cancer*. Nat Biotech, 2012. **30**(7): p. 639-647.
  34. Vaisanen, A., et al., *Prognostic value of MMP-2 immunoreactive protein (72 kD type IV collagenase) in primary skin melanoma*. J Pathol, 1998. **186**(1): p. 51-8.
  35. Hargadon, K.M., et al., *Melanoma-derived factors alter the maturation and activation of differentiated tissue-resident dendritic cells*. Immunol Cell Biol, 2016. **94**(1): p. 24-38.
  36. Yu, S., et al., *Tumor-derived exosomes in cancer progression and treatment failure*. Oncotarget, 2015. **6**(35): p. 37151-68.
  37. Hood, J.L., R.S. San, and S.A. Wickline, *Exosomes released by melanoma cells prepare sentinel lymph nodes for tumor metastasis*. Cancer Res, 2011. **71**(11): p. 3792-801.
  38. Yang, C., et al., *Tumor-derived exosomes confer antigen-specific immunosuppression in a murine delayed-type hypersensitivity model*. PLoS One, 2011. **6**(8): p. e22517.

39. Callejo, S.A., et al., *Macrophage-derived soluble factor enhances melanoma inhibitory activity expression by uveal melanoma cells in vitro*. *Melanoma Res*, 2004. **14**(2): p. 91-5.
40. Ruffini, F., et al., *Expression of the soluble vascular endothelial growth factor receptor-1 in cutaneous melanoma: role in tumour progression*. *Br J Dermatol*, 2011. **164**(5): p. 1061-70.
41. Roxana Stefania Dronca, S.H., Mithulan Jegapragasan, Lisa A. Kottschade, Wendy Kay Nevala, Elizabeth Ann Enninga, Svetomir Markovic, Haidong Dong, *Association of soluble PD-L1 (sPD-L1) with decreased survival in metastatic melanoma*. *J Clin Oncol*, 2017. **35**.
42. Weinstein, D., et al., *Diagnostic and Prognostic Biomarkers in Melanoma*. *J Clin Aesthet Dermatol*, 2014. **7**(6): p. 13-24.
43. Kell, J.S., *Prostate-specific antigen tests and prostate cancer screening: an update for primary care physicians*. *Can J Urol*, 2010. **17 Suppl 1**: p. 18-25.
44. Kazarian, A., et al., *Testing breast cancer serum biomarkers for early detection and prognosis in pre-diagnosis samples*. *Br J Cancer*, 2017. **116**(4): p. 501-8.
45. Eichelser, C., et al., *Increased serum levels of circulating exosomal microRNA-373 in receptor-negative breast cancer patients*. *Oncotarget*, 2014. **5**(20): p. 9650-63.
46. Peinado, H., et al., *Melanoma exosomes educate bone marrow progenitor cells toward a pro-metastatic phenotype through MET*. *Nat Med*, 2012. **18**(6): p. 883-91.
47. Lee, E., et al., *Breast cancer cells condition lymphatic endothelial cells within pre-metastatic niches to promote metastasis*. *Nat Commun*, 2014. **5**: p. 4715.
48. Thomas, S.N., et al., *Targeting the tumor-draining lymph node with adjuvanted nanoparticles reshapes the anti-tumor immune response*. *Biomaterials*, 2014. **35**(2): p. 814-24.
49. Skobe, M., et al., *Induction of tumor lymphangiogenesis by VEGF-C promotes breast cancer metastasis*. *Nat Med*, 2001. **7**(2): p. 192-8.
50. Karpanen, T., et al., *Vascular endothelial growth factor C promotes tumor lymphangiogenesis and intralymphatic tumor growth*. *Cancer Res*, 2001. **61**(5): p. 1786-90.
51. Harrell, M.I., B.M. Iritani, and A. Ruddell, *Tumor-Induced Sentinel Lymph Node Lymphangiogenesis and Increased Lymph Flow Precede Melanoma Metastasis*. *The American Journal of Pathology*, 2007. **170**(2): p. 774-786.

52. Mansfield, A.S., et al., *Regional immunity in melanoma: immunosuppressive changes precede nodal metastasis*. *Mod Pathol*, 2011. **24**(4): p. 487-94.
53. Davila, M., et al., *Tissue factor-bearing microparticles derived from tumor cells: impact on coagulation activation*. *J Thromb Haemost*, 2008. **6**(9): p. 1517-24.
54. Mehlen, P. and A. Puisieux, *Metastasis: a question of life or death*. *Nat Rev Cancer*, 2006. **6**(6): p. 449-58.
55. Meier, F., et al., *Metastatic pathways and time courses in the orderly progression of cutaneous melanoma*. *Br J Dermatol*, 2002. **147**(1): p. 62-70.
56. Sarin, H., *Physiologic upper limits of pore size of different blood capillary types and another perspective on the dual pore theory of microvascular permeability*. *J Angiogenes Res*, 2010. **2**: p. 14.
57. Welter, M. and H. Rieger, *Interstitial fluid flow and drug delivery in vascularized tumors: a computational model*. *PLoS One*, 2013. **8**(8): p. e70395.
58. Thomas, S.N. and A. Schudel, *Overcoming transport barriers for interstitial-, lymphatic-, and lymph node-targeted drug delivery*. *Current Opinion in Chemical Engineering*, 2015. **7**(0): p. 65-74.
59. Allan, R.S., et al., *Migratory Dendritic Cells Transfer Antigen to a Lymph Node-Resident Dendritic Cell Population for Efficient CTL Priming*. *Immunity*, 2006. **25**(1): p. 153-162.
60. Jain, R.K. and T. Stylianopoulos, *Delivering nanomedicine to solid tumors*. *Nat Rev Clin Oncol*, 2010. **7**(11): p. 653-64.
61. Andersen, B. and H.H. Ussing, *Solvent drag on non-electrolytes during osmotic flow through isolated toad skin and its response to antidiuretic hormone*. *Acta Physiol Scand*, 1957. **39**(2-3): p. 228-39.
62. Rohner, N.A. and S.N. Thomas, *Melanoma growth effects on molecular clearance from tumors and biodistribution into systemic tissues versus draining lymph nodes*. *Journal of Controlled Release*, 2016. **223**: p. 99-108.
63. Young, J.S., C.E. Llumsden, and A.L. Stalker, *The significance of the "tissue pressure" of normal testicular and of neoplastic (Brown-Pearce carcinoma) tissue in the rabbit*. *The Journal of Pathology and Bacteriology*, 1950. **62**(3): p. 313-333.
64. Boucher, Y., L.T. Baxter, and R.K. Jain, *Interstitial pressure gradients in tissue-isolated and subcutaneous tumors: implications for therapy*. *Cancer Res*, 1990. **50**(15): p. 4478-84.

65. Heldin, C.-H., et al., *High interstitial fluid pressure [mdash] an obstacle in cancer therapy*. Nat Rev Cancer, 2004. **4**(10): p. 806-813.
66. Jain, R.K., *Normalization of tumor vasculature: an emerging concept in antiangiogenic therapy*. Science, 2005. **307**(5706): p. 58-62.
67. Jain, R.K., *Normalizing tumor microenvironment to treat cancer: bench to bedside to biomarkers*. J Clin Oncol, 2013. **31**(17): p. 2205-18.
68. Netti, P.A., et al., *Role of extracellular matrix assembly in interstitial transport in solid tumors*. Cancer Res, 2000. **60**(9): p. 2497-503.
69. Ramanujan, S., et al., *Diffusion and convection in collagen gels: implications for transport in the tumor interstitium*. Biophys J, 2002. **83**(3): p. 1650-60.
70. Thomas, S.N., N.A. Rohner, and E.E. Edwards, *Implications of Lymphatic Transport to Lymph Nodes in Immunity and Immunotherapy*. Annu Rev Biomed Eng, 2016.
71. Thomas, S.N., et al., *Impaired humoral immunity and tolerance in K14-VEGFR-3-Ig mice that lack dermal lymphatic drainage*. J Immunol, 2012. **189**(5): p. 2181-90.
72. Mebius, R.E., et al., *The influence of afferent lymphatic vessel interruption on vascular addressin expression*. J Cell Biol, 1991. **115**(1): p. 85-95.
73. Bajenoff, M. and R.N. Germain, *B-cell follicle development remodels the conduit system and allows soluble antigen delivery to follicular dendritic cells*. Blood, 2009. **114**(24): p. 4989-97.
74. Tomei, A.A., et al., *Fluid Flow Regulates Stromal Cell Organization and CCL21 Expression in a Tissue-Engineered Lymph Node Microenvironment*. The Journal of Immunology, 2009. **183**(7): p. 4273-4283.
75. Halin, C., et al., *VEGF-A produced by chronically inflamed tissue induces lymphangiogenesis in draining lymph nodes*. Blood, 2007. **110**(9): p. 3158-3167.
76. Kunder, C.A., et al., *Mast cell-derived particles deliver peripheral signals to remote lymph nodes*. The Journal of Experimental Medicine, 2009. **206**(11): p. 2455-2467.
77. Acton, S.E., et al., *Dendritic cells control fibroblastic reticular network tension and lymph node expansion*. Nature, 2014. **514**(7523): p. 498-502.
78. Martin-Fontecha, A., et al., *Regulation of dendritic cell migration to the draining lymph node: impact on T lymphocyte traffic and priming*. J Exp Med, 2003. **198**(4): p. 615-21.

79. Webster, B., et al., *Regulation of lymph node vascular growth by dendritic cells*. The Journal of Experimental Medicine, 2006. **203**(8): p. 1903-1913.
80. Jeanbart, L., et al., *Enhancing Efficacy of Anticancer Vaccines by Targeted Delivery to Tumor-Draining Lymph Nodes*. Cancer Immunology Research, 2014. **2**(5): p. 436-447.
81. Rizwan, A., et al., *Metastatic breast cancer cells in lymph nodes increase nodal collagen density*. Sci Rep, 2015. **5**: p. 10002.
82. Ondondo, B., et al., *Progression of carcinogen-induced fibrosarcomas is associated with the accumulation of naïve CD4+ T cells via blood vessels and lymphatics*. International Journal of Cancer. Journal International du Cancer, 2014. **134**(9): p. 2156-2167.
83. Paszek, M.J., et al., *Tensional homeostasis and the malignant phenotype*. Cancer Cell, 2005. **8**(3): p. 241-54.
84. Shields, J.D., et al., *Autologous chemotaxis as a mechanism of tumor cell homing to lymphatics via interstitial flow and autocrine CCR7 signaling*. Cancer Cell, 2007. **11**(6): p. 526-38.
85. Shieh, A.C., et al., *Tumor cell invasion is promoted by interstitial flow-induced matrix priming by stromal fibroblasts*. Cancer Res, 2011. **71**(3): p. 790-800.
86. Barcus, C.E., et al., *Stiff Collagen Matrices Increase Tumorigenic Prolactin Signaling in Breast Cancer Cells*. The Journal of Biological Chemistry, 2013. **288**(18): p. 12722-12732.
87. Insana, M.F., et al., *Viscoelastic imaging of breast tumor microenvironment with ultrasound*. J Mammary Gland Biol Neoplasia, 2004. **9**(4): p. 393-404.
88. Gutmann, R., et al., *Interstitial hypertension in head and neck tumors in patients: correlation with tumor size*. Cancer Res, 1992. **52**(7): p. 1993-5.
89. Nathanson, S.D. and M. Mahan, *Sentinel lymph node pressure in breast cancer*. Ann Surg Oncol, 2011. **18**(13): p. 3791-6.
90. Nathanson, S.D., R. Shah, and K. Rosso, *Sentinel lymph node metastases in cancer: Causes, detection and their role in disease progression*. Seminars in Cell & Developmental Biology, 2015. **38**(0): p. 106-116.
91. Fifis, T., et al., *Size-dependent immunogenicity: therapeutic and protective properties of nano-vaccines against tumors*. J Immunol, 2004. **173**(5): p. 3148-54.
92. Manolova, V., et al., *Nanoparticles target distinct dendritic cell populations according to their size*. Eur J Immunol, 2008. **38**(5): p. 1404-13.

93. Mitragotri, S. and J. Lahann, *Physical approaches to biomaterial design*. Nat Mater, 2009. **8**(1): p. 15-23.
94. Sun, J., et al., *Tunable Rigidity of (Polymeric Core)–(Lipid Shell) Nanoparticles for Regulated Cellular Uptake*. Advanced Materials, 2015. **27**(8): p. 1402-1407.
95. Johansen, P., et al., *Direct intralymphatic injection of peptide vaccines enhances immunogenicity*. European Journal of Immunology, 2005. **35**(2): p. 568-574.
96. Senti, G., et al., *Intralymphatic allergen administration renders specific immunotherapy faster and safer: a randomized controlled trial*. Proc Natl Acad Sci U S A, 2008. **105**(46): p. 17908-12.
97. Shah, P., et al., *Skin permeating nanogel for the cutaneous co-delivery of two anti-inflammatory drugs*. Biomaterials, 2012. **33**(5): p. 1607-1617.
98. Lawler, S.E., et al., *Oncolytic viruses in cancer treatment: A review*. JAMA Oncology, 2016.
99. Duvall, C.L., et al., *Quantitative microcomputed tomography analysis of collateral vessel development after ischemic injury*. Am J Physiol Heart Circ Physiol, 2004. **287**(1): p. H302-10.
100. Kissenpfennig, A., et al., *Dynamics and Function of Langerhans Cells In Vivo: Dermal Dendritic Cells Colonize Lymph Node Areas Distinct from Slower Migrating Langerhans Cells*. Immunity, 2005. **22**(5): p. 643-654.
101. Reddy, S.T., et al., *A sensitive in vivo model for quantifying interstitial convective transport of injected macromolecules and nanoparticles*. J Appl Physiol (1985), 2006. **101**(4): p. 1162-9.
102. Kontani, K., et al., *Factors responsible for long-term survival in metastatic breast cancer*. World J Surg Oncol, 2014. **12**: p. 344.
103. Wolchok, J.D., et al., *Development of ipilimumab: a novel immunotherapeutic approach for the treatment of advanced melanoma*. Ann N Y Acad Sci, 2013. **1291**: p. 1-13.
104. Timp, J.F., et al., *Epidemiology of cancer-associated venous thrombosis*. Blood, 2013. **122**(10): p. 1712-1723.
105. Walker, A.J., et al., *Incidence of venous thromboembolism in patients with cancer – A cohort study using linked United Kingdom databases*. European Journal of Cancer, 2013. **49**(6): p. 1404-1413.
106. Rickles, F.R., *Mechanisms of cancer-induced thrombosis in cancer*. Pathophysiol Haemost Thromb, 2006. **35**(1-2): p. 103-10.

107. Erler, J.T., et al., *Hypoxia-induced lysyl oxidase is a critical mediator of bone marrow cell recruitment to form the premetastatic niche*. *Cancer Cell*, 2009. **15**(1): p. 35-44.
108. Jafarzadeh, A., et al., *Higher circulating levels of chemokine CCL22 in patients with breast cancer: evaluation of the influences of tumor stage and chemokine gene polymorphism*. *Tumour Biol*, 2015. **36**(2): p. 1163-71.
109. Pitteri, S.J., et al., *Tumor Microenvironment-Derived Proteins Dominate the Plasma Proteome Response during Breast Cancer Induction and Progression*. *Cancer Research*, 2011. **71**(15): p. 5090-5100.
110. Pfitzenmaier, J., et al., *Elevation of cytokine levels in cachectic patients with prostate carcinoma*. *Cancer*, 2003. **97**(5): p. 1211-1216.
111. Baran, J., et al., *Circulating tumour-derived microvesicles in plasma of gastric cancer patients*. *Cancer Immunol Immunother*, 2010. **59**(6): p. 841-50.
112. Bergmann, C., et al., *Tumor-derived microvesicles in sera of patients with head and neck cancer and their role in tumor progression*. *Head Neck*, 2009. **31**(3): p. 371-80.
113. Tichet, M., et al., *Tumour-derived SPARC drives vascular permeability and extravasation through endothelial VCAM1 signalling to promote metastasis*. *Nat Commun*, 2015. **6**.
114. Hiratsuka, S., et al., *Tumour-mediated upregulation of chemoattractants and recruitment of myeloid cells predetermines lung metastasis*. *Nat Cell Biol*, 2006. **8**(12): p. 1369-75.
115. Seymour, L.W., et al., *Tumour tropism and anti-cancer efficacy of polymer-based doxorubicin prodrugs in the treatment of subcutaneous murine B16F10 melanoma*. *Br J Cancer*, 1994. **70**(4): p. 636-41.
116. Yuan, F., et al., *Vascular permeability in a human tumor xenograft: molecular size dependence and cutoff size*. *Cancer Res*, 1995. **55**(17): p. 3752-6.
117. Maeda, H., et al., *Vascular permeability enhancement in solid tumor: various factors, mechanisms involved and its implications*. *International Immunopharmacology*, 2003. **3**(3): p. 319-328.
118. Lee, T.H., et al., *Microvesicles as mediators of intercellular communication in cancer--the emerging science of cellular 'debris'*. *Semin Immunopathol*, 2011. **33**(5): p. 455-67.
119. Kim, C.W., et al., *Extracellular membrane vesicles from tumor cells promote angiogenesis via sphingomyelin*. *Cancer Res*, 2002. **62**(21): p. 6312-7.

120. Andtbacka, R.H., et al., *Talimogene Laherparepvec Improves Durable Response Rate in Patients With Advanced Melanoma*. J Clin Oncol, 2015. **33**(25): p. 2780-8.
121. Liao, S., et al., *Impaired lymphatic contraction associated with immunosuppression*. Proceedings of the National Academy of Sciences of the United States of America, 2011. **108**(46): p. 18784-18789.
122. Munn, L.L., *Mechanobiology of lymphatic contractions*. Semin Cell Dev Biol, 2015. **38**: p. 67-74.
123. Fleury, M.E., K.C. Boardman, and M.A. Swartz, *Autologous Morphogen Gradients by Subtle Interstitial Flow and Matrix Interactions*. Biophysical Journal, 2006. **91**(1): p. 113-121.
124. Miteva, D.O., et al., *Transmural Flow Modulates Cell and Fluid Transport Functions of Lymphatic Endothelium*. Circulation Research, 2010. **106**(5): p. 920-931.
125. Haessler, U., et al., *Dendritic cell chemotaxis in 3D under defined chemokine gradients reveals differential response to ligands CCL21 and CCL19*. Proceedings of the National Academy of Sciences, 2011. **108**(14): p. 5614-5619.
126. Hubbell, J.A., S.N. Thomas, and M.A. Swartz, *Materials engineering for immunomodulation*. Nature, 2009. **462**(7272): p. 449-460.
127. Weber, J.S. and J.J. Mule, *Cancer immunotherapy meets biomaterials*. Nat Biotech, 2015. **33**(1): p. 44-45.
128. Hotaling, N.A., et al., *Biomaterial Strategies for Immunomodulation*. Annual Review of Biomedical Engineering, 2015. **17**(1): p. 317-349.
129. Park, J., et al., *Combination delivery of TGF- $\beta$  inhibitor and IL-2 by nanoscale liposomal polymeric gels enhances tumour immunotherapy*. Nat Mater, 2012. **11**(10): p. 895-905.
130. Xu, Z., et al., *Multifunctional nanoparticles co-delivering Trp2 peptide and CpG adjuvant induce potent cytotoxic T-lymphocyte response against melanoma and its lung metastasis*. Journal of Controlled Release, 2013. **172**(1): p. 259-265.
131. Egilmez, N.K., et al., *Cytokine immunotherapy of cancer with controlled release biodegradable microspheres in a human tumor xenograft/SCID mouse model*. Cancer Immunol Immunother, 1998. **46**(1): p. 21-4.
132. Sabel, M.S., et al., *Intratumoral IL-12 and TNF-alpha-loaded microspheres lead to regression of breast cancer and systemic antitumor immunity*. Ann Surg Oncol, 2004. **11**(2): p. 147-56.

133. Shimizu, T., et al., *Nanogel DDS enables sustained release of IL-12 for tumor immunotherapy*. Biochemical and Biophysical Research Communications, 2008. **367**(2): p. 330-335.
134. Melder, R.J., et al., *Pharmacokinetics and in vitro and in vivo anti-tumor response of an interleukin-2-human serum albumin fusion protein in mice*. Cancer Immunol Immunother, 2005. **54**(6): p. 535-47.
135. Gillies, S.D., et al., *A low-toxicity IL-2-based immunocytokine retains antitumor activity despite its high degree of IL-2 receptor selectivity*. Clin Cancer Res, 2011. **17**(11): p. 3673-85.
136. Zaric, M., et al., *Skin Dendritic Cell Targeting via Microneedle Arrays Laden with Antigen-Encapsulated Poly-d,l-lactide-co-Glycolide Nanoparticles Induces Efficient Antitumor and Antiviral Immune Responses*. ACS Nano, 2013. **7**(3): p. 2042-2055.
137. Hatzifoti, C., et al., *Liposomal Co-Entrapment of CD40mAb Induces Enhanced IgG Responses against Bacterial Polysaccharide and Protein*. PLoS ONE, 2008. **3**(6): p. e2368.
138. Wang, C., et al., *Enhanced Cancer Immunotherapy by Microneedle Patch-Assisted Delivery of Anti-PD1 Antibody*. Nano Letters, 2016. **16**(4): p. 2334-2340.
139. Zaharoff, D.A., et al., *Intratumoral immunotherapy of established solid tumors with chitosan/IL-12*. J Immunother, 2010. **33**(7): p. 697-705.
140. Ruiz, P., et al., *Transplant Tolerance: New Insights and Strategies for Long-Term Allograft Acceptance*. Clinical and Developmental Immunology, 2013. **2013**: p. 15.
141. Fransen, M.F., R. Arens, and C.J.M. Melief, *Local targets for immune therapy to cancer: Tumor draining lymph nodes and tumor microenvironment*. International Journal of Cancer, 2013. **132**(9): p. 1971-1976.
142. Chandrasekaran, S. and M.R. King, *Microenvironment of Tumor-Draining Lymph Nodes: Opportunities for Liposome-Based Targeted Therapy*. International Journal of Molecular Sciences, 2014. **15**(11): p. 20209-20239.
143. Muraoka, D., et al., *Nanogel-based immunologically stealth vaccine targets macrophages in the medulla of lymph node and induces potent antitumor immunity*. ACS Nano, 2014. **8**(9): p. 9209-18.
144. Liu, H., et al., *Structure-based Programming of Lymph Node Targeting in Molecular Vaccines*. Nature, 2014. **507**(7493): p. 519-522.

145. Dane, K.Y., et al., *Nano-sized drug-loaded micelles deliver payload to lymph node immune cells and prolong allograft survival*. Journal of Controlled Release, 2011. **156**(2): p. 154-160.
146. Bourquin, C., et al., *Targeting CpG Oligonucleotides to the Lymph Node by Nanoparticles Elicits Efficient Antitumoral Immunity*. The Journal of Immunology, 2008. **181**(5): p. 2990-2998.
147. Kwong, B., H. Liu, and D.J. Irvine, *Induction of potent anti-tumor responses while eliminating systemic side effects via liposome-anchored combinatorial immunotherapy*. Biomaterials, 2011. **32**(22): p. 5134-5147.
148. Peiris, P.M., et al., *Treatment of Invasive Brain Tumors Using a Chain-like Nanoparticle*. Cancer Research, 2015. **75**(7): p. 1356-1365.
149. Foged, C., et al., *Particle size and surface charge affect particle uptake by human dendritic cells in an in vitro model*. Int J Pharm, 2005. **298**(2): p. 315-22.
150. Fromen, C.A., et al., *Controlled analysis of nanoparticle charge on mucosal and systemic antibody responses following pulmonary immunization*. Proceedings of the National Academy of Sciences, 2015. **112**(2): p. 488-493.
151. Rao, D.A., et al., *Biodegradable PLGA based nanoparticles for sustained regional lymphatic drug delivery*. J Pharm Sci, 2010. **99**(4): p. 2018-31.
152. Moyano, D.F., et al., *Nanoparticle Hydrophobicity Dictates Immune Response*. Journal of the American Chemical Society, 2012. **134**(9): p. 3965-3967.
153. Champion, J.A., Y.K. Katare, and S. Mitragotri, *Particle shape: a new design parameter for micro- and nanoscale drug delivery carriers*. J Control Release, 2007. **121**(1-2): p. 3-9.
154. Sun, B., et al., *Engineering an Effective Immune Adjuvant by Designed Control of Shape and Crystallinity of Aluminum Oxyhydroxide Nanoparticles*. ACS Nano, 2013. **7**(12): p. 10834-10849.
155. Fan, Y. and J.J. Moon, *Nanoparticle Drug Delivery Systems Designed to Improve Cancer Vaccines and Immunotherapy*. Vaccines (Basel), 2015. **3**(3): p. 662-85.
156. Mehvar, R., M.A. Robinson, and J.M. Reynolds, *Dose dependency of the kinetics of dextrans in rats: effects of molecular weight*. J Pharm Sci, 1995. **84**(7): p. 815-8.
157. Zhuang, Y., et al., *PEGylated cationic liposomes robustly augment vaccine-induced immune responses: Role of lymphatic trafficking and biodistribution*. J Control Release, 2012. **159**(1): p. 135-42.

158. Cornell, R.C., et al., *Intralesional interferon therapy for basal cell carcinoma*. J Am Acad Dermatol, 1990. **23**(4 Pt 1): p. 694-700.
159. Edwards, L., et al., *The effect of intralesional interferon gamma on basal cell carcinomas*. J Am Acad Dermatol, 1990. **22**(3): p. 496-500.
160. Zamarin, D., et al., *Localized Oncolytic Virotherapy Overcomes Systemic Tumor Resistance to Immune Checkpoint Blockade Immunotherapy*. Science Translational Medicine, 2014. **6**(226): p. 226ra32-226ra32.
161. Kamath, A.T., et al., *Developmental kinetics and lifespan of dendritic cells in mouse lymphoid organs*. Blood, 2002. **100**(5): p. 1734-41.
162. Randolph, G.J., V. Angeli, and M.A. Swartz, *Dendritic-cell trafficking to lymph nodes through lymphatic vessels*. Nat Rev Immunol, 2005. **5**(8): p. 617-28.
163. Wu, F., et al., *Fluorescence imaging of the lymph node uptake of proteins in mice after subcutaneous injection: molecular weight dependence*. Pharm Res, 2012. **29**(7): p. 1843-53.
164. Uto, T., et al., *Uptake of biodegradable poly( $\gamma$ -glutamic acid) nanoparticles and antigen presentation by dendritic cells in vivo*. Results in Immunology, 2013. **3**: p. 1-9.
165. Platt, A.M., et al., *Normal dendritic cell mobilization to lymph nodes under conditions of severe lymphatic hypoplasia*. J Immunol, 2013. **190**(9): p. 4608-20.
166. Guo, D., et al., *Elastic Properties of Polystyrene Nanospheres Evaluated with Atomic Force Microscopy: Size Effect and Error Analysis*. Langmuir, 2014. **30**(24): p. 7206-7212.
167. Bippes, C.A., et al., *Direct measurement of single-molecule visco-elasticity in atomic force microscope force-extension experiments*. European Biophysics Journal, 2006. **35**(3): p. 287-292.
168. Radiom, M., et al., *A correlation force spectrometer for single molecule measurements under tensile load*. Journal of Applied Physics, 2013. **113**(1): p. 013503.
169. Babu, S., et al., *Effect of size at the nanoscale and bilayer rigidity on skin diffusion of liposomes*. J Biomed Mater Res A, 2009. **91**(1): p. 140-8.
170. Longmire, M.R., et al., *Biologically Optimized Nanosized Molecules and Particles: More than Just Size*. Bioconjugate Chemistry, 2011. **22**(6): p. 993-1000.

171. Arnida, et al., *Geometry and surface characteristics of gold nanoparticles influence their biodistribution and uptake by macrophages*. Eur J Pharm Biopharm, 2011. **77**(3): p. 417-23.
172. Muro, S., et al., *Control of endothelial targeting and intracellular delivery of therapeutic enzymes by modulating the size and shape of ICAM-1-targeted carriers*. Mol Ther, 2008. **16**(8): p. 1450-8.
173. Topalian, S.L., et al., *Safety, activity, and immune correlates of anti-PD-1 antibody in cancer*. N Engl J Med, 2012. **366**(26): p. 2443-54.
174. Robert, C., et al., *Anti-programmed-death-receptor-1 treatment with pembrolizumab in ipilimumab-refractory advanced melanoma: a randomised dose-comparison cohort of a phase I trial*. Lancet, 2014. **384**(9948): p. 1109-17.
175. Motz, G.T. and G. Coukos, *Deciphering and reversing tumor immune suppression*. Immunity, 2013. **39**(1): p. 61-73.
176. Eroglu, Z. and A. Ribas, *Combination therapy with BRAF and MEK inhibitors for melanoma: latest evidence and place in therapy*. Therapeutic Advances in Medical Oncology, 2016. **8**(1): p. 48-56.
177. Saunderson, S.C., et al., *CD169 mediates the capture of exosomes in spleen and lymph node*. Blood, 2014. **123**(2): p. 208-16.
178. Karagiannis, P., et al., *Elevated IgG4 in patient circulation is associated with the risk of disease progression in melanoma*. Oncoimmunology, 2015. **4**(11): p. e1032492.
179. Rohner, N.A. and S.N. Thomas, *Flexible Macromolecule versus Rigid Particle Retention in the Injected Skin and Accumulation in Draining Lymph Nodes Are Differentially Influenced by Hydrodynamic Size*. ACS Biomaterials Science & Engineering, 2017. **3**(2): p. 153-159.
180. Ganti, S.N., et al., *Regulatory B cells preferentially accumulate in tumor-draining lymph nodes and promote tumor growth*. Scientific Reports, 2015. **5**: p. 12255.
181. Junt, T., et al., *Subcapsular sinus macrophages in lymph nodes clear lymph-borne viruses and present them to antiviral B cells*. Nature, 2007. **450**(7166): p. 110-114.
182. Hiratsuka, S., et al., *MMP9 induction by vascular endothelial growth factor receptor-1 is involved in lung-specific metastasis*. Cancer Cell, 2002. **2**(4): p. 289-300.
183. Hirakawa, S., et al., *VEGF-A induces tumor and sentinel lymph node lymphangiogenesis and promotes lymphatic metastasis*. The Journal of Experimental Medicine, 2005. **201**(7): p. 1089-1099.

184. Girotti, M.R., et al., *No longer an untreatable disease: how targeted and immunotherapies have changed the management of melanoma patients*. *Mol Oncol*, 2014. **8**(6): p. 1140-58.
185. Dahlberg, C.I.M., et al., *Natural Killer Cell-Based Therapies Targeting Cancer: Possible Strategies to Gain and Sustain Anti-Tumor Activity*. *Frontiers in Immunology*, 2015. **6**: p. 605.
186. Kimura, H., et al., *Randomized controlled phase III trial of adjuvant chemo-immunotherapy with activated killer T cells and dendritic cells in patients with resected primary lung cancer*. *Cancer Immunology, Immunotherapy*, 2015. **64**: p. 51-59.
187. Zhang, W., et al., *Characterization of exosomes derived from ovarian cancer cells and normal ovarian epithelial cells by nanoparticle tracking analysis*. *Tumour Biol*, 2016. **37**(3): p. 4213-21.
188. Villasante, A., et al., *Recapitulating the Size and Cargo of Tumor Exosomes in a Tissue-Engineered Model*. *Theranostics*, 2016. **6**(8): p. 1119-1130.
189. Huang, C., et al., *Formation and size distribution of self-assembled vesicles*. *Proceedings of the National Academy of Sciences*, 2017. **114**(11): p. 2910-2915.
190. Knijff-Dutmer, E.A.J., et al., *Elevated levels of platelet microparticles are associated with disease activity in rheumatoid arthritis*. *Arthritis & Rheumatism*, 2002. **46**(6): p. 1498-1503.
191. Boilard, E., et al., *Platelets amplify inflammation in arthritis via collagen-dependent microparticle production*. *Science*, 2010. **327**(5965): p. 580-3.